Electronic Thesis and Dissertation Repository

6-26-2019 11:00 AM

Evaluating zircon strain chronometry of a Grenville Front deformation fabric through microstructural analysis and quartz piezometry

Kaitlyn Petkau
The University of Western Ontario

Supervisor
Jiang, Dazhi
The University of Western Ontario Joint Supervisor
Moser, Desmond
The University of Western Ontario

Graduate Program in Geology
A thesis submitted in partial fulfillment of the requirements for the degree in Master of Science
© Kaitlyn Petkau 2019

Follow this and additional works at: https://ir.lib.uwo.ca/etd

Part of the Geology Commons

Recommended Citation

Abstract

Zircon strain chronometry can theoretically show correlation of isotopic ages with microstructural fabrics to place an absolute age on the timing of deformation. However, the general applicability of zircon strain chronometry to problems in regional continental tectonics is still being tested and this study is the first effort to apply the approach to the ~1 Ga (billion year old) Grenville Province of the Precambrian Canadian Shield. Samples were analyzed from the 1747 +6/-5 Ma Wanapitei Complex, a poly-deformed mafic metaplutonic body that preserves fabric evidence for several stages in the tectonic history of the Grenville Front. This study is the first to combine in situ strain measurements of zircon with independent measurements of past differential stress using quartz grain size piezometry. Zircon grains in Wanapitei Complex samples exhibiting the latest, D_3, ductile deformation were analyzed using electron backscatter diffraction whereas grain size piezometry was completed on a cross-cutting dyke and a marginal gneiss. It was determined that the stress conditions in the Grenville Front near the Wanapitei Complex were not sufficient to deform the generally small (< 50 microns) zircon grains seen in thin sections and result in discordance that would date deformation. Future work targeting significantly larger zircon grains as well as other accessory phases such as baddeleyite and monazite would more thoroughly test the viability of U-Pb strain chronometry in the Grenville Front region.

Keywords

Quartz piezometry, U-Pb dating, polyphase deformation, zircon, Grenville Orogeny, zircon strain chronometry

Summary for Lay Audience

The Grenville Front is an area of complex deformation near Sudbury, Ontario resultant from events that occurred around 1 billion years ago. This thesis explores whether it is possible to date this deformation with increased confidence than previous work. The method examined in this thesis is zircon strain chronometry. Zircon strain chronometry is an underexamined method whereby plastically deformed zircons can be used to provide ages to the events in which the zircons were deformed. It was determined through this study that the conditions of deformation in the Grenville Front were not sufficient to cause zircon strain and therefore zircon strain chronometry is not an applicable method in this case. Justifications for these findings and suggestions for further work are provided.

Acknowledgements

First and foremost, I'd like to thank my supervisors, Dazhi Jiang and Desmond Moser, for their help throughout this process. I thank them both for their patience and understanding during the last 2.5 years as well as the support and guidance they have provided me. I'd also like to thank Amy Wickham. Amy has been an important part of my graduate experience and I truly appreciate her support in the last year.

In addition, my thanks go out to my fellow classmates that have been instrumental to my success. I'd like to thank Lucy Lu for joining me in the field and helping me immensely with the Matlab component of my results. Lucy has provided a great amount of support as I have been working towards this degree. Giancarlo Jones helped me learn the ropes of the ZAPLab. He answered many of my questions about zircon and equipment in the ZAPLab. I also appreciate Giancarlo taking the time to discuss his research with me which I was able to reference in my studies.

I would not have been able to complete my research without Ivan Barker's technical assistance in the ZAPLab. I appreciate his time and effort in guiding me through the analyses process.

I'd like to thank my trivia team, Giancarlo Jones, Ankit Bhandari, Gabriel Arcuri and Philip Reger for the fun and distraction, it was greatly appreciated, even though we lost 99% of the time.

My final thanks must go to my friends and family. To my parents, David and Sandi Petkau, thank you for your endless support during this process and for always having my back. To my wonderful boyfriend, Alex Stap, thank you for all the pep talks and encouraging words that helped me immensely to persevere. And to my friends, thank you for always being there for me for the past 2.5 years, your support has meant the world to me.

Table of Contents

List of Tables

Table of Figures

List of Appendices

Chapter 1

1 Objectives and Geological Background

1.1 Introduction

The Grenville Front Tectonic Zone (GFTZ) is a region of complex polyphase deformation that is yet to be completely understood with regard to the absolute age of different deformation fabrics. Previous work by Li (2012) in the Grenville Front near Sudbury and the northeast Britt Domain has established a sequence of deformation through overprinting relationships. The present thesis sets out to test whether or not deformation conditions were sufficient to deform the accessory geochronology mineral zircon such that it could be used to date the deformational event in which the zircon was strained. This thesis investigates the microstructures associated with the regional deformation in the GFTZ and estimates the deformation differential stresses using grain size distribution of co-existing quartz in order to evaluate the deformation effect on zircon. The significance of this study is twofold. First, while the Grenville orogeny has been studied for decades, this will be the first investigation of quartz piezometry in the GFTZ. Estimating stress in the Grenville Front adds to our interpretation of the Grenville orogeny and will help build a clearer tectonic history. Second, these results further our general understanding of deformation geochronology and its potential for dating lithosphere tectonic fabrics. I will introduce and compare three piezometer calibrations for stress determination using grain size as well as evaluate the limitations of using zircon to date deformation.

This thesis is organized in the following way. Chapter 1 will present the geological background of the project and a description of the study area. Chapter 2 will be a review of the methods used in this thesis, microstructural investigation of in situ zircon and methods of stress

determination. Chapter 3 will explain the materials and methods used in this thesis. Chapter 4 will present the results of the microstructural investigation and quartz grain size measurements. Chapter 5 will include interpretations of stress estimates using quartz piezometers and discuss the applicability of dating Grenvillian deformation with zircon. Finally, the Chapter 6 discussion will summarize the findings of this report.

1.2 The Grenville Province (Orogeny and Geology)

The Grenville Province resulted from a series of accretionary and collisional events associated with the collision of the North American craton, Laurentia, with magmatic arcs and continental terranes linked with the assembly of supercontinent Rodinia (e.g. Rivers, 1997; Tollo et al. 2004; McLelland et al., 2010). These events have been resolved into three separate orogenies. The early- to mid-Mesoproterozoic Elziverian and Shawinigan orogenies (1250-1190 Ma and 1190-1140 Ma, respectively) which affected accreted terranes in the southwestern Grenville Province and the late-Mesoproterozoic to early-Neoproterozoic Grenvillian orogeny which is further subdivided into two orogenic phases: the Ottawan Phase (ca. 1080-1020) and the Rigolet Phase (ca. 1000-980) (Rivers, 1997, 2008). The Grenville Province lacks overprinting from regional metamorphism since the Grenville orogeny and thus is inherently useful in unravelling the orogeny's complicated tectonic history (Tollo et al., 2004).

The Grenville Front represents the northernmost boundary of penetrative deformation resulting from the Grenville orogeny and separates the Grenville Province from the Southern and Superior Provinces near Sudbury, Ontario (Lumbers, 1971). Rivers et al. (1989) divided the Grenville orogen into three litho-tectonic belts, the Parautochthonous Belt, the Allochthonous Polycyclic Belt and the Allochthonous Monocyclic Belt (Figure 1-1). Immediately adjacent to

the Grenville Front is the Parautochthonous Belt. The Parautochthonous Belt represents the reworked rocks of the foreland, increasing in metamorphic grade southeastward from the Grenville Front. The Allochthon Belt follows the moderate to shallow southeast dipping Allochthon Boundary Thrust and overlies the Parautochthonous Belt. It is characterized by its exotic nature and evidence of having undergone pre-Grenvillian orogenic cycles. The Allochthon belt is subdivided into a polycyclic and a monocyclic domain. The Allochthon Polycyclic Belt shows evidence of tectonic activity from orogenies pre-dating the Grenville Orogeny. The Monocyclic Belt Boundary Zone is a major shear zone that separates the polycyclic terrane of the Allochthon Polycyclic Belt from the monocyclic rocks of the Allochthon Monocyclic Belt, the latter being affected exclusively by the Grenville orogeny.
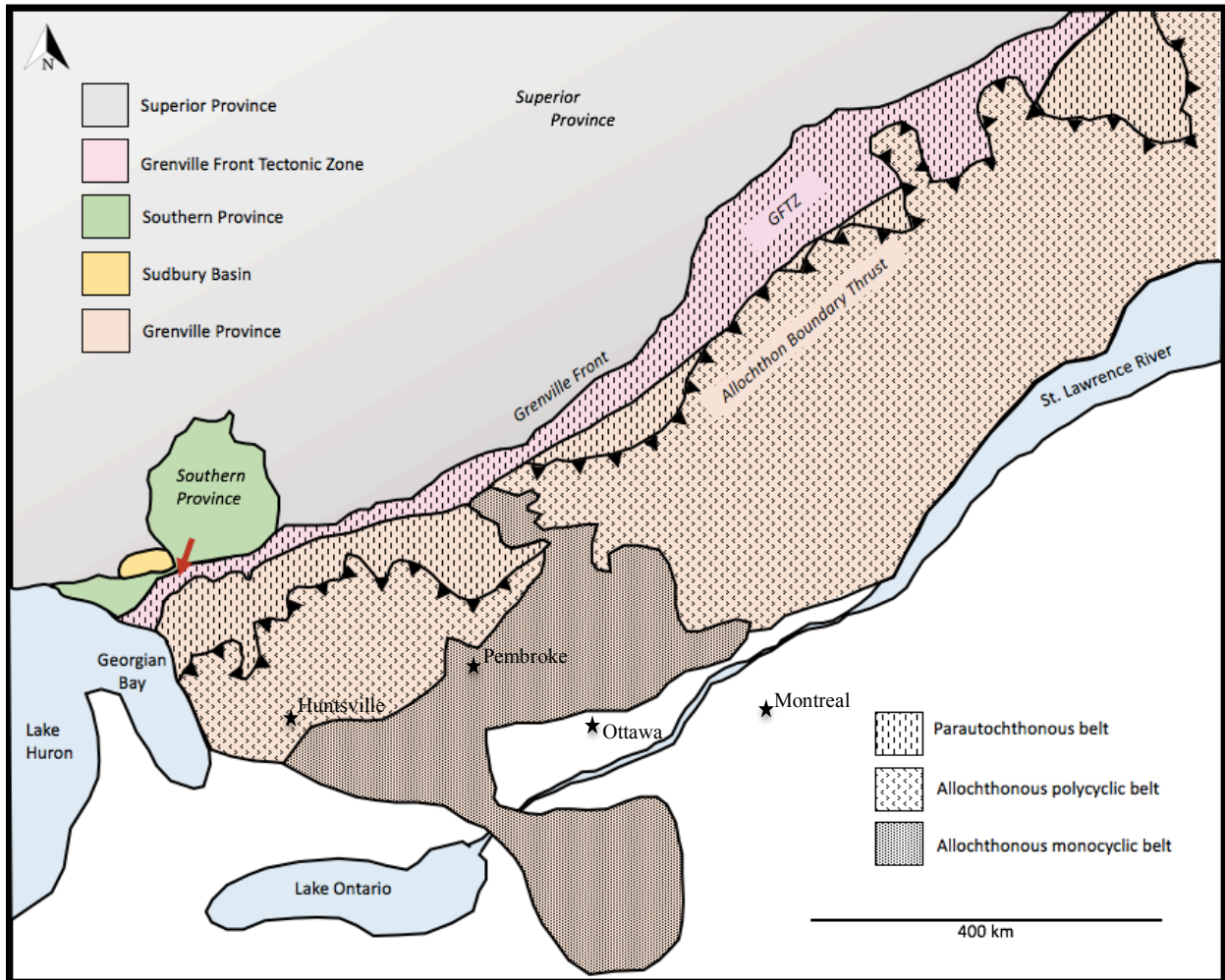
Figure 1-1. Lithotectonic map compiled from Carr et al. (2000) and Li (2012) using lithotectonic divisions by Rivers et al. (1989). Red arrow indicates study location.

1.3 The Grenville Front Tectonic Zone in the Sudbury area and Polyphase Deformation

The Grenville Front is exposed for ~2000 km in a northeast trend at 065° to 070° and consists mostly of gneisses and migmatites with considerable amounts of anorthosite and other plutonic rocks that have been subjected to deformation and metamorphism (Rivers et al., 1989; Davidson, 1984). The Grenville Front also includes lesser amounts of metavolcanics and metasedimentary rocks (e.g. Davidson, 1984). The Grenville Front Tectonic Zone (GFTZ), a high-strain zone adjacent to the Front (Lumbers, 1971; Wynne-Edwards, 1972), will be studied in detail in this thesis. The GFTZ has a complex history of polyphase deformation, extensive uplift, faulting, mylonitization, and metamorphism (Corfu and Easton, 2000). Li (2012) identified that three major deformational phases have affected this region between 1079 and 953 Ma. The deformational phases are referred to as D_1, D_2 and D_3. It is important to note that each deformational phase consists of a progressive deformational event that may develop many generations of structures. In the Grenville Front, the three deformational phases of the Grenville Front are associated with a total of four generations of folding and two generations of transposition foliation. The final phase of deformation, associated with the Rigolet phase of the Grenville orogeny (Li, 2012), gave rise to the features that are recognized today as the GFTZ. The structural features in the GFTZ are summarized in Li's (2012) block diagram (Figure 1-2) and are described in detail using Li's (2012) terminology and classifications below.
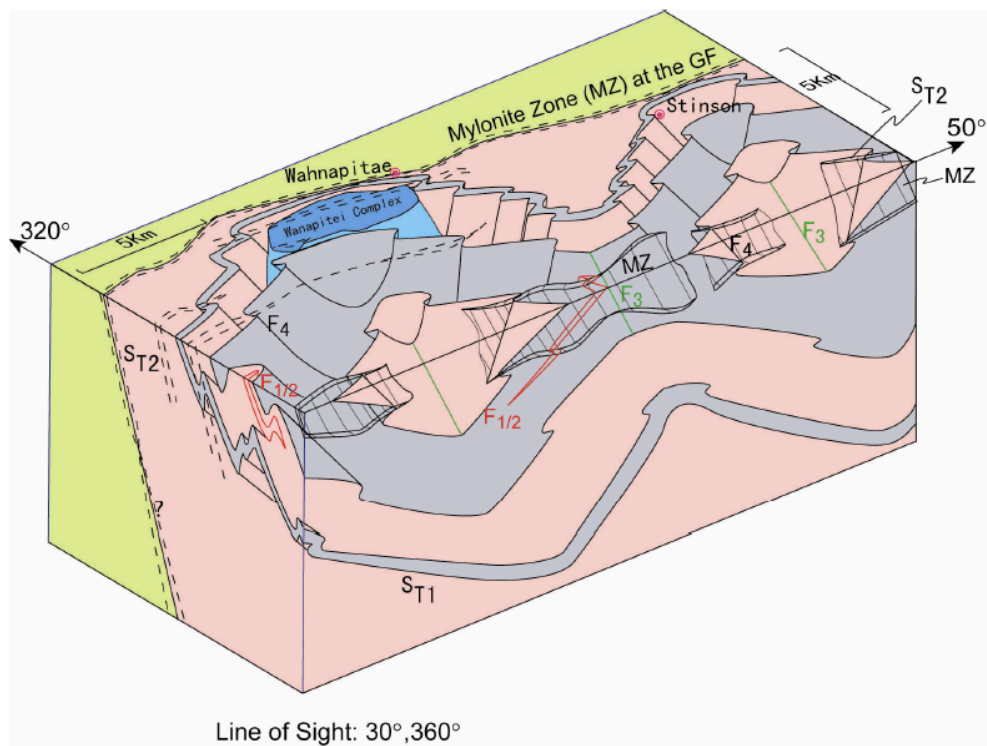
Figure 1-2. Block diagram from Li (2012) showing deformation structures in three dimensions.

The first phase of deformation (D_1) includes two generations of isoclinal folding (F_1, F_2) and the formation of a transposition foliation (S_{T1}) as a result of the Ottawan orogenic phase (Li, 2012). F_1 and F_2 are generally rootless intrafolial folds. Due to their similar styles, F_1 and F_2 can only be distinguished when an overprinting relationship is observed. When this overprinting relationship is indeterminable, they are referred to as $F_{1/2}$ (Figure 1-3). The orientation of $F_{1/2}$ varies with S_{T1} foliation and overprinting by later fold generations. When overprinting is not observed, F1/2 and ST1 are shallowly dipping. These fabrics are consistent with the features of the high-grade nappe association (HGNA) described by Williams and Jiang (2005) and therefore D_1 is interpreted to be reflect a crustal scale shear zone (Li, 2012). Li (2012) identified the formation of S_{T1} in D_1 to be between 1080 and 1030 Ma.

6

Figure 1-3. $F_{1/2}$ rootless intrafolial fold in the Wanapitei region. Solid line indicates axial trace, dashed line indicates $S_{T1/2}$ transposition foliation. Fold hinge orientation 30→213.

The second phase of deformation (D_2), resulting from NW-SE extension, produced northwest-trending regional scale folds (F_3) (Culshaw et al., 1994; Li, 2012). F_3 folds are generally open to tight with larger interlimb angles than $F_{1/2}$ (Li 2012). F_3 folds cannot be observed on outcrop due to their large amplitudes usually greater than 5 km; F_3 folds are visible in satellite images and regional maps (ex. Figure 1-8) (Rivers et al. 1989; Davidson, 1995; Harris et al., 2002; Schwerdtner et al., 2016). Li (2012) constrained the timing of F_3 folds in D_2 to be between 1028 and 1018 Ma.

The last dominant phase of deformation (D_3) was a result of NW-SE shortening in the Rigolet orogenic phase (Li, 2012). This phase is the last major phase of deformation to affect this region; the folds, foliation, and mylonitization resulting from D_3 define the high shear zone that is recognized as the GFTZ. This tectonic shortening resulted in the development of mylonitic foliation at the Front and overprinting of the previous fold generations (F_1-F_3) with folds of northeast trend (F_4). Closest to the Front, F_4 folds are tight with small interlimb angles (Figures

1-4,1-5) and are typically chevron style. Localized high strain zones of the D_3 generation are common and, in such zones, F_4 is transposed resulting in a second generation of transposition foliation (S_{T2}), parallel to the axial plane of F_4. D_3 also resulted in a NE-SW trending mylonite zone adjacent to the Grenville Front. More distally, F_4 folds have larger interlimb angles (Figure 1-5). The overprinting of D_3 on D_2 is not usually observable on an outcrop scale due to the difference in fold-scale (Li, 2012). However, D_3/D_1 overprinting can be distinguished by the difference in fold style (Figures 1-5,1-7). The style and consistent orientation of F_4 imply that it was a separate and overprinting event on F_3 (Li, 2012), corroborating the hypothesis that the GFTZ was a result of polyphase deformation (Brocoum and Dalziel, 1974) rather than progressive top-to-the-NW shearing (La Tour, 1981). Li (2012) suggested the timing of deformation and mylonitization in D_3 to be between 1000 and 953 Ma.
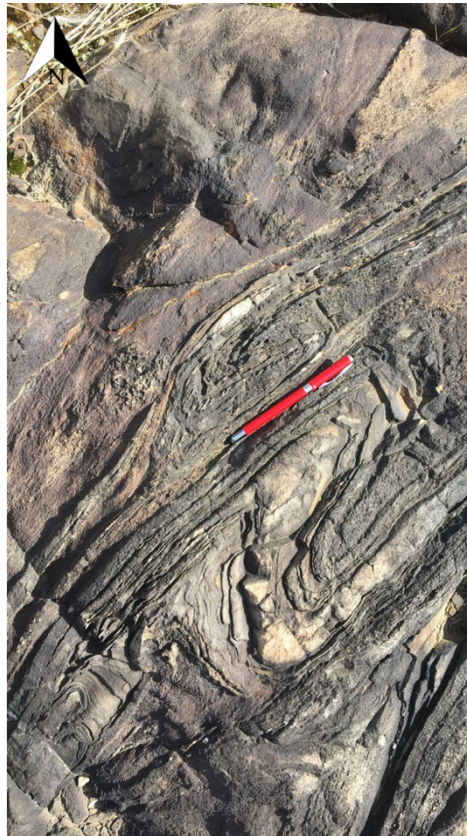
Figure 1-4. Tight F_4 folding in Wanapitei region. S_{T1} makes up fold surface. Axial trace trends NE-SW.
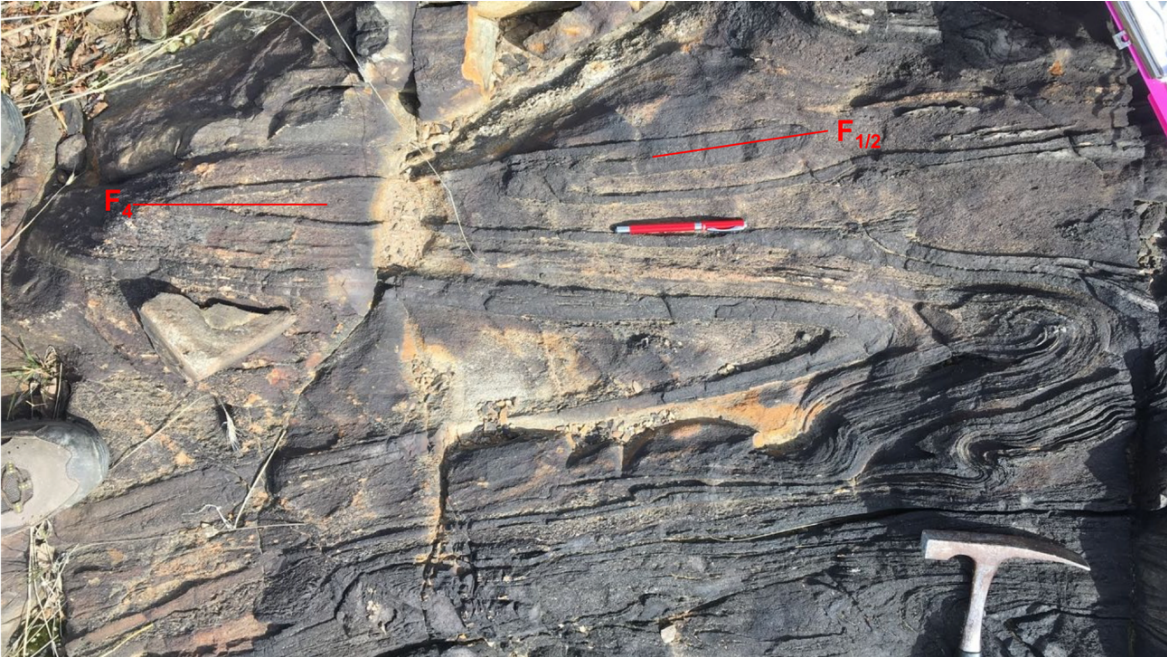
Figure 1-5. Isoclinal F_4 fold overprinting isoclinal $F_{1/2}$ in Wanapitei country rock. Solid lines indicate axial trace. F_4 axial trace trends NE-SW.

Figure 1-6. F_4 fold with larger interlimb angle and F_4 parasitic fold in migmatitic gneiss with syn-D_3 pegmatitic intrusion. Approx. 12 km SE of study area.

Figure 1-7. F_4 fold overprinting $F_{1/2}$ in country gneiss. Solid lines indicate axial trace, dashed line shows $F_{1/2}$ fold surface.

Lumbers (1971) reports an assortment of dykes that are common in the GFTZ. Quartz monzonite dykes cut early and mid-Precambrian rocks and are deformed and recrystallized by the subsequent polyphase deformation. They are found within a kilometer NW and SE of the Grenville Front boundary. Recrystallized and deformed granite pegmatite dykes are present within a few kilometres SE of the boundary. In the gneissic country rock of the study area, recrystallized and deformed granite pegmatite dykes were emplaced syn-tectonically with D_3 deformation (Figure 1-8).

Figure 1-8. Pegmatite dyke intruding D₃ fold surface in migmatitic gneiss.

1.4 Study Area and Sample Setting (Wanapitei Complex)

This study includes samples from the Wanapitei Complex and surrounding country rock. The Wanapitei Complex is an igneous pluton described as a 6 km by 2.5 km oval-shaped body with long axis trending northeast and is located about 0.4 km southeast of the Grenville Front near Sudbury, Ontario (Rousell and Trevisiol, 1988) (Figure 1-9). The Wanapitei Complex was mapped by Rousell and Trevisiol (1988) as primarily injection breccia, which is a magmatic breccia formed during intrusion (Tă maş, 2002; as cited in Tă maş and Milési, 2002), with some felsic dykes and hornblende gabbro in the southwestern two-thirds and recrystallized gabbro, hornblende gabbro, gabbronorite and norite in the northeastern most section. The complex has been subjected to amphibolite facies metamorphism (Figure 1-10). The crystallization age of gabbronorite in the Wanapitei Complex was determined to be 1747 +6/-5 Ma based on U-Pb

zircon geochronology, the zircons from the complex have a Grenvillian-aged lower intercept age on a concordia plot (996 Ma) (Prevec, 1995). Geochronology was completed on extracted zircon grains described as having subhedral to anhedral prismatic forms. Due to the pre-Grenvillian emplacement of the Wanapitei Complex, this complex is of particular interest when unravelling the deformational history of the GFTZ.
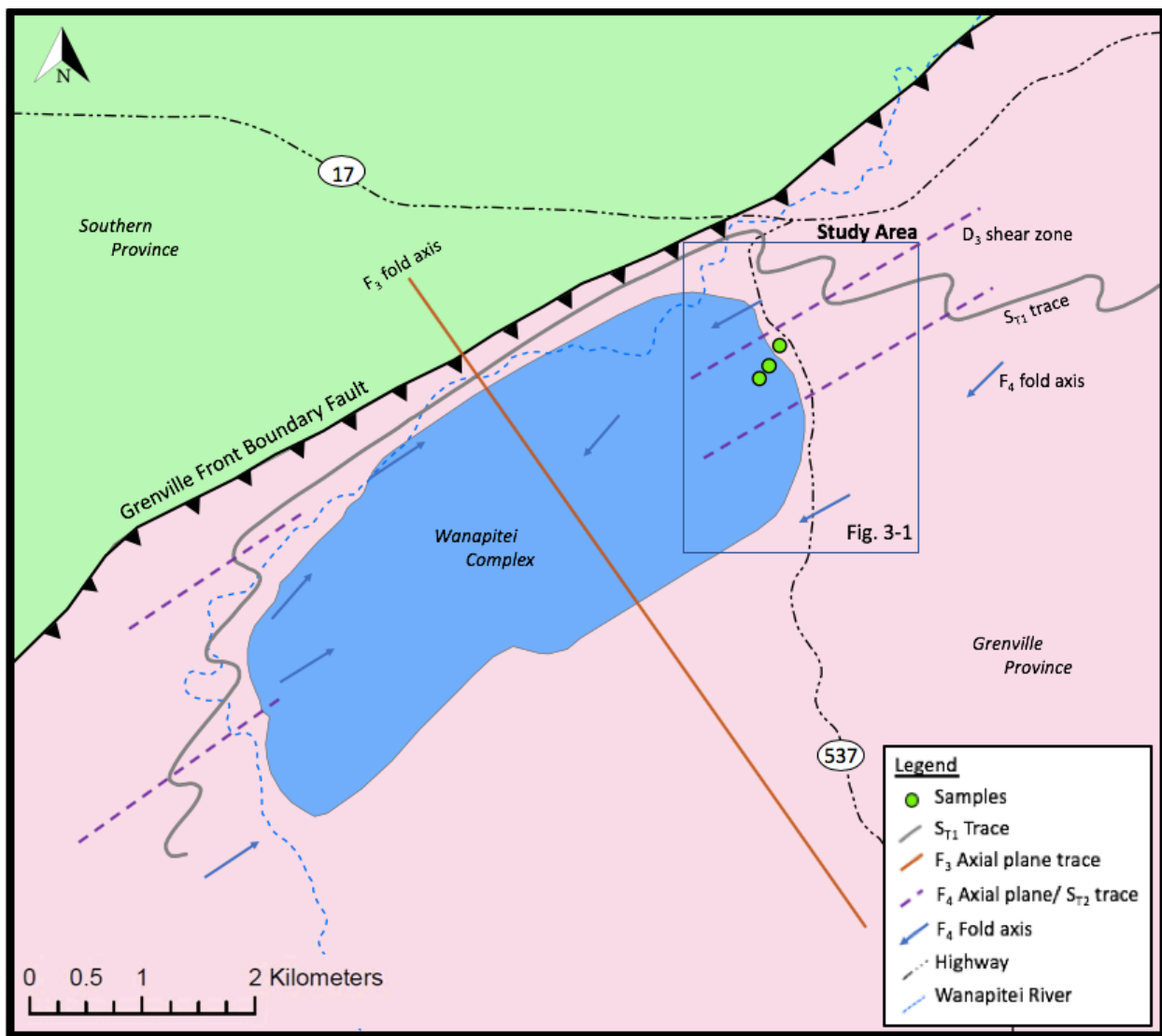
Figure 1-9. Structural map of area surrounding the Wanapitei Complex modified from Li (2012).

Figure 1-10. Wanapitei Complex amphibolite. (A) Massive garnet amphibolite. (B) Garnet amphibolite with plagioclase pressure shadows. (C) Massive garnet amphibolite adjacent to highly strained amphibolite.

Li (2012) proposed constraints on the timing of deformation in the GFTZ and confirmed that the Wanapitei Complex metagabbro was subjected to all three phases of deformation. Li (2012) correlated regional structures dated by Corrigan et al. (1994) and Ketchum et al. (1998) in the Shawanaga and Parry Sound Domains, ~100 km southeast of the Wanapitei Complex, to Grenvillian structures in the GFTZ. Along with U-Pb dating of zircons in four samples (two of a dioritic dyke in the GFTZ, one of the Wanapitei Complex and one of a pegmatite dyke east of the Wanapitei Complex), Li (2012) proposed the timing of deformation in the GFTZ to be: D_1 (S_{T1} foliation): 1079-1030 Ma, D_2 (F_3 folds): 1028-1018 Ma and, D_3 (F_4 and mylonite zones): 1000-953 Ma. U-Pb dating of separated zircons was completed by targeting of distinct growth zones using cathodoluminescence (CL) imaging. In the Wanapitei Complex sample, Li (2012) dated 21 spots on extracted zircon, 18 of which were interpreted to be metamorphic

recrystallization of relict igneous grains due to their irregular shapes and patchy zonation. U-Pb geochronology of these zircon grains suggested the timing of this deformation within the complex to be 1079-953 Ma. Two spots on one grain revealed an igneous age of more than 1800 Ma which was interpreted to be an inherited grain from the country rock. One additional spot on an igneous zircon with partial recrystallization corresponded to the crystallization age of the complex. The complex is crosscut by mafic and felsic dykes that were subjected to the same deformation as the complex (Li, 2012).

The country rock of the complex is comprised of supracrustal rocks most likely derived from the Huronian Supergroup (Ames et al., 2005), the age of the country rock is unknown. In the area, country rock is primarily garnet-biotite gneiss and migmatized garnet-biotite gneiss and metasedimentary rocks with pegmatitic intrusions (Figure 1-10, 1-11).
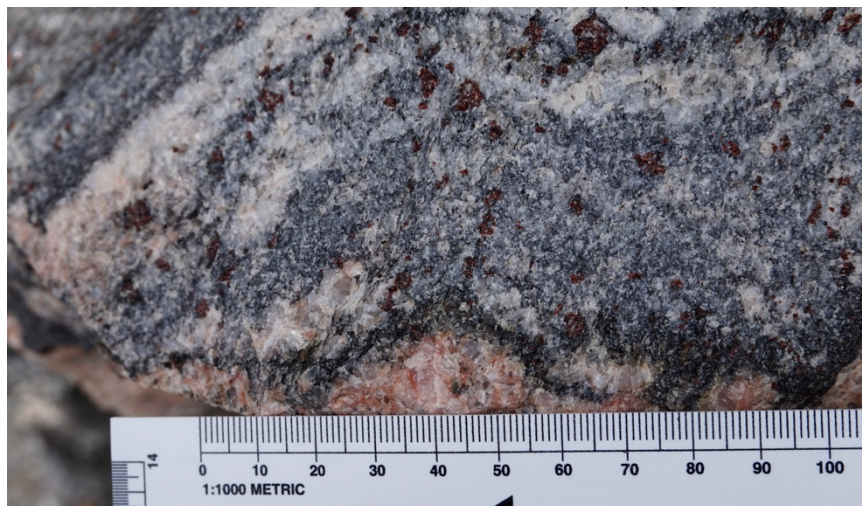
Figure 1-11. Migmatized garnet-biotite gneiss of the country rock.
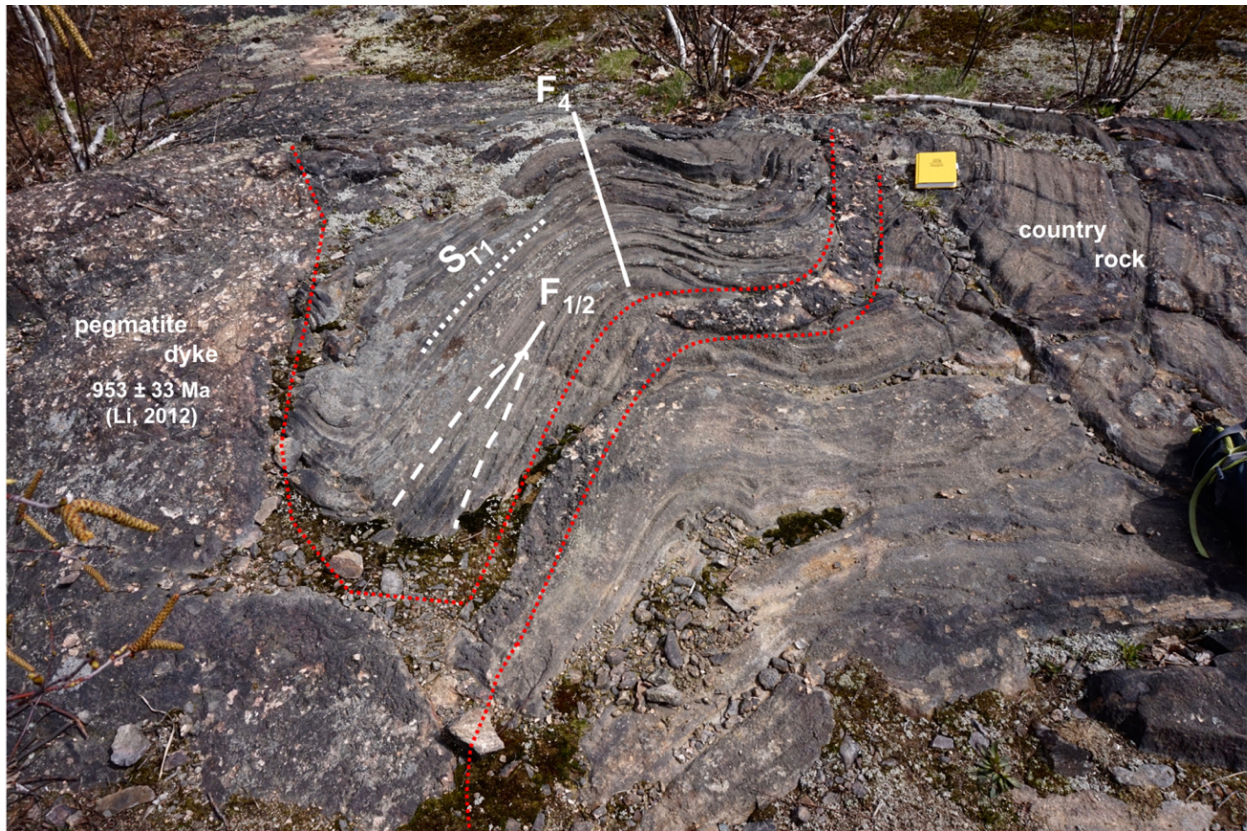
Figure 1-12. Pegmatite dyke (red dotted line) folded by D_3 (F_4) in marginal gneiss east of the Wanapitei Complex. $F_{1/2}$ and S_{T1} overprinted by F_4. Pegmatite dyke emplacement estimated to be 953 ± 33 Ma (Li, 2012).

In this thesis, microstructural investigations are conducted on four samples from D_3 high strain zones. Samples Wcc-2 and Wcc-4m are hornblende metagabbro collected from the Wanapitei Complex (Li, 2012), sample Wcc-4g is a granitic dyke that is believed to have crosscut the complex pre/syn-D_3 deformation (Li, 2012), and W2-2 is a garnet-biotite gneiss collected from the country rock. The next chapters will explore these samples in detail to assess the feasibility of constraining a higher resolution temporal history of D_2 and D_3 deformation in the area by in situ zircon analysis and stress estimates of the deformation conditions.

Chapter 2

2 Review of methods

A comprehensive characterization of the Grenville Front deformation requires investigation to take place at multiple scales. Work by Li (2012) described the regional deformation of the Wanapitei area and performed U-Pb zircon geochronology on several samples. In situ microstructural analysis of the textures and zircons from samples in this area will allow the re-interpretation of earlier zircon ages within their deformational context as well as the investigation of additional coeval phases. If zircon grains show evidence of deformation, discordant dates have a significant probability of defining the timing of deformation in the Wanapitei Complex. Lack of strain, however, would indicate that deformation did not reach the extent to cause permanent deformation in zircon grains or that zircon crystallization post-dated deformation. Correlation of zircon deformation to structural features and corresponding discordant ages would allow for more confident estimations of the timing of deformation. If they do not exhibit structural evidence of the deformational events of the Grenville orogeny, the discordant dates interpreted to be the timing of deformation by Li (2012) may not be accurate. A stress estimation of the samples using quartz piezometry will provide insight into the factors that control zircon deformation.

2.1 Microstructural Investigation of in situ Zircon

Zircon ($ZrSiO_4$) can be examined microstructurally and chemically to reveal information about both the zircon and its host rock's history. It is one of the most common accessory minerals used for radiometric dating. The long half-life of the U-Pb system makes it particularly useful for

dating old events that the radiometric dating of other trace elements cannot. Additionally, zircon's high resistance to chemical and mechanical alteration makes it very durable and able to survive considerable metamorphism. This makes zircon a prime target for isotopic dating in deformed and metamorphosed rock such as that found in the Grenville Front Tectonic Zone (GFTZ).

The importance of microstructural analysis of chemical and orientation variations in grains in tandem with U-Pb dating has become universally acknowledged as the internal morphology of zircon is highly variable and can provide insight about the formation of the mineral (e.g. Gagnevin et al., 2010). Electron microscope imaging using cathodoluminescence (CL) or back-scattered electrons (BSE) can be used to decipher different growth domains and internal textures, thus allowing conclusions to be made on the origin of the zircon, strain and chemical alteration (Hanchar and Miller, 1993; Corfu et al., 2003). The integration of these microanalytical techniques combined with in situ geochronology has resulted in the capacity to date tectonothermal events with improved accuracy. Analysis of metamorphic growth zones using high-resolution ion-microprobe has allowed temporal constraints to be made in polymetamorphic zircon (e.g. Möller et al., 2003; Liu et al., 2013; Liati et al., 2016). Additionally, investigations of the effects of plastic deformation on trace element mobility has determined that U-Pb isotopic age may be reset through enhanced trace element diffusion (Reddy et al., 2006; Piazolo et al., 2016); and therefore, used to date deformational events (e.g. Moser et al., 2009; Piazolo et al., 2012; Kovaleva et al., 2016; Kovaleva et al., 2017). The method of dating strained lattice domains in zircon is referred to as zircon strain chronometry (e.g. Moser et al., 2009). There is a significant interest in the relationship between plastic deformation in zircon, subsequent isotopic age resetting and regional deformation kinematics as

it can be difficult to confirm the peak-metamorphism origin of metamorphic zircons and correlate them accurately to a target event (Möller et al. 2007; Kohn et al., 2015). Therefore, constraining the relationships of zircon strain chronometry is key to dating areas of multiple metamorphisms and specific deformational events with zircon.

A study by Reddy et al. (2006) was the first to identify crystal-plastic deformation of zircon under crustal conditions and deformation enhanced fast-diffusion of trace elements in zircon. This led to the recognition of the importance of intra-grain deformation in isotopic dating. Moser et al. (2009) demonstrated that in zircon grains exhibiting crystal-plastic deformation, Pb loss can occur at an accelerated rate compared to in a pristine lattice (e.g. Moser et al., 2009). Elemental redistribution occurs through pipe diffusion along dislocation arrays. Pb and other trace elements diffuse rapidly along these arrays while isolated dislocations or closed networks act as structural sinks where trace elements pile up (Piazolo et al., 2016). In this process, Pb is "lost" from the dislocation, resulting in a discordant age of deformation. Zircon strain chronometry has been completed in cases of lattice distortion related to impact events (Moser et al., 2009; Moser et al., 2011); seismicity (Kovaleva and Klötzi, 2017); and in deformation due to regional tectonics (Piazolo et al., 2012; MacDonald et al., 2013). This new avenue holds the potential to improve the geochronological resolution of tectonic events significantly. However, the accuracy of this method and the prevalence of zircon lattice strain in regional tectonics are currently unconfirmed.

Piazolo et al. (2012) identified three lattice distortion patterns in deformed zircon porphyroclasts (0.8 – 1.5 mm); similar patterns are described in smaller zircon grains (10 – 50 μm) by Kovaleva et al. (2014). *Type I* lattice distortion involves gradual lattice bending with progressive orientation change of ~0.3°/μm (Piazolo et al, 2012) or 10-25° of misorientation

within a single grain (Kovaleva et al., 2014). *Type II* distortion is an indent-type pattern in which distortion is concentrated in a concentric pattern around a contact point that results in half-circle shaped deformation zones of ~0.8-1°/μm (Piazolo et al., 2012) or ~25-40° of misorientation within a single grain (Kovaleva et al., 2014). *Type III* distortion is described as localized crystal-plastic deformation due to internal heterogeneities or coupling with a strong host; *Type III* distortion forms a network of low angle boundaries and subgrain boundaries separating grains with 3-10° of internal distortion. The U-Pb system of deformed grains in Piazolo et al. (2012) displayed discordance broadly correlating to an amphibolite facies reworking, with most precise dating from *Type I* and *II* patterns and a broader range in values from *Type III* patterns. Kovaleva et al. (2017) also concluded that gradually bent *Type I* and *Type II* patterns may accurately date ductile deformation of zircon. However, caution must be used when dating deformed zircon grains due to the large variability in U-Pb ages (Piazolo et al. 2012).

Despite the usefulness of zircon strain chronometry, this method of age determination is only pertinent in areas where zircon lattice distortion is observed and can be sufficiently analysed. For example, in a study from the Lewisian gneiss complex of northwest Scotland, MacDonald et al. (2013) found that only 5% of 99 zircon grains exhibited lattice distortion, a fraction of which were able to be linked temporally to a deformational event. Defining sample criteria and determining the governing conditions of lattice strain in zircon are essential to establish the applicability of zircon strain chronometry and the circumstances under which it can be employed. Moser et al. (2009) outlined sample criteria required for zircon strain chronometry; (1) Zircon must be devoid of radiation damage that occurs below the closure temperature of ~150°C as it can result in discordance from Pb-loss; (2) Zircons must be studied in situ to correlate ductile deformation with deformation fabric, and (3) U-Pb data must be of sufficient

analytical and spatial resolution so that a correlation of discordance with zircon microstructure can be established. Samples should also be devoid of fractures, high- and low-angle boundaries and pores, and analyses should be done ~5 μm from the deformation front and 5-10 μm from boundaries to avoid contamination of results (Kovaleva et al., 2017). The factors that control lattice distortion also need to be investigated to determine how widespread its applicability is. Possible factors on the presence and pattern of zircon lattice distortion within natural shear zones include: temperature, distribution, magnitude and direction of differential stress, grain shape and host matrix (Kovaleva et al., 2014), internal mechanical weakness and grain orientation (Kovaleva et al., 2016; Kovaleva et al., 2018).

Yield strength is the stress that exceeds the elastic limit of a mineral and the point at which permanent plastic deformation occurs (Passchier and Truow, 1996). The yield strength of a mineral is affected by temperature and strain rate; therefore, the yield strength of zircon at crustal conditions is an important foundation for defining the parameters that control zircon lattice distortion. Although zircon is universally recognized as a strong mineral (bulk modulus 203±13 GPa), zircon is more susceptible to differential stress than expected, with a lower shear modulus than olivine (Morozova et al., 2017). Experiments have explored the yield and tensile strengths of zircon at room temperature and temperatures higher than 980°C, there is a gap of knowledge currently regarding zircon lattice strength between these temperatures (Figure 2-1). Yield strengths have been defined as Y=1830 MPa by shock compression at room temperature (Mashimo et al., 1983), and 400 – 5000 MPa at room temperature in the confining pressures range between 1 and 32 GPa using a diamond anvil cell (Morozova et al., 2017). Wygant (1951) identified the yield of dislocation creep of zircon in a high-T torsion apparatus to be 8.9 MPa at 1100°C. Tensile strengths have also been explored. Gangler (1950) identified the short time

elevated-temperature tensile strength of zircon to be 60 MPa and 25 MPa at 980°C and 1200°C, respectively. Similarly, Glenny (1956) found tensile strengths of 42 MPa at 980°C and 21 MPa at 1200°C. In these tests, tensile strength was defined as the maximum tensile stress the material could withstand before brittle fracture/rupture. Given this definition and the general stress-strain curve, the tensile strength may be treated as an approximate boundary between the plastic behaviour of zircon and brittle failure. Therefore, tensile strength is considered an upper limit of stress in zircon plastic deformation.
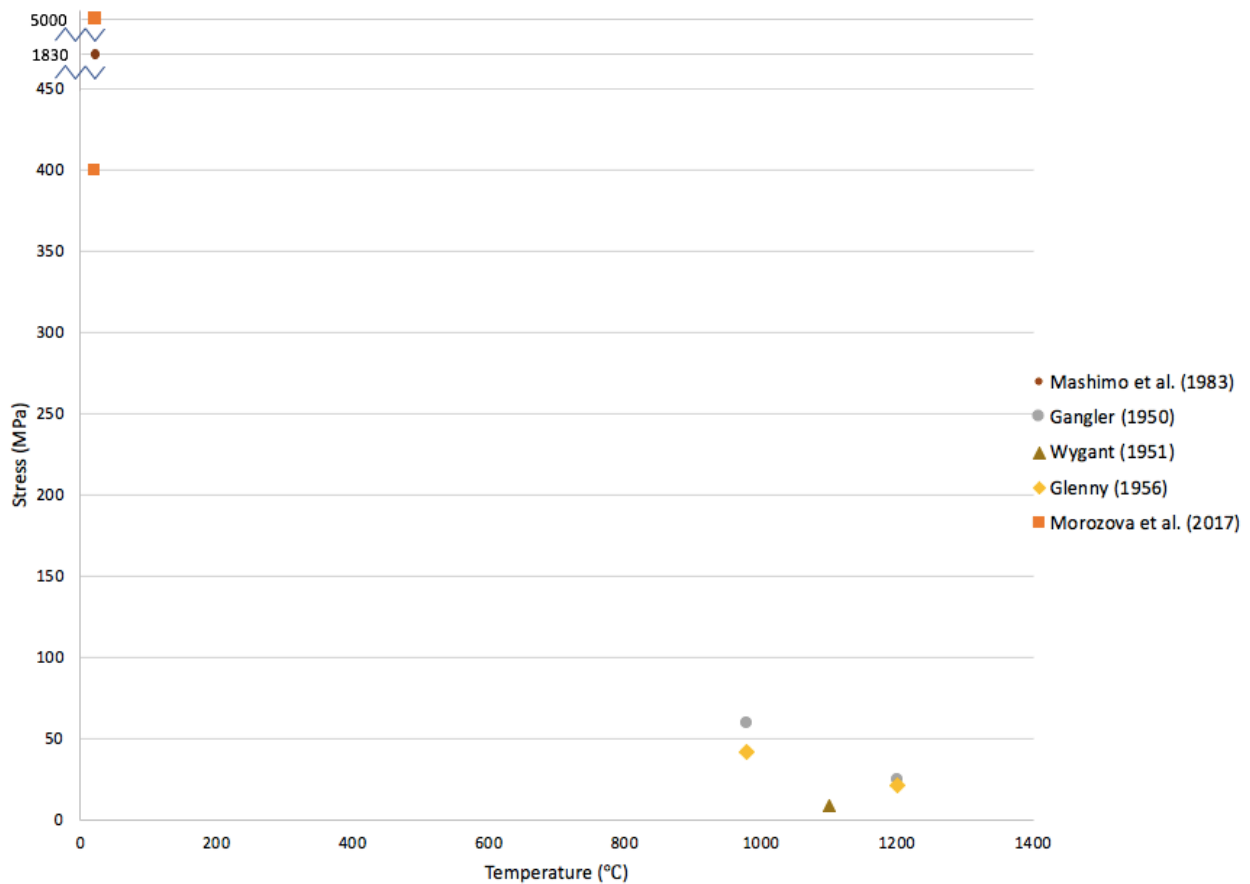
Figure 2-1. Yield and tensile strengths of zircon.

This study explores the possibility of better correlating the dates previously obtained to the final D$_3$ deformation. In situ investigation of zircon within D$_3$ structures using microstructural imaging will allow their internal morphology within specific kinematic features to be studied, drawing conclusions on the presence and conditions of zircon lattice distortion. Zircon grains deformed in D$_3$ would provide the potential to date this phase of deformation with more accuracy than previous work. This study will also enhance the current knowledge of the factors that influence lattice strain in zircon.

2.2 Methods of stress determination: A review of theory and methods

2.2.1 Using recrystallized grain size to determine stress

The Grenville Front Tectonic Zone (GFTZ) is the locus of a series of deformational events resulting from the Grenville orogeny. Deformation and metamorphism in the GFTZ are widespread and can be seen at various scales. On a microstructural scale, the effects of deformation can be observed through recrystallized grain size. Recrystallization is a microstructural response to deformation that lowers the internal free energy of a mineral by producing new finer grains (Passchier and Truow, 1996). Recrystallization is separated into two forms. First, dynamic recrystallization is synchronous with deformation and results in grain size reduction. Dynamic recrystallization is interpreted to occur through two distinct processes: (1) subgrain rotation and (2) grain boundary migration (Lloyd, 1994). Subgrain rotation occurs when a grain is progressively strained and the increase in misorientation angle results in the formation of a new grain boundary. The critical angle for quartz where this formation occurs is approximately 10 degrees (White, 1977). Subgrain rotation is favoured by high deviatoric stress

and low temperatures while Grain boundary migration generally occurs at higher temperatures (Winter, 2010). Grain boundary migration produces irregularly shaped grains as a result of relatively strain-free grains with a low density of defects consuming grains with higher defect density (Lloyd, 1994). Second, static recrystallization, or annealing, is a recrystallization process that occurs at elevated temperatures devoid of deformation (Urai et al., 1986). During annealing, grain growth results in polygonal grains with straight boundaries (Heilbronner and Tullis, 2002). This process reduces the surface area of affected grains thus lowering the internal energy state of the grains (Otani and Wallis, 2006). Dynamic recrystallization occurs to reduce the effects of strain and thus can be used to interpret the deformational history of a rock including flow stress and deformation temperature (e.g. Stipp et al., 2002; Stipp et al., 2010). The recrystallized grain size of several samples will be used to investigate the microstructural effects of deformation produced by the Grenville orogeny and extrapolate this information to draw conclusions on the microstructural response of other minerals in D_3 deformation.

Paleopiezometry utilizes structural characteristics of a rock to estimate the differential stresses at the time of deformation. In this instance, recrystallized grain size piezometry will be utilized. Twiss (1977) introduced the original theory behind grain size piezometry. In the theoretical equation, Twiss (1977) described a relationship where recrystallized grain size and subgrain size were dependent on differential stress and insensitive to temperature. The general form of recrystallized grain size piezometers based on Twiss' (1977) theory is:

$$d_s = A \cdot \sigma^{-m} \tag{1}$$

where d_s is steady state recrystallized grain size in μm, σ is stress in MPa and A and m are empirically determined constants (Austin and Evans, 2007). Since the grain size piezometer's introduction, recrystallized grain size piezometers have been calibrated for many materials

including quartz (Stipp and Tullis, 2003), olivine (Ross et al., 1980), halite (Guillopé and Poirier, 1979), calcite (Schmid et al., 1980), and feldspar (Post and Tullis, 1999). New models for grain size piezometry have also been introduced (e.g. Austin and Evans, 2007; Shimizu, 1998). Differences in piezometric models and calibrations arise from debates related to dependence of recrystallized grain size on internal and external factors such as: grain growth kinetics, temperature, creep activation energy, grain size distribution of the deforming aggregate and operating recrystallization mechanisms (e.g. Stipp et al., 2003; De Bresser et al., 2001; Austin and Evans 2007; Shimizu, 2008, 2012). Though the relationship between recrystallized grain size and stress state has been extensively studied, no universally accepted relation exists presently. Additionally, piezometers have usually been calibrated based on experimental results and have unknown accuracy when extrapolated to natural samples. Three prominent studies are the paleopiezometers of Stipp and Tullis (2003) and Shimizu (2012); and the paleowattmeter of Austin and Evans (2007). These three relations will be reviewed and compared in the following section.

2.2.2 Stipp and Tullis (2003)

While conducting a calibration of the paleopiezometer of Twiss (1977), Stipp and Tullis (2003) were the first to recognize the importance of the different mechanisms of dynamic recrystallization in piezometric calibrations. Stipp and Tullis (2003) used the dislocation creep regimes of Hirth and Tullis (1992) to investigate the dependence of grain size on differential stress in different dynamic recrystallization mechanisms.

Hirth and Tullis (1992) identified that deformed quartz is accommodated by three regimes of dislocation creep. Each regime is associated with characteristic microstructures resulting from dynamic recrystallization. *Regime 1* occurs under low temperatures and fast strain

rate. Under this regime, grain boundary migration (GBM) acts as the dominant recrystallization mechanism. The transition to *Regime 2* occurs with an increase in temperature or a decrease in strain rate. This, in turn, means a decrease in flow stress. In *Regime 2*, recrystallization is controlled by subgrain rotation (SGR). Lastly, a further increase in temperature or decrease in strain rate results in the transition to *Regime 3*. *Regime 3*, or general recrystallization, describes the operation of both mechanisms at once.

Using a Griggs apparatus to deform Black Hills quartzite, Stipp and Tullis (2003) observed recrystallized grain sizes between 3.2 ± 0.7 and 46 ± 15 μm with microstructures corresponding to *Regime 2* and *3*. Combining that data with unpublished data from Bishop (1996; presented in Post and Tullis, 1999, as cited in Stipp and Tullis, 2003*)* (Figure 12), it was determined that dynamic recrystallization under *Regime 1* results in a different slope (piezometric exponent, m) than *Regimes 2* and *3*. *Regimes 2* and *3* fit the same relation and had no change in slope at the *Regime 2/3* transition. Stipp and Tullis (2003) hypothesized this variance could be due to different dominant recrystallization mechanisms.
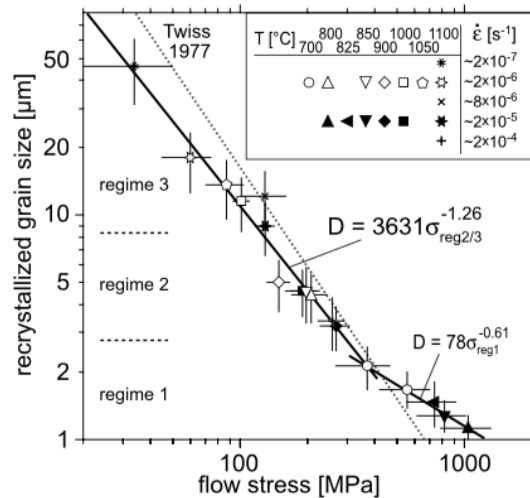
Figure 2-2. Recrystallized grain size piezometer for quartz (Stipp and Tullis, 2003).

In Stipp and Tullis (2003) recrystallized grain size was expressed by two equations:

$$\text{Regime 1} \qquad D = 10^{1.89\pm0.11} \cdot \sigma^{-0.61\pm0.04} \qquad (2)$$

$$\text{Regimes 2 and 3} \qquad D = 10^{3.56\pm0.27} \cdot \sigma^{-1.26\pm0.13} \qquad (3)$$

where D is the root mean square (RMS) average grain size in μm and σ is flow stress in MPa.

This piezometer was deemed effective for the grain sizes recorded in Stipp and Tullis (2003) (~3 to 45 μm). Stipp and Tullis (2003) did not identify any dependence of recrystallized grain size on temperature or the α-β quartz transition. Stipp et al. (2006) added that there is no independent effect of water content or strain rate on recrystallized grain size. Therefore, it was concluded that recrystallized grain size was dependent on flow stress (σ) and the dominant recrystallization mechanism.

More recently, Stipp and Tullis (2010) revisited the 2003 quartz grain size piezometer with natural samples. The natural data set granted the ability to examine a much larger range of grain size distribution than in experimental samples. The recrystallized grain size distribution of natural quartz samples in Stipp and Tullis (2010) ranged from ~2.5 μm to 2.8 mm. It was found that distinct grain size distribution peaks separated by minima correlated to the dominant operation of one of three main recrystallization mechanisms, bulging recrystallization (BLG), subgrain rotation recrystallization (SGR), and grain boundary migration (GBM). When these results were compared to the 2003 piezometer (Stipp and Tullis), it was determined that all three regimes of Hirth and Tullis (1992) are mostly contained within the BLG grain size fraction of Stipp and Tullis (2010). Therefore, the earlier piezometer can only be reliably applied to grain size distributions resulting from BLG recrystallization. Stipp and Tullis (2010) found that the piezometer could apply reasonably well to SGR but resulted in significant underestimates of flow stress for GBM (D > 120 μm). This substantiates the rationale that distinct piezometers are

needed for each recrystallization mechanism as well as the necessity for additional research of natural samples at larger grain sizes. Cross et al. (2015) also presented a recrystallized grain size distribution of quartz from a natural mylonite (10 to 100 μm) that matched within error to Stipp and Tullis (2003). Due to sample features reviewed in Chapter 4 and 5 Stipp and Tullis (2003)'s *Regime 2/3* quartz piezometer which will be used with consideration of its limitations.

2.2.3 Austin and Evans (2007)

Austin and Evans (2007) introduced the paleowattmeter as a scaling relation between dynamically recrystallized grain size and stress at a steady state. Austin and Evan's model postulates that recrystallized grain size is a factor of both strain rate and stress, while most paleopiezometry only considers the latter. The paleowattmeter suggests that recrystallized grain size is dependent on the rate of mechanical work done during dislocation creep. Dislocation creep is a deformation mechanism in which dislocation glide is balanced by recovery mechanisms. Whereas dislocation glide increases the density of free dislocation and the energy within the system, recovery mechanisms (i.e. subgrain formation and recrystallization) lower the internal free energy of the system so that a steady-state creep can be sustained. The paleowattmeter is contingent on the assumption that the internal energy increase due to dislocation glide is only partly dissipated by recovery and the remaining internal energy increase is related to the recrystallized grain size. Work done by diffusion creep is wholly dissipated. The steady state grain size occurs when there is a balance between the rates of dynamic grain size reduction and normal grain growth. Austin and Evan's model includes a dependence of recrystallized grain size on temperature, consistent with multiple paleopiezometers. However, the paleowattmeter may underestimate differential stress at low temperatures and when extrapolated to natural conditions (Kidder et al., 2012; Kidder et al., 2016). Additionally, the

paleowattmeter predicts average grain size at a steady-state (100% recrystallization) (Austin and

Evans, 2009) and may therefore not be applicable to partially recrystallized samples (Kidder et

al., 2016). The paleowattmeter is not dependent on the operating recrystallization mechanism

(Austin and Evans, 2009).

Recrystallized grain size as expressed in Austin and Evans (2007) is as follows:

$$d_s^{1+p} = \frac{K_g \exp\left(\frac{-Q_g}{RT}\right) p^{-1} c \gamma}{\lambda \sigma \dot{\varepsilon}_{disl}} \tag{4}$$

where: d_s is steady state grain size in μm, K_g is the grain growth rate parameter in $\mu m^{-p} s^{-1}$, Q_g is

the activation energy of grain growth in kJ/mol, R is the universal gas constant in $J \cdot K^{-1} \cdot mol^{-1}$, T

is absolute temperature in K, p is the exponent in the normal grain growth law (non-

dimensional), c is a geometric constant (non-dimensional), γ is the average specific grain

boundary energy in J/mol^2, λ is the fraction of work done by dislocation creep that is not

dissipated (non-dimensional), σ is differential stress in MPa and $\dot{\varepsilon}_{disl}$ is the strain rate of

dislocation creep in s^{-1}.

Experimentally determined flow laws describe the rheological behaviour of a mineral and

must be used to relate the dislocation creep strain rate ($\dot{\varepsilon}_{disl}$) to the differential stress. There are a

few different dislocation creep flow laws for quartzite (e.g. Gleason and Tullis, 1995; Luan and

Paterson, 1992; Hirth et al., 2001; Rutter and Brodie, 2004). Austin and Evans (2007) originally

employed the quartz flow law of Hirth et al. (2001). The variation in quartz flow laws is mainly a

result of differing Q values (activation energy); i.e. 223 ± 56 kJ/mol (Gleason and Tullis, 1995),

152 ± 71 kJ/mol (Luan and Paterson, 1992), 135 ± 15 kJ/mol (Hirth et al., 2001), and 242 ± 24

kJ/mol (Rutter and Brodie, 2004). Lu and Jiang (2019) introduced a new quartz flow that

reconciles the difference between Q values among previous laws. In place of the activation

energy of dislocation creep, Lu and Jiang (2019) instead use the activation enthalpy. Activation

enthalpy for dislocation creep is the activation energy of the system (Q) plus the product of the activation volume (V) and pressure (P). It was previously believed that the pressure effect was not significant in flow law equations pertaining to the deformation in the crust due to the small range of pressure at which deformation occurs (i.e. activation enthalpy $\cong$ activation energy). However, Lu and Jiang (2019) found that the magnitude of difference in confining pressure in previous experiments can account for over 10% variation in Q and therefore considering the PV term is critical. The use of the activation enthalpy, as well as the inclusion of water fugacity in the flow law, accounts for the influence of pressure on strain rate.

My results will use the updated flow law of Lu and Jiang (2019):

$$\dot{\varepsilon} = (6.0 \pm 5.0)x10^{-15} f_w^{2.7} \exp\left(\frac{Q+PV}{RT}\right)\sigma^4 \qquad (5)$$

where: f_w is water fugacity in MPa, Q is activation energy in J/mol (Q = 132±5 kJ/mol as determined by Lu and Jiang (2019) as an average of existing experimental data), P is pressure in MPa, V is the activation volume for wet quartzite in cm³/mol (35.3 cm³/mol), σ is differential stress in MPa, R is the universal gas constant in J·K⁻¹·mol⁻¹ and T is temperature in K.

2.2.4 Shimizu (2012)

Shimizu (1998) introduced a new piezometry model based on the nucleation and growth model of dynamic recrystallization, the piezometer relates the SGR nucleation rate and grain growth by GBM as functions of stress and temperature and therefore applies to *Regime 3* recrystallization. In subsequent work (Shimizu, 2008, 2012) this piezometer has been calibrated and revised, as outlined below.

Shimizu's major criticisms of previous piezometers included consideration of the change in activation energy at the α-β quartz transition, methods of grain size data collection and the

effects of surface energy on grain growth. Firstly, Shimizu (2008) stipulated that different piezometers are required for α and β quartz due to the change in activation energy of oxygen diffusion and grain boundary diffusion at the α-β transition as they are both temperature dependent processes. Shimizu (2008) uses the coefficient of volume diffusion (D_v) and the diffusion coefficient at the grain boundary (D_{gb}) from Farver and Yund (1991a) and Giletti and Yund (1984) to determine Q_v and Q_{gb} of β quartz. For α quartz, Shimizu (2008) uses the D_v of Farver and Yund (1991b), D_{gb} is assumed to be continuous at the transition temperature, and the ratio of Q_v to Q_{gb} in α quartz is assumed to be equal to that of β quartz. The separation of this piezometer into two distinct relations results in a change in the temperature dependence of flow stress at the α-β transition. Shimizu (2008) identified that recrystallized grain size shows a low dependence on temperature at high temperatures (>800°C) and a higher dependence at lower temperatures. Secondly, Shimizu (2008) argues shortcomings in previous methods of grain size data collection. Shimizu (2008) notes the fact that grain size distribution is not considered in earlier piezometers. Conventionally, the mean recrystallized grain size is used for quartz piezometers. However, in the case of steady-state recrystallized samples, grain size distribution is typically log-normal, meaning that the highest volume grain size may not align with the average grain size (i.e. Figure 2-3). Shimizu (2008) argues that in that case, the median recrystallized grain size would be more representative of the steady-state grain size of most samples. Considering this claim, the difference in the median and mean recrystallized grain size will be considered in the results.
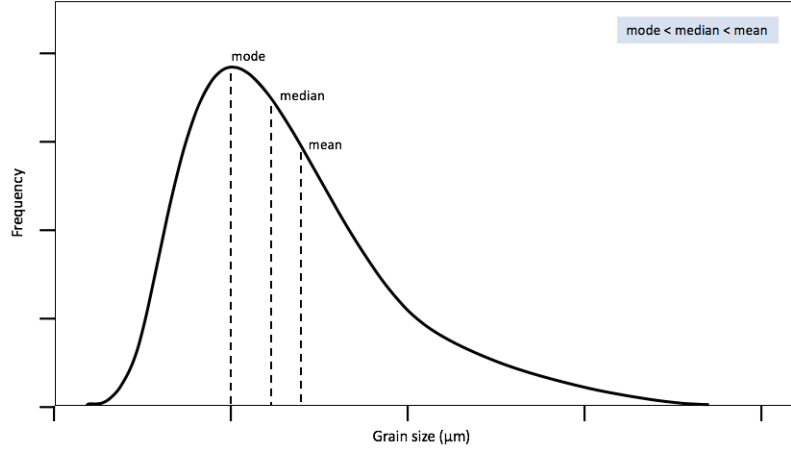
Figure 2-3. Theoretical comparison of mean, median and mode in a log-normal distribution.

Lastly, in Shimizu (2012) the influence of surface energy (grain boundary energy) was incorporated into the Shimizu model. Surface energy drives grain coarsening in static state by means of larger grains growing at the expense of smaller grains. Therefore, surface energy acts as a drag force in strain-energy-driven GBM. The influence of surface energy on grain growth rate is accounted for in a non-dimensional constant (*B*) in the calibration of Shimizu (2012)'s piezometer which has the general form:

$$\frac{d}{b} = K° \left(\frac{\sigma}{\mu}\right)^{-p} \exp\left(-\frac{\Delta Q}{mRT}\right) \tag{6}$$

where

$$K° = B\left(\frac{wD°_{gb}}{bD°_v}\right)^{1/m} \tag{7}$$

and

$$\Delta Q = Q_{gb} - Q_c \tag{8}$$

d is steady state grain size in µm, b is the length of the Burgers vector in m, B is a non-dimensional scaling factor, σ is differential stress in Pa, μ is shear modulus in Pa, p is the non-dimensional stress exponent of recrystallized grain size, w is grain boundary width in m, $D°_{gb}$ is a constant, $D°_v$ is a constant, m is a non-dimensional scaling parameter, Q_{gb} is the activation energy of grain boundary diffusion in J·mol^{-1}, Q_c is the activation energy of dislocation creep in

J·mol⁻¹, R is the universal gas constant in J·K⁻¹·mol⁻¹ and T is temperature in K. With these modifications, and the correction of a numerical error in Shimizu (2008), recrystallized grain size expressed in Shimizu (2012) became:

$$\alpha\text{-quartz} \qquad d = 9.98 \cdot 10^2 \cdot \sigma^{-1.25} \exp(\frac{12.4\ kJ/mol}{RT}) \qquad (9)$$

$$\beta\text{-quartz} \qquad d = 1.82 \cdot 10^3 \cdot \sigma^{-1.25} \exp(\frac{7.25\frac{kJ}{mol}}{RT}) \qquad (10)$$

where d is the steady-state grain size in μm, σ is differential stress in MPa, R is the universal gas constant in J·K⁻¹·mol⁻¹ and T is temperature in K.

The Shimizu piezometer is deemed suitable for high-temperature samples recrystallized by SGR and GBM. However, this relation is not suitable to rocks deformed at low-temperature conditions (< 400°C), as stress states would be significantly underestimated (Shimizu, 2012).

Chapter 3

3 Materials and Methods

Figure 3-1 indicates the sample locations chosen for this thesis. The rationale was to choose samples of varying stress state and composition to evaluate the ability to use U-Pb zircon strain chronometry to date Grenvillian deformation. Foliation in the area was primarily identified as NE-SW trending transposition foliation (S_{T2}). Samples were chosen from these D_3 structures. The southwestern two-thirds of the complex are obstructed by swamp/marsh area and private properties, the northeastern most section is poorly exposed. Therefore, field work was limited to the northeastern most area of the complex along HWY 537 (~500 m west of highway).

Figure 3-1. Left: Map of sample locations. Right: Stereonet representing field measurements of S_{T2} foliation and D_3 fold hinges.
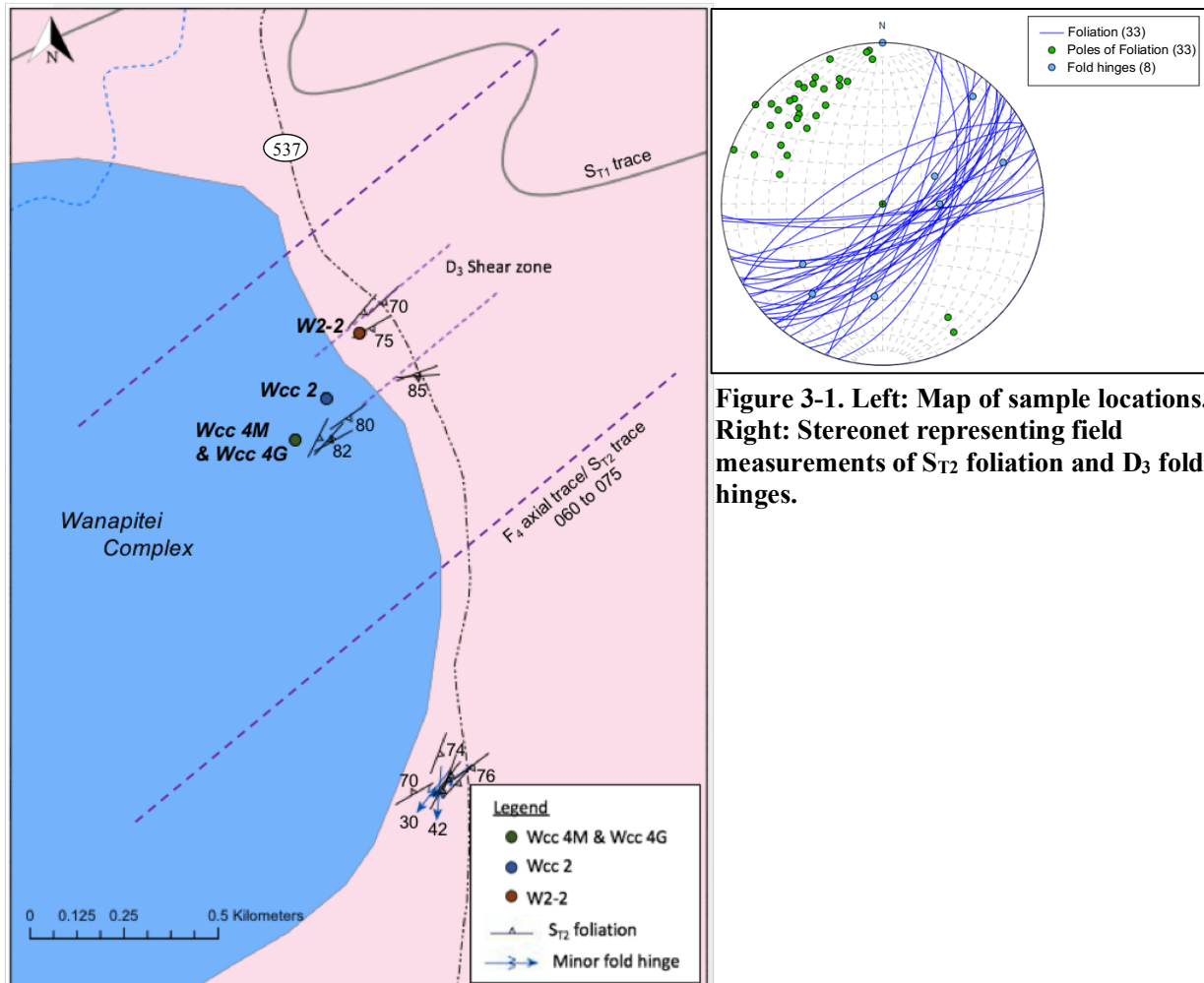
Wcc 4M, Wcc 4G and Wcc 2 are samples collected by Li (2012). W1-1/W1-2, W2-1/W2-2 and W3 were collected for this thesis, sample descriptions are listed in Table 1. The samples were cut perpendicular to D_3 foliations and prepared as 30-micron thin sections, with the exception of Wcc 2, which was viewed under scanning electron microscope as a rock slab, thin sections for Wcc 2 were later made for optical investigation. Preliminary imaging was done with a backscattered electron (BSE) map of each sample. The BSE samples were carbon coated for electrical conductivity. Element composition mapping was also completed for each sample.

Table 1. Sample descriptions.

Sample	Collection	Rock Type	Mineralogy	Foliation (strike/dip)	Lineation (plunge/trend)	Cut
Wcc 4M	Li (2012)	Wanapitei metagabbro (1747 +6/-5 Ma)	Hbl, plag, bt, ilm, gt	not oriented	N/A	perp to foliation, defined by biotite
Wcc 4G	Li (2012)	Granitic dyke (age unknown)	Qtz, albite, ilm, trace biotite	not oriented	N/A	perp to foliation, defined by quartz ribbons
WCC-2	Li (2012)	Wanapitei metagabbro (1747 +6/-5 Ma)	Hbl, plag, trace bt, ilm and gt	not oriented	N/A	perp to foliation, defined by coarse grained quartz layers parallel to lineation
W1-1/W1-2	Petkau (2017)	Biotite garnet gniess (age unknown)	Qtz, bt, grt, trace ky	085/79	260/32 stretching lineation	perp to foliation, weakly defined by bt 1-1 parallel to lineation 1-2 perp to lineation
W2-1/W2-2	Petkau (2017)	Biotite garnet gniess (age unknown)	Qtz, bt, grt, trace ky	085/79	Not measured in field	perp to foliation, weakly defined by bt 2-1 parallel to lineation 2-2 perp to lineation
W3	Petkau (2017)	Biotite garnet gniess (age unknown)	Qtz, bt, grt, trace ky	N/A	Not measured in field	parallel to lineation

*Petkau (2017) refers to field work associated with this study

3.2 Zircon selection and analysis

The largest zircon, baddeleyite and monazite grains were chosen for detailed analysis with BSE and Electron Backscatter Diffraction (EBSD) as these were the best targets for follow-up U-Pb dating. The BSE imaging displays the variation of average atomic number in a phase and internal elemental variations by grayscale, which can correlate to different growth phases or zones of secondary recrystallization or alteration. BSE images were taken using a Hitachi SU6600 FEG-

SEM (Field Emission Gun Scanning Electron Microscope) with an emission current of 3.6 microA and an accelerating voltage of 15 kV. Working distance was 9800 μm, at 80x magnification.

EBSD was also used to map internal variations in lattice orientation and crystallinity (order). The EBSD method entails using a series of computations to determine the phase and orientation of samples at a set spatial resolution (step size ~ 0.1-0.15 μm). Interaction of the incident beam with the sample results in an output of a pattern of diffracted electrons (EBSP) which consists of Kikuchi bands at different angles and intensities that correspond to lattice planes orientation, spacing and diffraction efficiency (intensity) comparable to an X-ray pattern (Reddy et al., 2007). The EBSP is then analyzed by EBSD post-processing software (Oxford Instruments HKL Channel 5) that detects and analyses these properties of Kikuchi bands using the Hough transform and compares the output to a reference library, set up by the user, of model EBSP characteristics. This allows the sample to be indexed by phase and orientation with an angular resolution of ~0.5° following the methods in Moser et al. (2011). The "Tango" program allows the user to make measurements and maps based on information indexed during EBSD. "Tango" was used to map the internal misorientation of individual grains within the samples. A specific point within the target is chosen as a reference point, following which the relative misorientation throughout the grain is presented using a colour gradient. The misorientation profile shows the relative lattice misorientation of a line drawn through the crystal (noise ~0.5°). By examining the internal orientation within a grain, lattice distortion, if present, can be identified. The "Mambo" program can also be used to observe crystallographic orientation and misorientation. The "Mambo" program reads the EBSP data to produce pole figures of plane

normals to display relative crystallographic orientation. Data were plotted in "Mambo" using lower hemisphere, equal area projections.

Target zircon grains are those of igneous origin with significant lattice distortion (>0.3°/μm (Piazolo et al., 2012); ~3-40° cumulative misorientation per grain (Kovaleva et al., 2014)).

3.3 Grain size analysis

Samples were then investigated under a Nikon Eclipse LV100POL polarizing microscope. Using the Nikon NIS Elements Imaging Software, quartz grain size measurements were made on samples Wcc 4G and W2-2. The auto-detect tool is an automatic drawing tool that identifies grains based on a manually placed probe; manual adjustment is then used to confirm the grain boundaries (e.g. Figure 3-2). The estimated random error of measurement is ± 2.97 μm (based on reproducibility n=50, σ=2.97 μm).
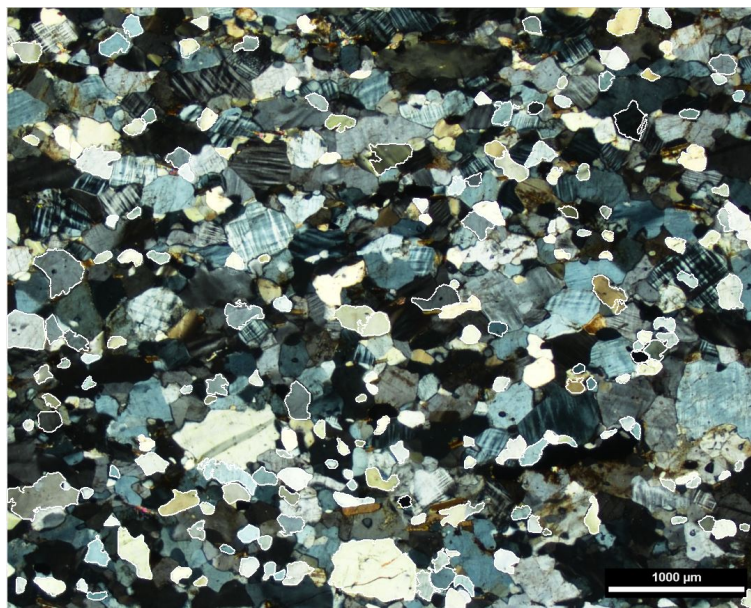
Figure 3-2. Quartz grains measured in Wcc 4G using NIS Element "auto-detect" function. White polylines indicate auto-detected grain boundaries used for measurements.

The .xls reports generated by NIS Elements measure features including area, grain size, minimum feret length, and maximum feret length. Grain size was measured as the equivalent diameter (Eqdia) of a circle with the same area (Figure 3-3). Elongation was calculated as the ratio between maximum and minimum feret length.

$$Eqdia = sqrt(4*Area/ \pi)$$
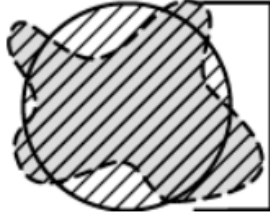
Figure 3-3. Eqdia calculation (Nikon, NIS Elements Advanced Research: User's Manual Ver. 4.00).

Chapter 4

4 Results

The results of microstructural analyses will be presented in two sections; the first on zircon followed by a section on quartz grain size analysis and piezometry. The zircon section will feature grain distributions in oriented samples followed by in situ microstructural investigations using backscattered electron imaging (BSE) and electron backscatter diffraction (EBSD) in each of the four samples. The second section on quartz piezometry will present the grain size distribution of recrystallized quartz in the two quartz-rich samples. Through optical microscopy, texture development and quartz grain size distribution were used to approximate the differential stresses experienced by the mafic samples. Four samples were investigated; two samples of the Wanapitei metagabbro (Ca. 1747 +6/-5 Ma), one of a granitic dyke intruding the complex (age unknown), and one of the supracrustal country rock (age unknown). Zircon grains were chosen based on size and position within localized strain zones and differing host matrix to obtain an accurate representation of zircon within each sample.

Refer to Appendix A for all imaging and EBSD maps. Feature lists for each sample including zircon, monazite and baddeleyite grain statistics can be found in Appendix B.

4.1 Microstructural Investigation

4.1.1 Wcc-4m – Garnet Amphibolite

Sample mineralogy, fabrics and zircon distribution

Sample Wcc 4M is from the metagabbroic Wanapitei Complex. The complex is a hornblende metagabbro, and its main mineral assemblage is hornblende, plagioclase, biotite and almandine

garnet (Figure 4-1). The sample contains minor quartz and traces of iron sulphides and titanite. Extensive metamorphism has led to the complete replacement of pyroxene by hornblende. The thin section is cut perpendicular to the foliation which is defined by amphibole and biotite. Poikiloblastic garnet is anhedral and deeply embayed with inclusions of matrix minerals including hornblende, plagioclase, biotite and sulphides. Garnet is fractured subperpendicular to foliation; fractures are infilled by chlorite. Hornblende and biotite bow around garnet and garnet fragments follow foliation. These features indicate that garnet is syn-deformational. The foliation in this sample is parallel to the Grenville Front and lacks overprinting from F_4, it is therefore identified as S_{T2} foliation, a D_3 fabric (Li, 2012). The MicroGIS map of the sample (Figure 4-2) shows zircon grains greater than 10 μm in size. Zircon in this sample is homogeneously distributed and ranges in size up to 58.63 μm. Also mapped are two monazite and two baddeleyite grains. Figure 4-3 displays the zircons that were investigated in detail with BSE and EBSD imaging.
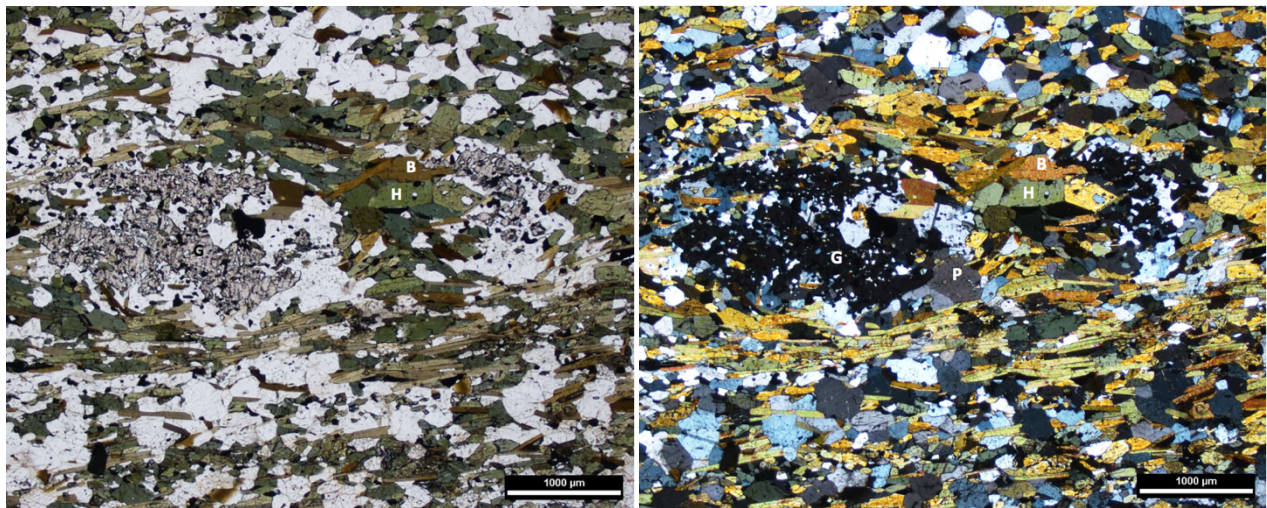
Figure 4-1. Photomicrographs of sample Wcc 4M in plane polarized light (left) and cross polarized light (right). B: biotite, H: hornblende, P: plagioclase, G: garnet. Scale bar = 1000 μm.
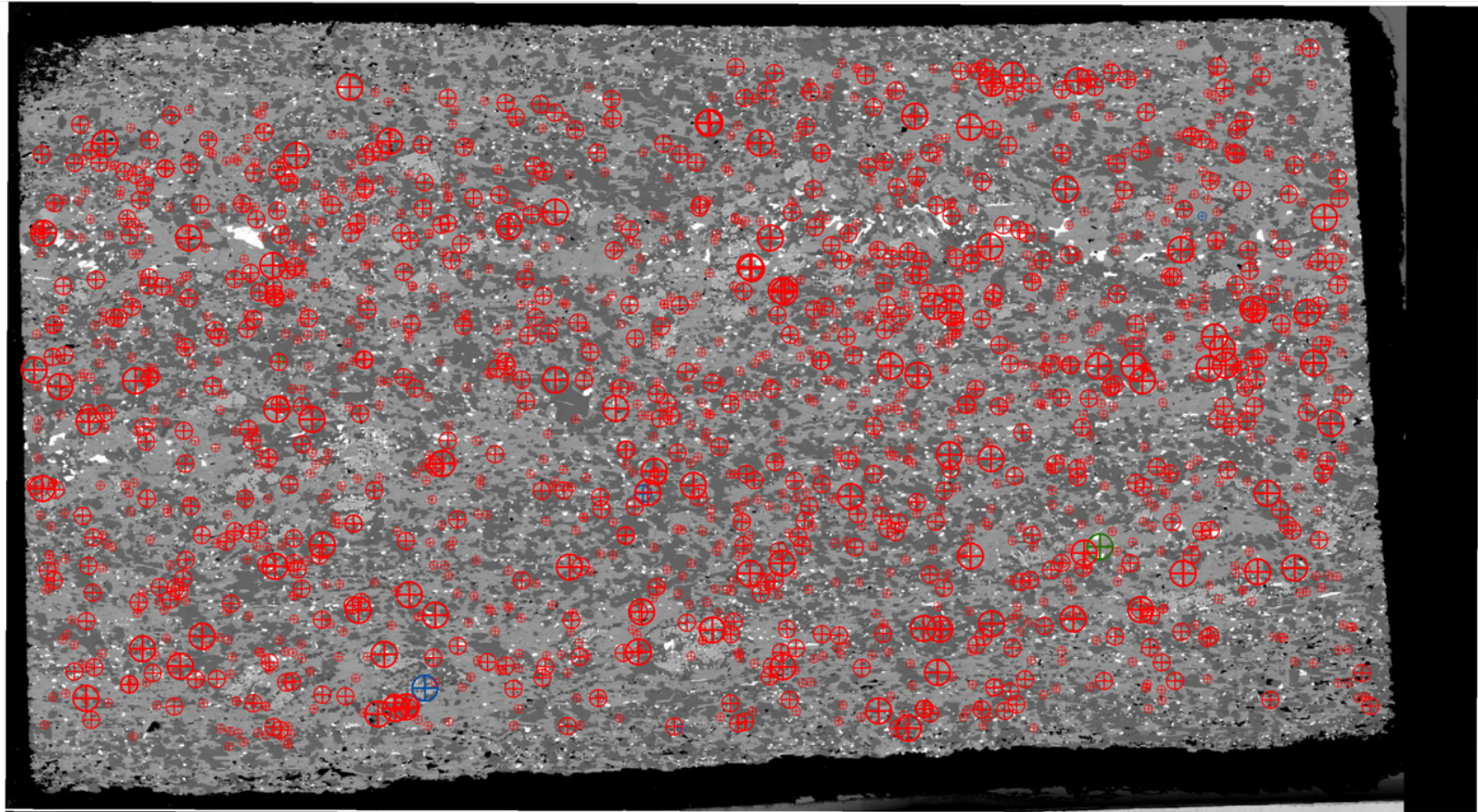
Legend (Length μm)

Zircon
- ⊕ 10.02 - 15.67
- ⊕ 15.68 - 25.43
- ⊕ 25.44 - 58.63

Baddeleyite
- ⊕ 4.199 - 5.009
- ⊕ 5.010 - 6.790
- ⊕ 6.791 - 9.638

Monazite
- ⊕ 4.199
- ⊕ 4.200 - 5.994

0   2.75   5.5   11 Millimeters

Figure 4-2. MicroGIS map of accessory minerals in sample Wcc 4M. Zircons >10 um.
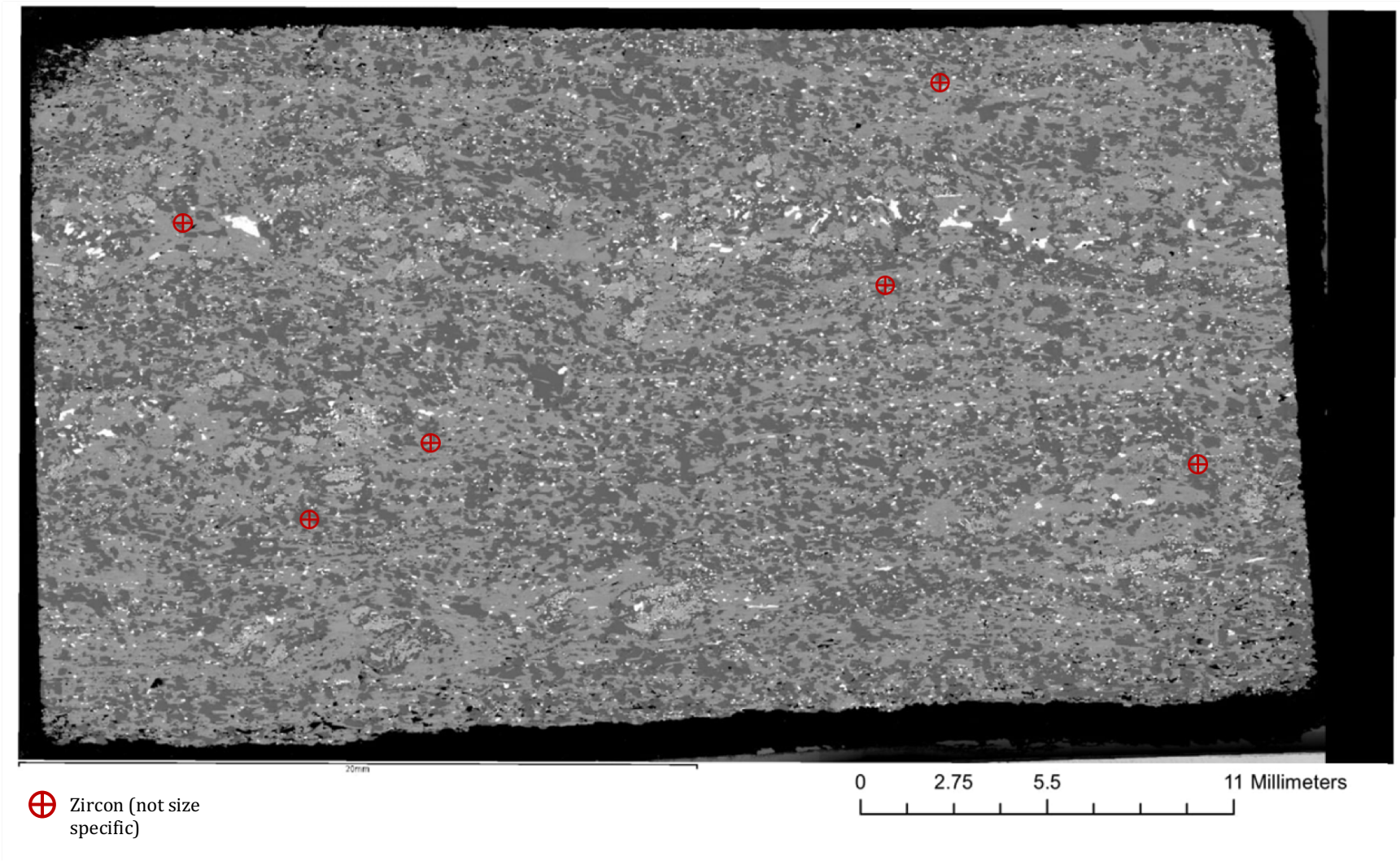
Figure 4-3. MicroGIS map of zircons imaged with BSE and EBSD in sample Wcc 4M.

In sample Wcc 4M, 3794 zircon grains were identified and, of these, 1668 were greater than 10 microns in size. A total of 12 were imaged with BSE imaging. Zircon grains in sample Wcc 4M exhibit three main morphologies. First, sector zoning is present in euhedral to subhedral zircons of both igneous and metamorphic origin (Figure 4-4: A, B). Metamorphic zircons are often distinguished from igneous by their irregular shape, sub-rounded edges and evidence of resorption while igneous zircon shows euhedral crystal development (Corfu et al., 2003; Hoskin and Schaltegger, 2003). Second, relict igneous cores are mantled by metamorphic rims (Figure 4-4: C, D). Cores exhibit oscillatory zoning and are resorbed and overgrown by homogenous metamorphic rims. During cooling, radiation damage causes expansion of the high-U (BSE bright) core (Holland and Gottfried, 1955) resulting in radially fractured rims (e.g. Chakoumakos et al., 1987). Lastly, complex metamict cores are overgrown by metamorphic rims (Figure 4-4: E, F). Cores show traces of concentric zoning, but zircons are significantly metamictized and fractured.
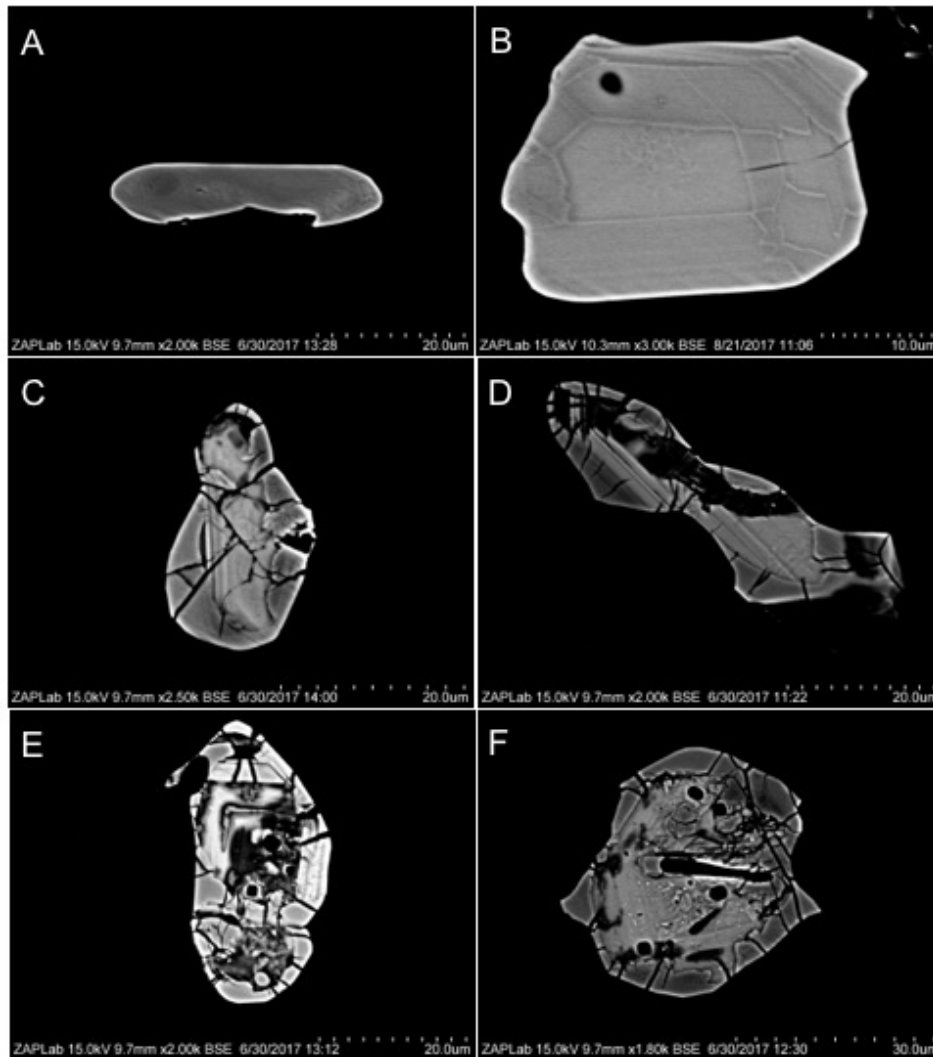
Figure 4-4. (A) Euhedral {100} igneous zircon with sector zoning. (B) Subhedral equant metamorphic zircon with sector zoning. (C, D) Igneous core with metamorphic mantle. Mantle fractured by expansion of high-U core. (E, F) Complex metamict core exhibiting traces of igneous zoning, metamorphic rims are intensely fractured.

Grain 16910 (Figure 4-5) is a sector-zoned metamorphic zircon. EBSD maps show there is no

significant distortion (< 3°), as displayed by the colour gradient (Figure 4-5: C) and

misorientation profile (Figure 4-5: D). Pole figures (Figure 4-5: E) display the orientation of the

grain and do not indicate deformation. Grain 16910 is representative of zircon grains in this

samples; three additional grains show misorientation < 3°, attributable in all cases to

displacement on open fractures.

E {100} Y1 Fx=0.348 {010} Fx=0.348 {001} Fx=0.304 Pole Figures
              Fy=0.362   Fy=0.362   Fy=0.275
              Fz=0.290   Fz=0.290   Fz=0.421 [2017-10-20_WCC-4M_
                                                        Zircon (4/mmm)
                                                        Complete data set
                                                        23481 data points
                                                        Equal Area projection
                                                        Lower hemispheres

X1
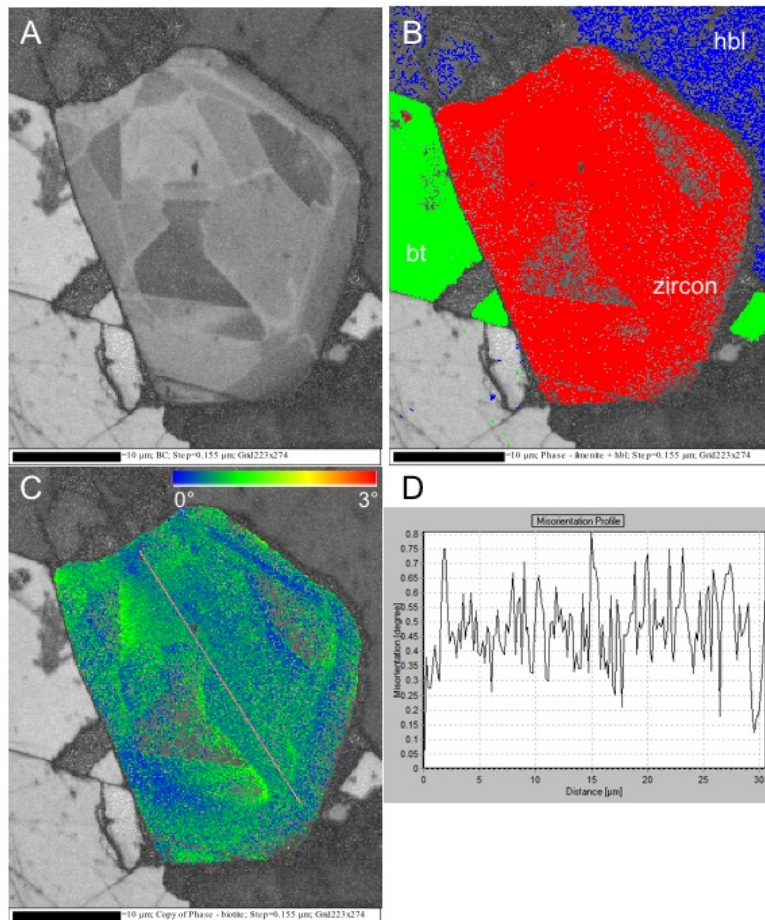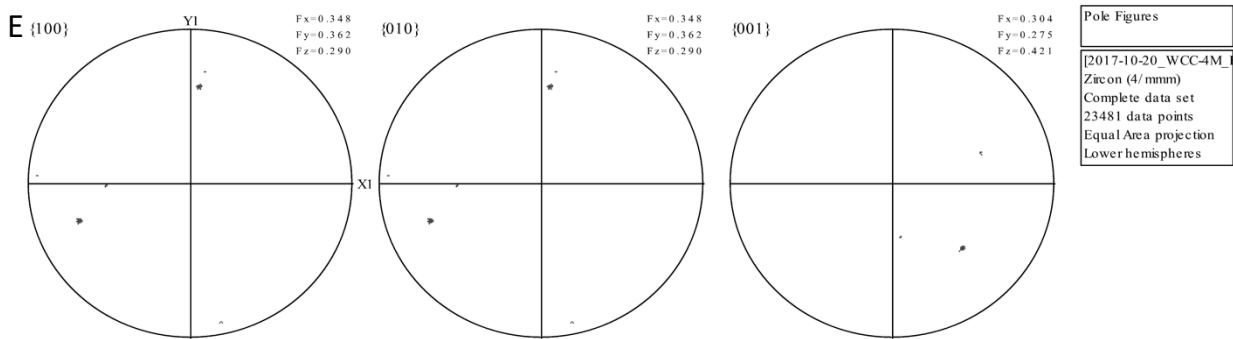
Figure 4-5. Grain 16910, metamorphic zircon. A: Band contrast image with fir-tree zoning. B: EBSD map colour coded by phase. C: EBSD map colour coded by misorientation (misorientation < 3°). D: Misorientation profile along line shown in C. E: Pole figure plot of grain orientation.

One baddeleyite grain (Grain 24937) was also imaged using EBSD (Figure 4-6). The baddeleyite shows no significant distortion (Figure 4-6: C), gaps in the misorientation profile (Figure 4-6: D) correlate with brittle fractures (Figure 4-6: A). Pole figures (Figure 4-6: E) display the orientation of the grain and do not indicate deformation.
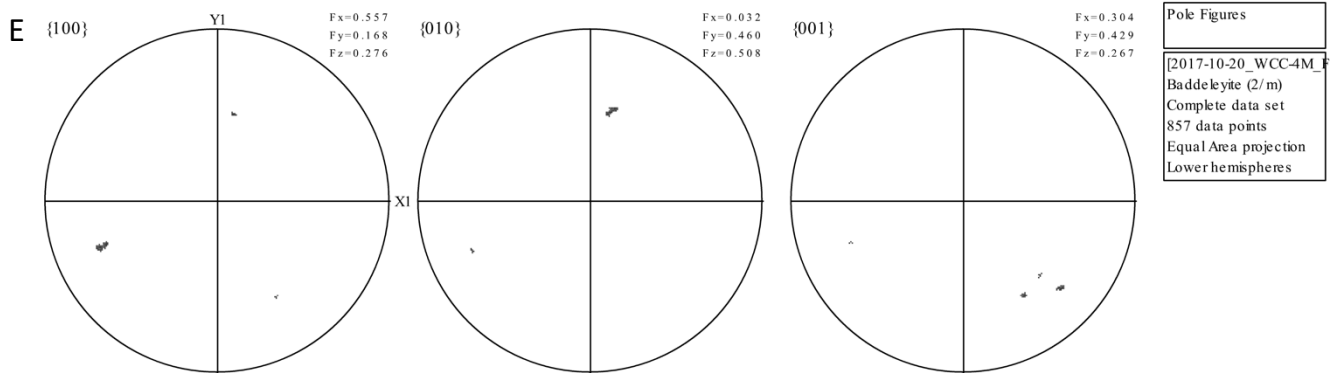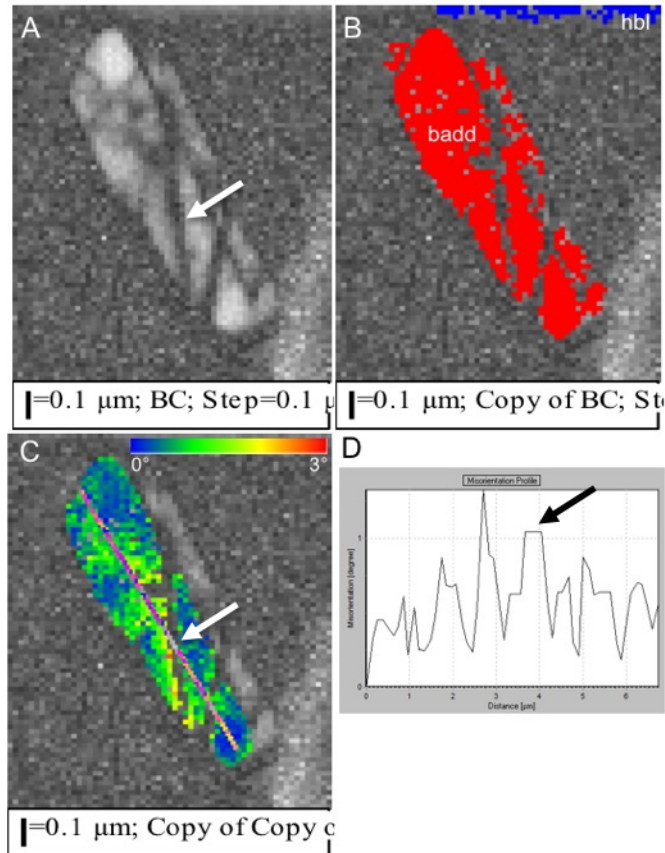
Figure 4-6. Grain 24937, baddeleyite. A: CL image; brittle fractures identified by arrows. B: EBSD map colour coded by phase. C: EBSD map colour coded by misorientation (misorientation < 3°). D: Misorientation profile along line shown in C, arrows correspond to fractures. E: Pole figure plot of grain orientation.

4.1.2 Wcc-2 – Garnet-Biotite Amphibolite

Sample mineralogy, fabrics and zircon distribution

Wcc 2 is the second sample from the Wanapitei Complex, containing a mineral assemblage of hornblende, plagioclase and quartz with trace amounts of biotite, garnet and ilmenite (Figure 4-7). The sample was prepared as a slab for the SEM as well as a thin section for optical microscopy. The section and slab studied were cut perpendicular to D_3 foliation, defined by amphibole and plagioclase, and parallel to lineation. Garnet is anhedral and poikiloblastic with inclusions of mainly plagioclase. Intragranular fractures run subperpendicular to foliation. This sample exhibits localized parallel banding that represents compositional and grain size differences (Figure 4-8). Bands of larger plagioclase grains (avg. eqdia = 270 μm) are adjacent to bands composed of hornblende, biotite and smaller plagioclase (avg. eqdia =150 μm). Plagioclase is recrystallized, exhibiting triple junctions (e.g. Figure 4-8 in circle) and is intensively sericitized. Biotite is largely replaced by chlorite. A MicroGIS map of the sample (Figure 4-9) shows the distribution of zircons greater than 10 μm. The map was used to ensure zircon grains were investigated from the compositionally different areas to compare internal structures. The largest zircon in Wcc 2 is 47.77 μm, there is no correlation between zircon size and location within the localized zones. Two monazite grains were also identified in this sample. Figure 4-10 displays the zircons that were investigated in detail with BSE and EBSD imaging.
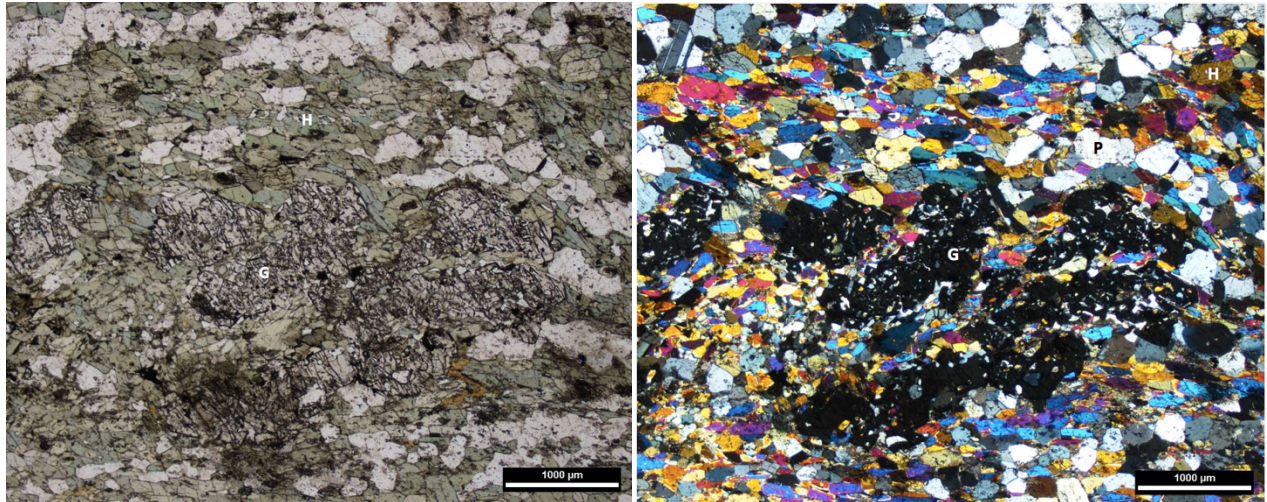
Figure 4-7. Photomicrographs of sample Wcc 2 in plane polarized light (left) and cross polarized light (right). B: biotite, H: hornblende, P: plagioclase, G: garnet. Scale bar = 1000 μm.
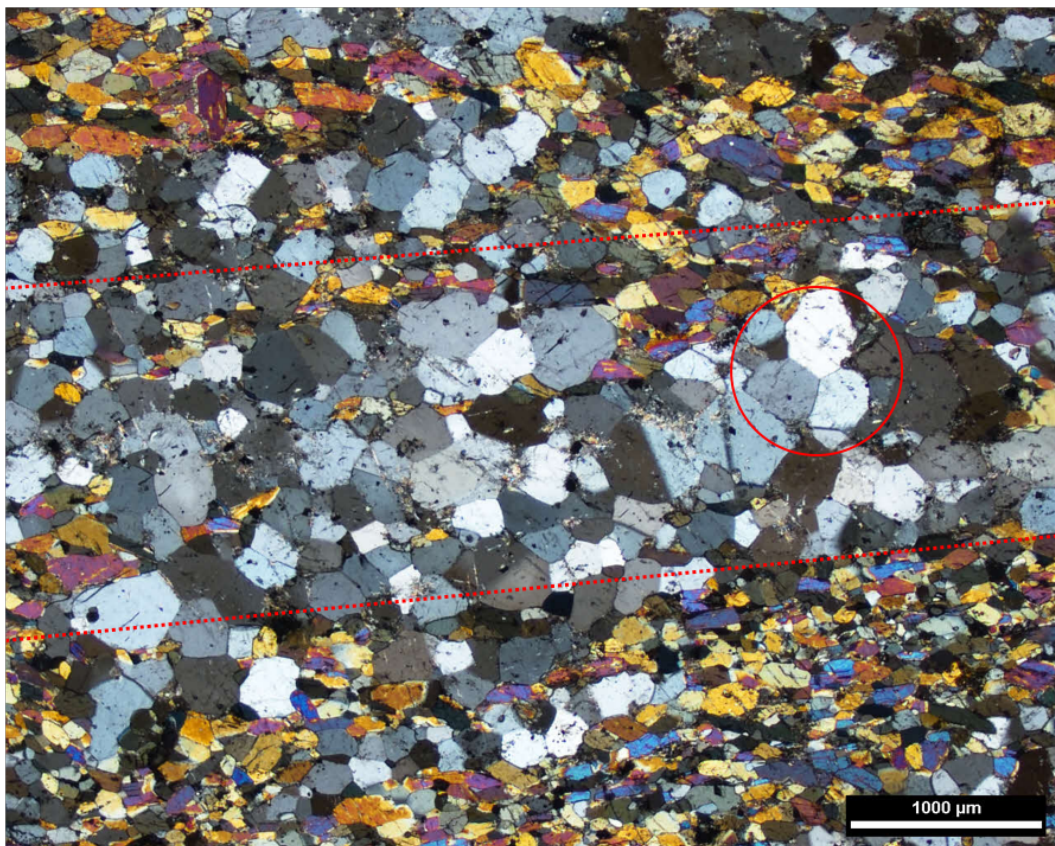

Figure 4-8. Compositionally contrasting bands in Wcc 2 marked by dotted line. In circle: plagioclase exhibiting triple junction grain boundary. Scale bar = 1000 μm.

Figure 4-9. MicroGIS map of accessory minerals in sample Wcc 2. Zircons >10 um.

Legend (length µm)

Zircon
- 10.19 - 15.38
- 15.39 - 25.85
- 25.86 - 47.77

Monazite
- 4.199
- 4.200 - 10.02

0 3.25 6.5   13 Millimeters
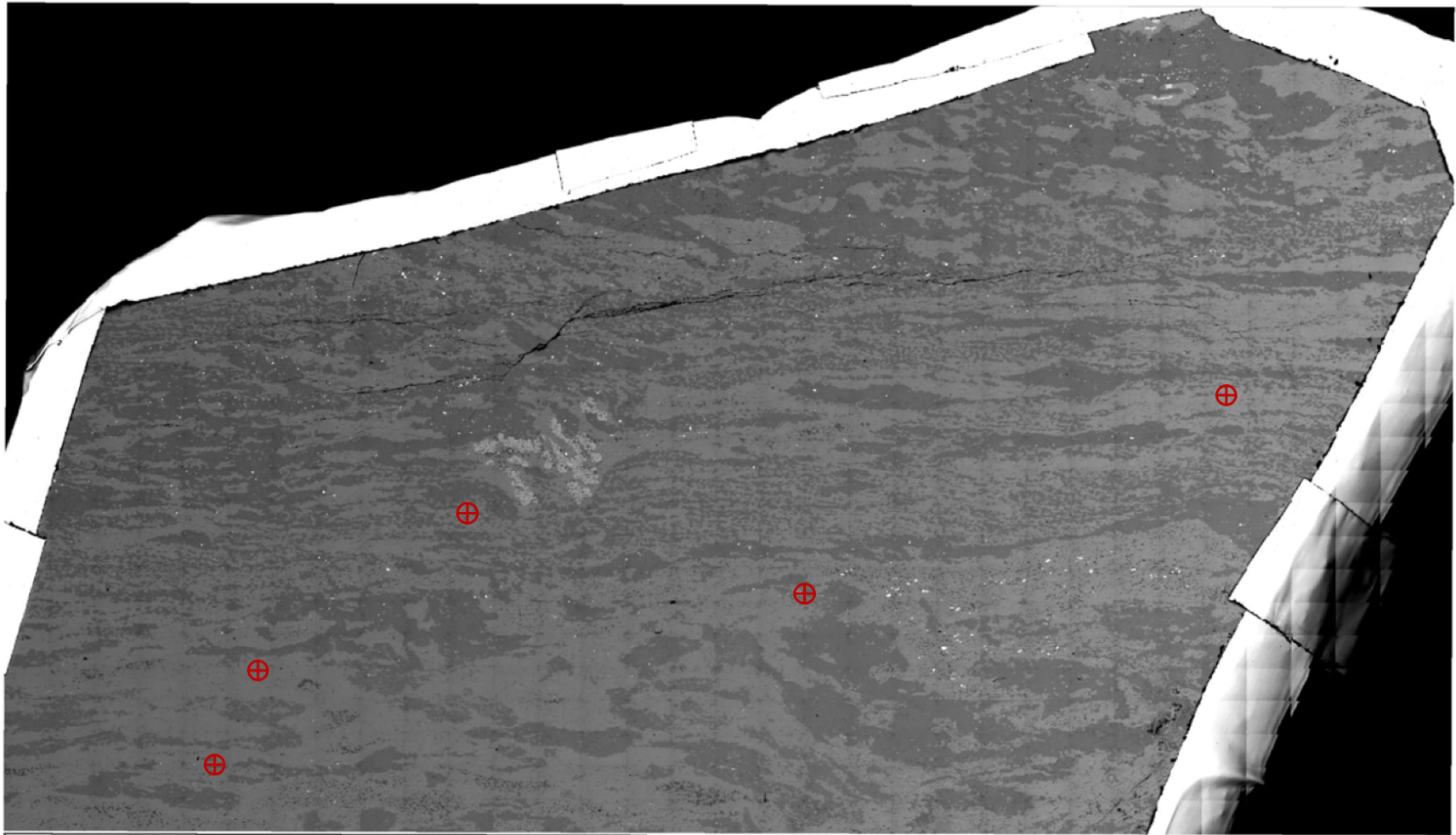
⊕ Zircon (not size specific)

0 3.25 6.5   13 Millimeters

Figure 4-10. MicroGIS map of zircons imaged with BSE and EBSD in sample Wcc 2.

A total of 105 zircon grains were identified in sample Wcc 2. Of these, 31 were greater than 10 microns in size, 13 were imaged using BSE imaging. There are two main morphologies of zircons in sample Wcc 2. First, anhedral sub-rounded grains are interpreted to be of metamorphic origin (Figure 4-11: A, B). In Figure 4-11: C, D these grains exhibit triple junction grain boundaries, typical of annealed minerals. Secondly, complex grains show igneous cores with relict oscillatory zoning resorbed and overgrown by metamorphic rims (Figure 4-11: E). Radial fractures extend through the metamorphic rim due to expansion of the core.
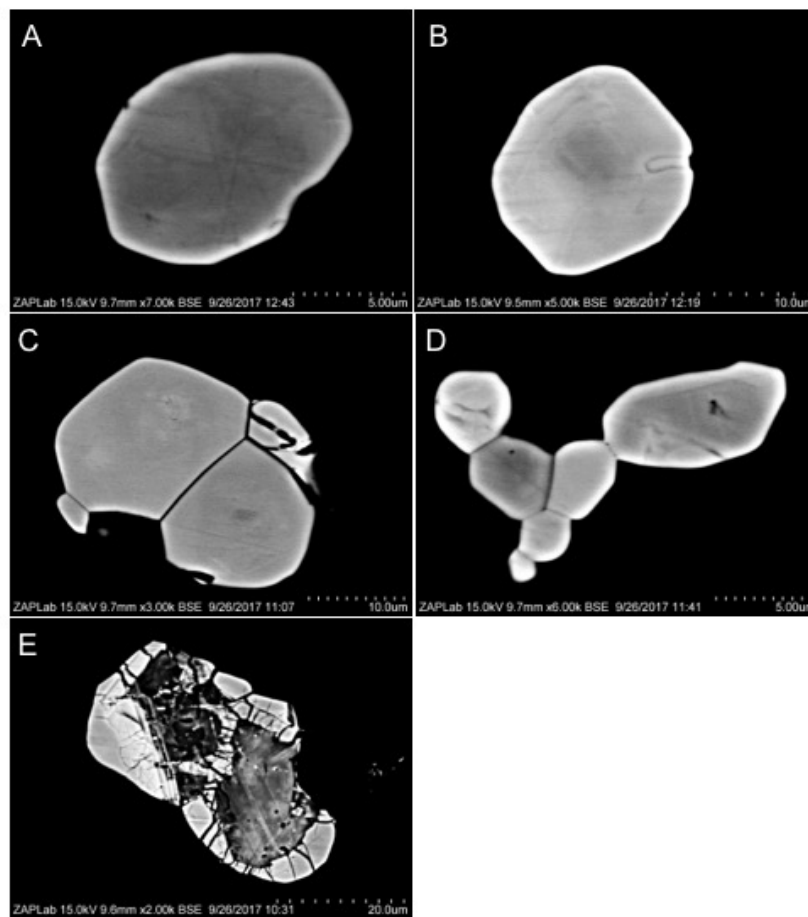
Figure 4-11. (A, B) Anhedral, sub-rounded metamorphic zircons. (C, D) Featureless metamorphic zircons exhibiting triple-grain junctions. (E) Igneous core mantled by fractured metamorphic zircon.

Grain 17451 (Figure 4-12) is an aggregate of four metamorphic zircons displaying features of annealing (Figure 4-12: A). EBSD maps show there is no significant distortion (< 2°), as displayed by the colour gradient of the two largest zircon grains (Figure 4-12: B, C) and misorientation profile corresponding to the upper left zircon (Figure 4-12: D). The two additional zircon grains in Figure 4-12 were examined with the same results.
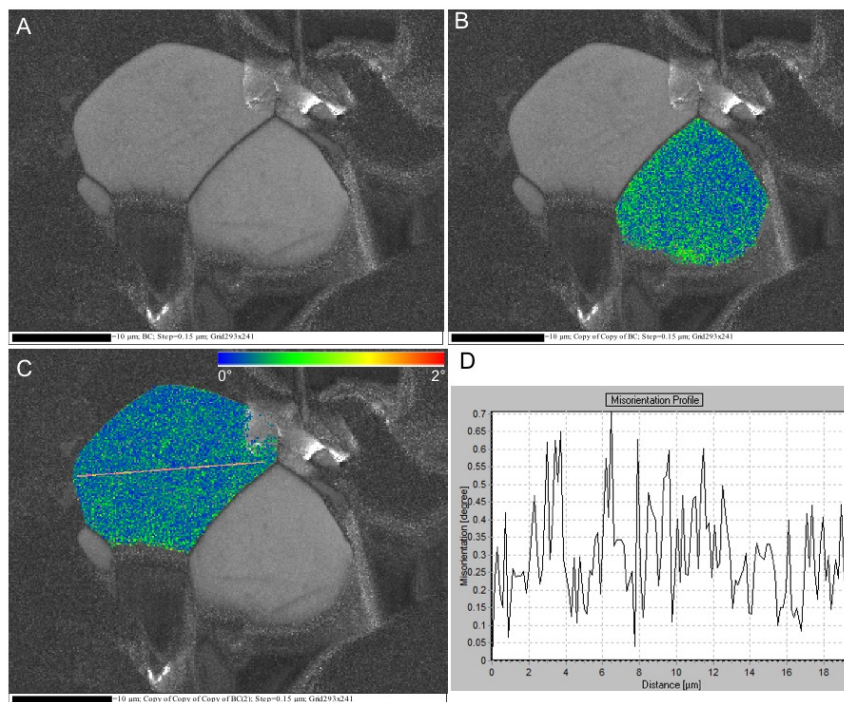
Figure 4-12. Grain 17451, aggregate of four metamorphic zircons. A: Band contrast image; triple junction at arrow. B: EBSD map colour coded by misorientation (misorientation < 2°). B: EBSD map colour coded by misorientation (misorientation < 2°). D: Misorientation profile along line shown in C.

Inverse pole figure (IPF) colouring is used to identify crystallographic orientation. Figure 4-13: A shows the IPF colouring of the target confirming that each grain's orientation is independent. Pole figures (Figure 4-13: B) display the orientation of each grain with IPF colouring and do not indicate deformation.
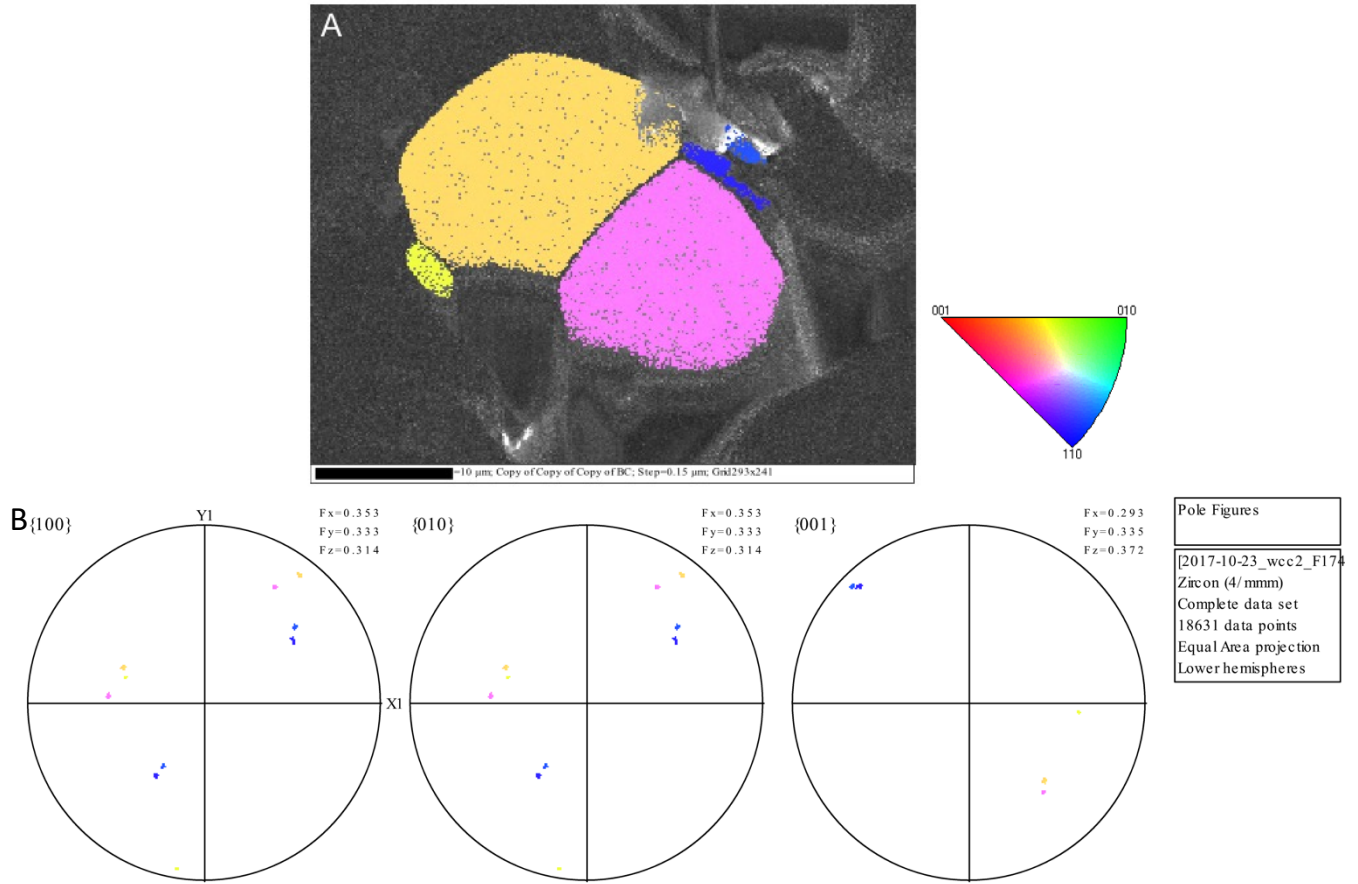
Figure 4-13. Grain 17451, metamorphic zircon. A: EBSD map with Inverse Pole Figure (IPF) colouring of zircon grains. B: Pole figure plot of grain orientation colour coded with IPF colouring.

Additional zircon grains mapped from sample Wcc 2 show comparable results. Internal misorientation is < 3° in the other five investigated zircon grains. Some minor distortion can be correlated to brittle fracture within the zircon grains and is not an indication of plastic deformation.

4.1.3 Wcc 4G – Deformed Granitic Dyke

Sample mineralogy, fabrics and zircon distribution

Wcc 4G is a granitic dyke that was observed crosscutting through the Wanapitei Complex (Li 2012). Its timing of crystallization is believed to be pre/syn-D_3. Wcc 4G has a matrix mineral assemblage of quartz, feldspar and sulphides with trace amounts of biotite (Figure 4-14). The granitic dyke appears to have undergone deformation-induced recrystallization and shows a weak foliation (parallel to the Y direction). The foliation is identified as a D_3 fabric (S_{T2}), orientation is unknown (Li, 2012). Quartz appears in the matrix as subgrains and recrystallized grains as well as significantly larger quartz ribbons. Quartz ribbons define the foliation. The origin of these ribbons is inconclusive. Models for the origin of quartz ribbons include (1) fracture filling by silica-rich fluids (Mackinnon et al., 1997) or (2) quartz coalescing by grain boundary migration and annealing (Hippertt et al., 2001). K-feldspar and plagioclase are present in the matrix as equant grains, with k-feldspar often displaying microcline twinning. Feldspar grains are slightly larger than the matrix quartz. The MicroGIS map of the sample (Figure 4-15) shows zircon grains greater than 10 μm in size. Zircon in this sample is homogeneously distributed and ranges in size up to 111.1 μm. 10 monazite grains were also mapped. Four zircon grains were investigated in detail with BSE imaging (Figure 4-16).
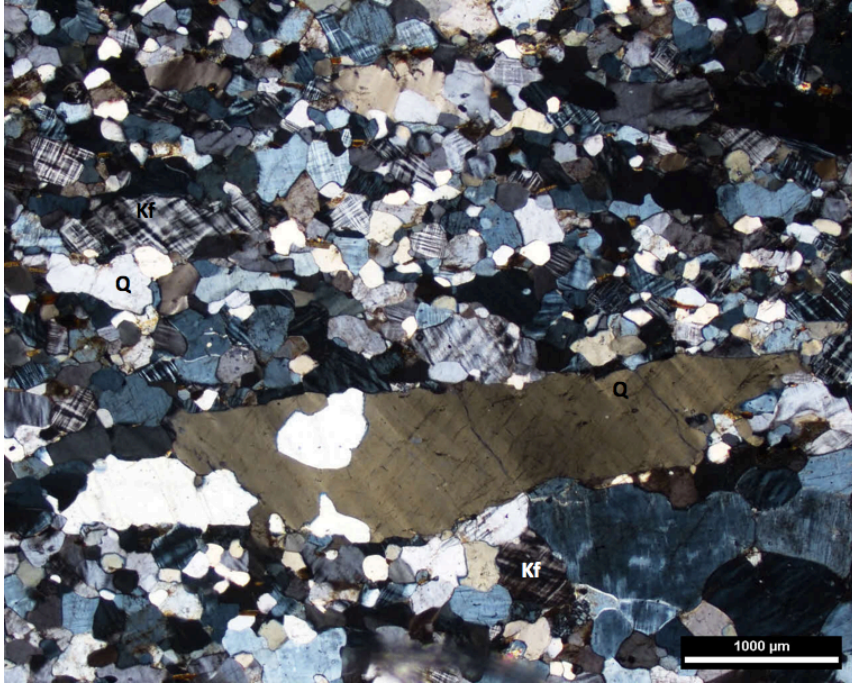
Figure 4-14. Photomicrograph of sample Wcc 4G. Q: quartz, Kf: potassium feldspar. Scale bar = 1000 μm.
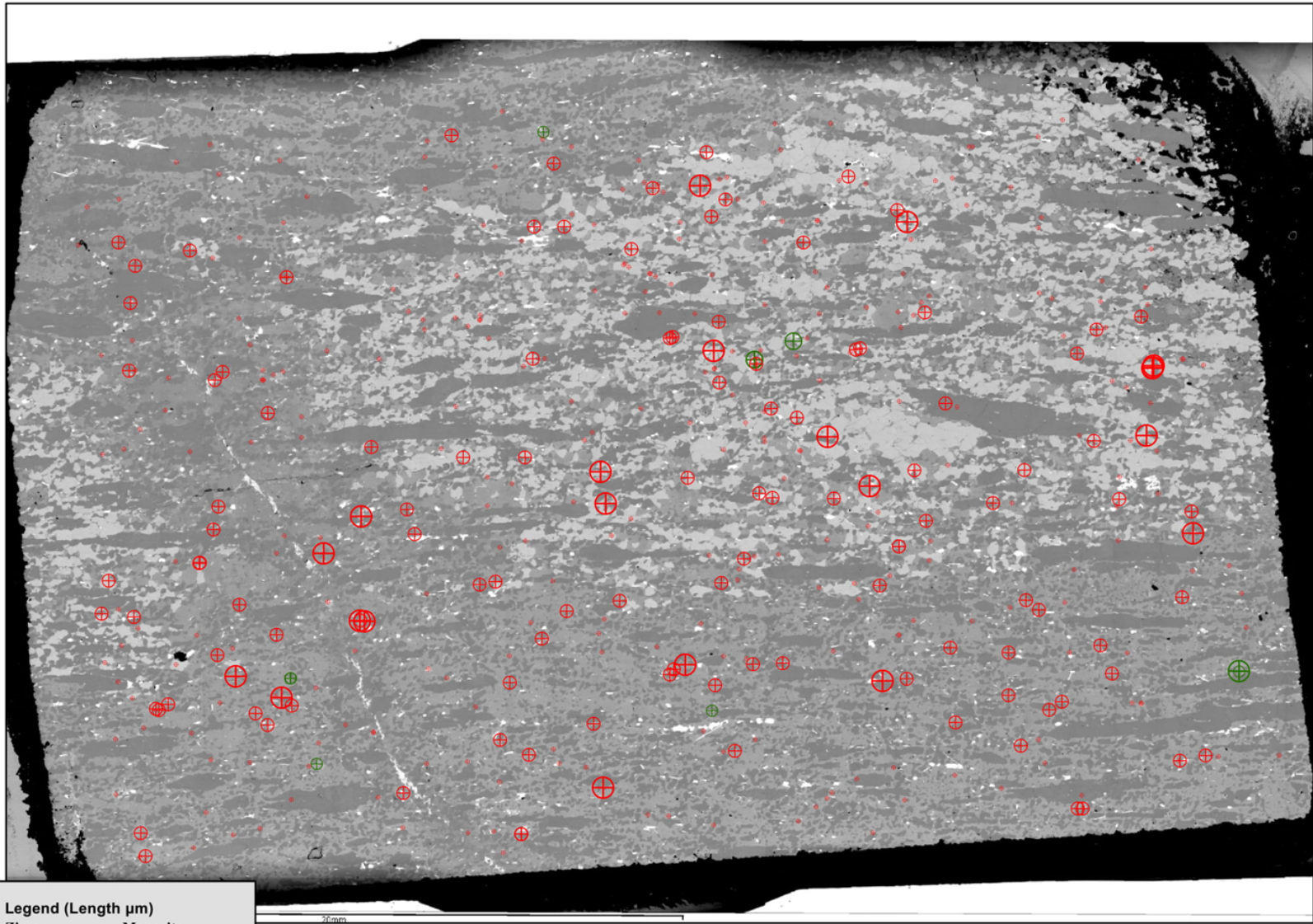
Figure 4-15. MicroGIS map of accessory minerals in sample Wcc 4G. Zircons >10 um.

Figure 4-16. MicroGIS map of zircons imaged with BSE in sample Wcc 4G.
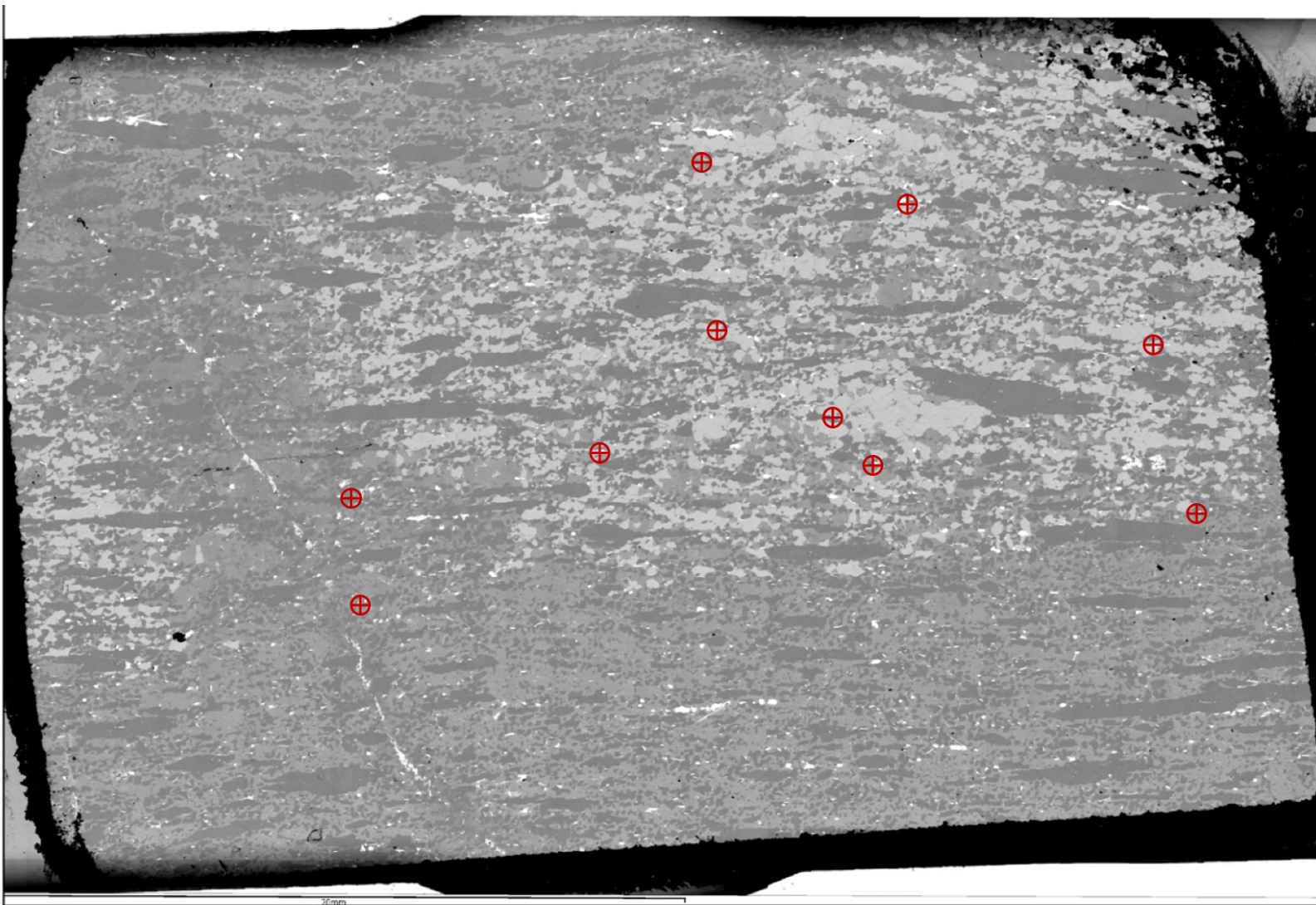
Zircon (not size specific)

0   2.5   5   10 Millimeters

In sample Wcc 4G, 576 zircon grains were identified. Of these, 425 were greater than 10 μm in size, 14 were imaged with BSE imaging. Zircon in sample Wcc 4G is completely metamictized (Figure 4-17: A) with some showing relict oscillatory igneous zoning (Figure 4-17: B). The metamict nature of zircon grains in this sample excluded them from further investigation with EBSD.
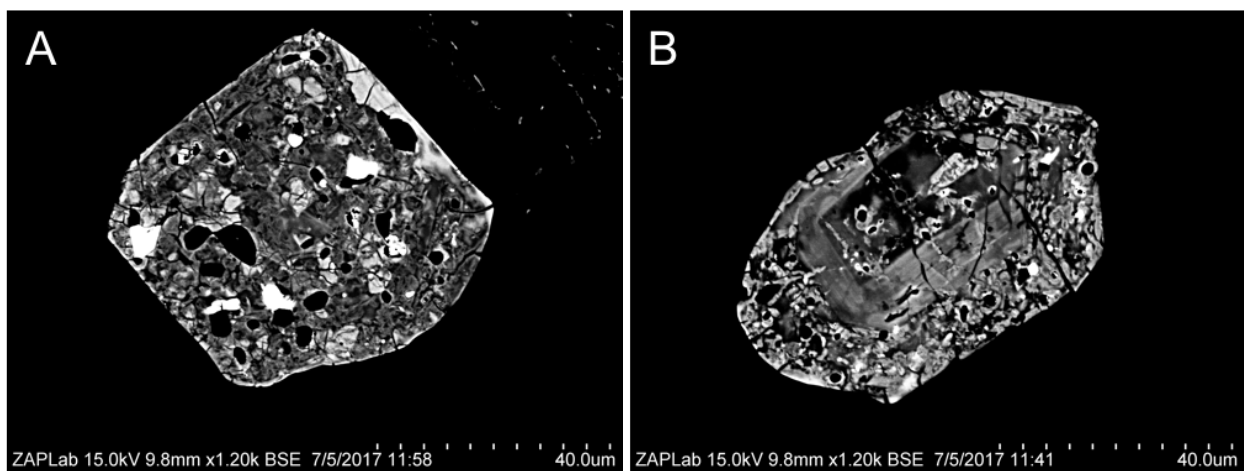
Figure 4-17. (A) Metamict zircon. (B) Metamict zircon with relict concentric zoning.

4.1.4 W2-2 – Garnet-Biotite Quartzofeldspathic Gneiss

Sample mineralogy, fabrics and zircon distribution

W2-2 is a sample of the gneissic country rock collected from the northeast end of the Wanapitei Complex. W2-2 is a garnet-biotite quartzofeldspathic gneiss likely derived from the Huronian Supergroup. Its main mineral assemblage is biotite, garnet, quartz, muscovite and plagioclase feldspar with trace amounts of kyanite (Figure 4-18). Garnet is observed as subhedral porphyroclasts up to 1.5 mm in size and contain significant fractures, chlorite infills fractures in

garnet. Garnet grains in the gneiss are more intact than earlier samples and have few plagioclase inclusions. A large euhedral garnet (5 mm) in the upper left quadrant of the thin section is surrounded by a quartz corona (Figure 4-19). The garnet has inclusions of biotite, opaques, zircon, and one monazite. Biotite defines the foliation (085/79) and bows around the garnets, demonstrating garnets are pre/syn-deformational. Radiation damage of zircons embedded in biotite cause development of pleochroic haloes. Plagioclase displays sericitic alteration. The MicroGIS map of the sample (Figure 4-20) shows even distribution of zircons greater than 10 µm. Zircons range in size up to 36.09 µm. One baddeleyite grain and 25 monazite grains were identified in W2-2. The baddeleyite grain is unconfirmed as it is unlikely to occur naturally in a felsic rock. There is a possibility the baddeleyite grain is detrital; otherwise, it is likely a misidentification. Focused elemental distribution mapping would be required to confirm its identity. Figure 4-21 displays the zircons that were investigated in detail with BSE and EBSD imaging.
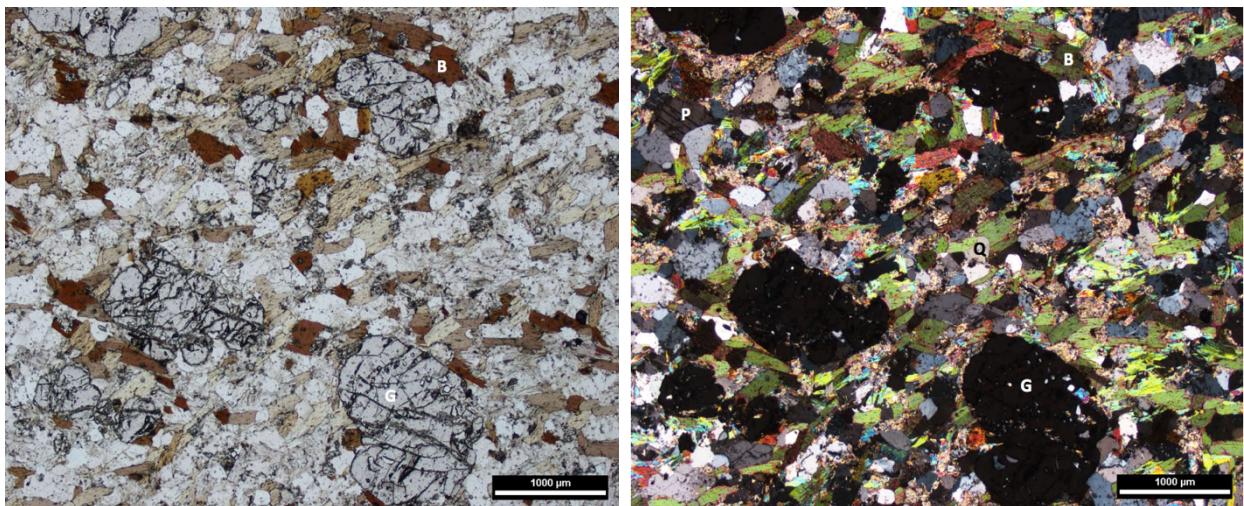
Figure 4-18. Photomicrographs of sample W2-2 in plane polarized light (left) and cross polarized light (right). B: biotite, G: garnet, Q: quartz, P: plagioclase. Scale bar = 1000 µm.
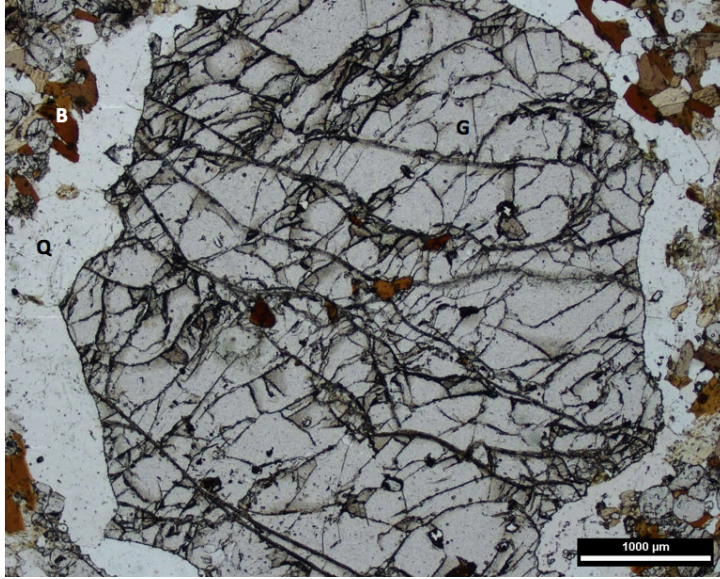
Figure 4-19. 5 mm garnet in sample Wcc 2 surrounded by quartz corona. G: garnet, Q: quartz, B: biotite. Scale bar = 1000 μm.
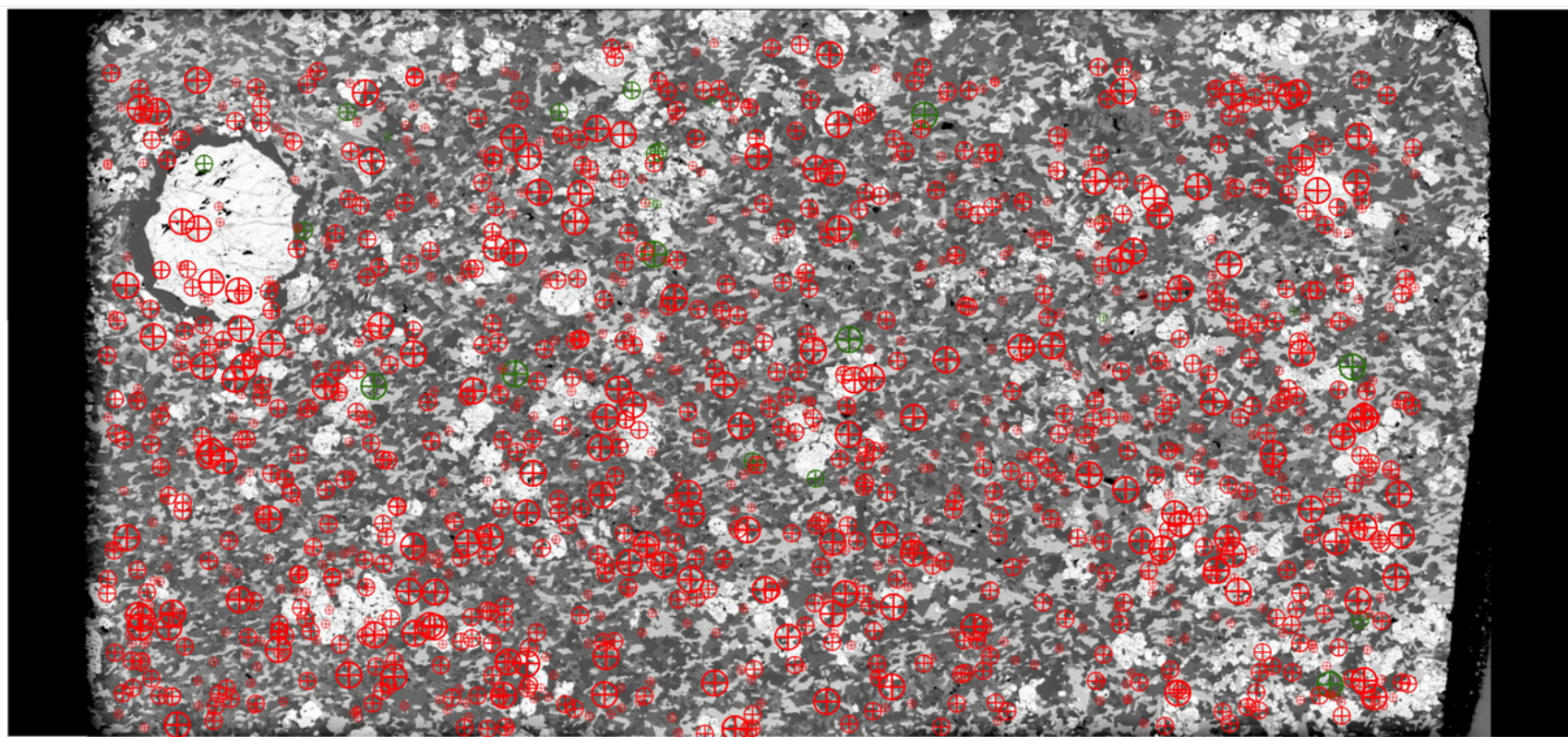
Figure 4-20. MicroGIS map of accessory minerals in sample W2-2. Zircons >10 um.
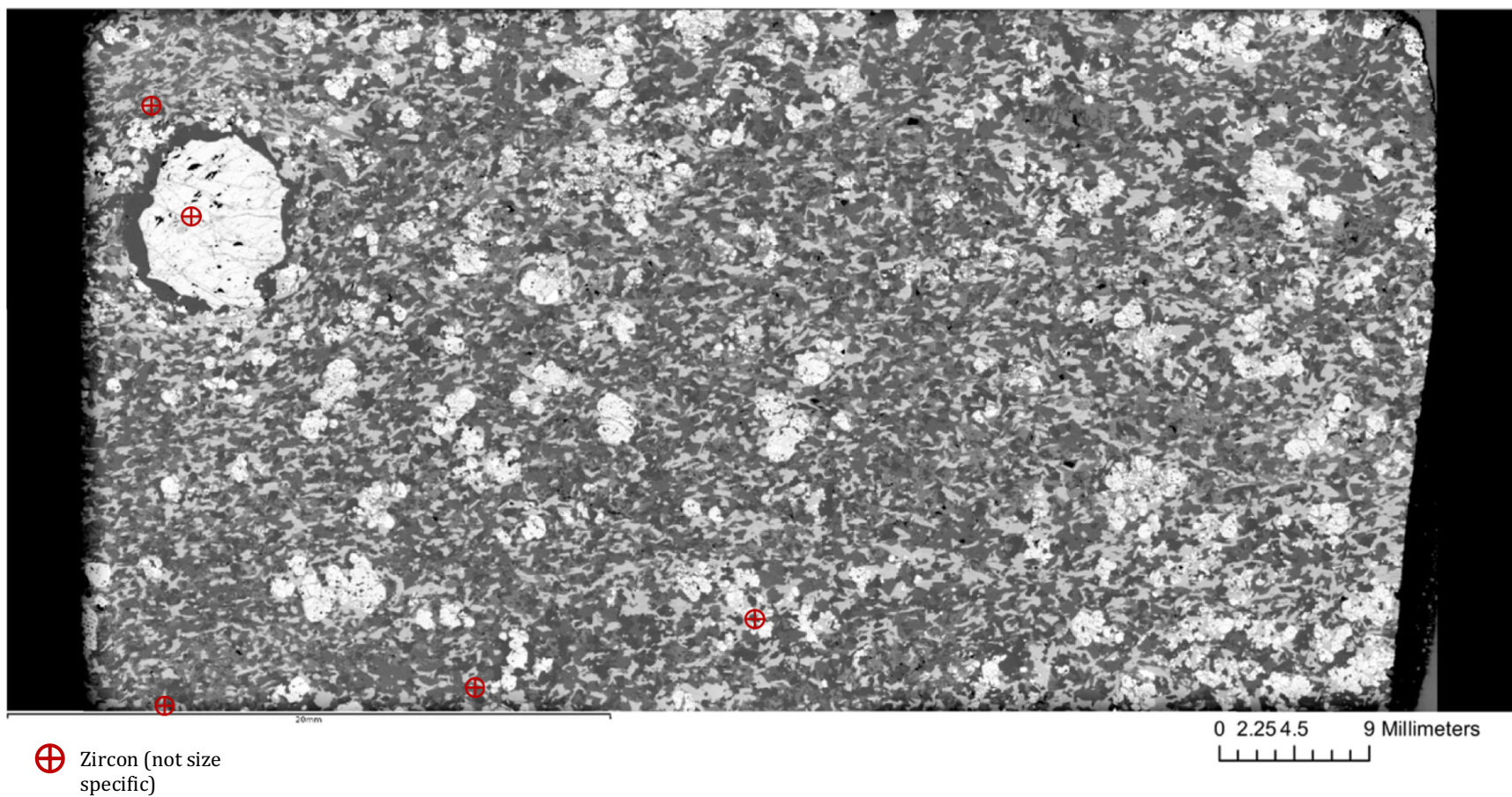
Figure 4-21. MicroGIS map of zircons imaged with BSE and EBSD in sample W2-2.

In sample W2-2, 2328 zircon grains were identified, and of these, 1238 were larger than 10 μm in size. A total of 5 zircon grains were imaged using BSE imaging. W2-2 contains primarily complexly zoned metamorphic zircons. The zircons are anhedral with complex sector zoning (fir-tree zoning) (Figure 4-22: A). Some have metamict cores (possibly detrital) surrounded by metamorphic rims (Figure 4-22: B, C, D). Expansion of metamict cores has resulted in radial fractures of metamorphic overgrowth.
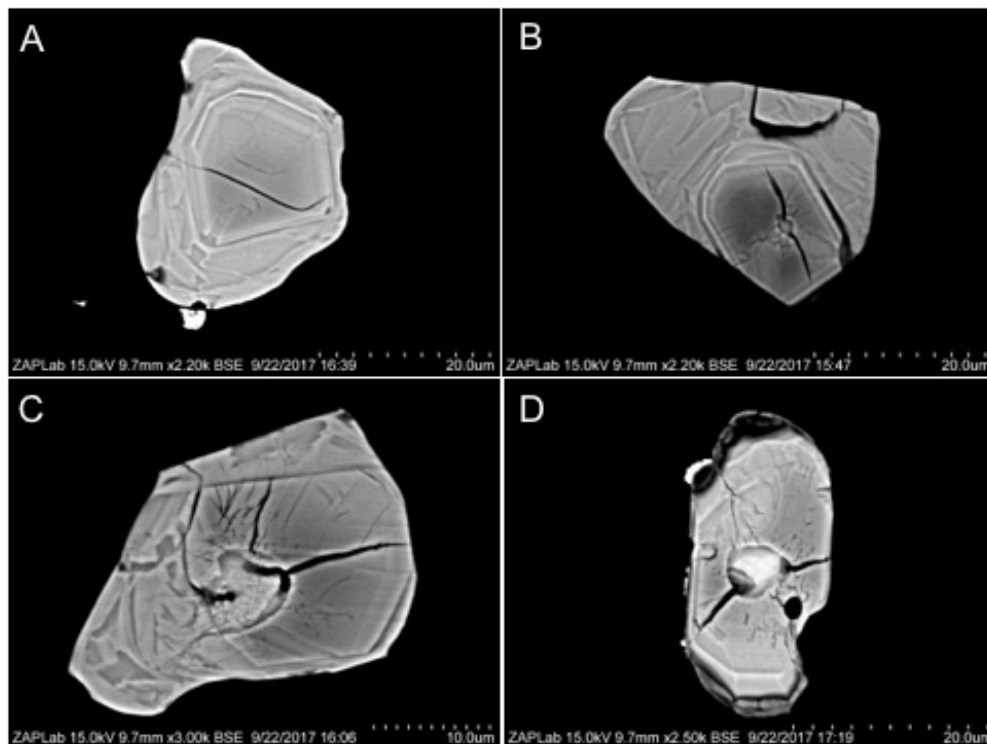
Figure 4-22. (A) Metamorphic zircon with sector zoning. (B, C, D) Metamict cores mantled by complexly zoned metamorphic zircon. Radial fractures due to expansion of cores.

Grain 801 (Figure 4-23) is a metamorphic zircon with a metamict core. The metamict core is unable to be indexed by EBSD. Note Grain 801 is the same grain as imaged in Figure 4-22: C rotated 180°. Micro-zircon can be seen in the matrix around the target zircon in the EBSD map colour coded by phase (Figure 4-23: B). There is no significant distortion (< 2.5°), as displayed by the colour gradient (Figure 4-23: C) and misorientation profile (Figure 4-23: D). Minor variations in orientation can be correlated with brittle fractures. Pole figures colour coded with IPF colouring show the orientation of the target zircon and micro-zircon and display no lattice deformation (Figure 4-24). The two other zircons imaged in sample W2-2 showed a similar degree of deformation (< 3°) and some brittle fracturing.
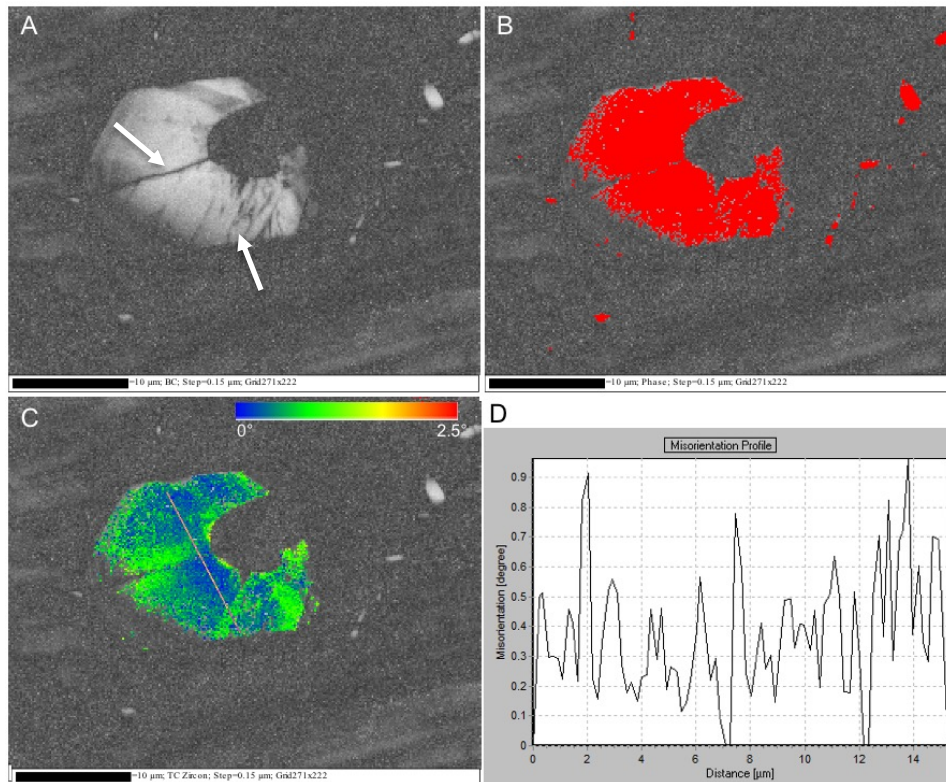
Figure 4-23. Grain 801, metamorphic zircon with metamict core. A: Band contrast image; brittle fractures identified by arrows, metamict core not indexed by EBSD. B: EBSD map colour coded by phase showing micro-zircon. C: EBSD map colour coded by misorientation (misorientation < 2.5°). D: Misorientation profile along line shown in C.
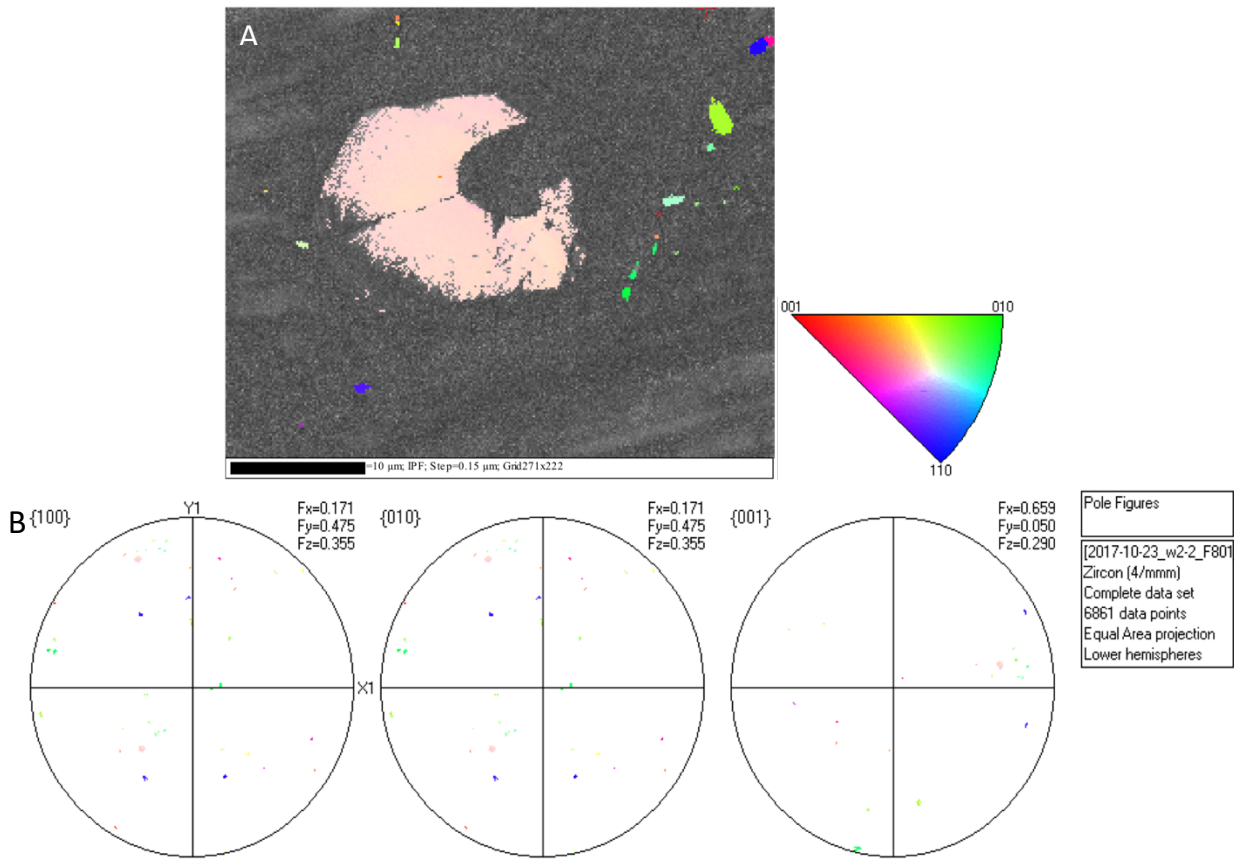
Figure 4-24. Grain 801, metamorphic zircon with metamict core. A: EBSD map with Inverse Pole Figure (IPF) colouring of zircon grains. B: Pole figure plot of grain orientation colour coded with IPF colouring.

In this sample, zircon grains were also imaged from within a 5 mm almandine garnet to compare to matrix zircons due to the contrasting rheological strength of their hosts. A large scale EBSD map (Figure 4-25) indicates that the garnet was not plastically deformed (internal misorientation < 4° with intensive brittle fracturing). Pole figures of the garnet indexed during the focused EBSD also show no deformation (Figure 4-26), the second set of poles is due to a fractured segment of the garnet as indicated by an arrow in Figure 4-26: A. Grain 1770 (Figure 4-27) is hosted by the garnet. The zircon is anhedral and homogeneous and similarly shows no significant internal misorientation (Figure 4-26: C). A small fractured segment gives a slightly

higher internal misorientation of 4°. Therefore, the zircon grains hosted by the matrix and by the

garnet porphyroclast have similar morphologies and misorientation profiles.
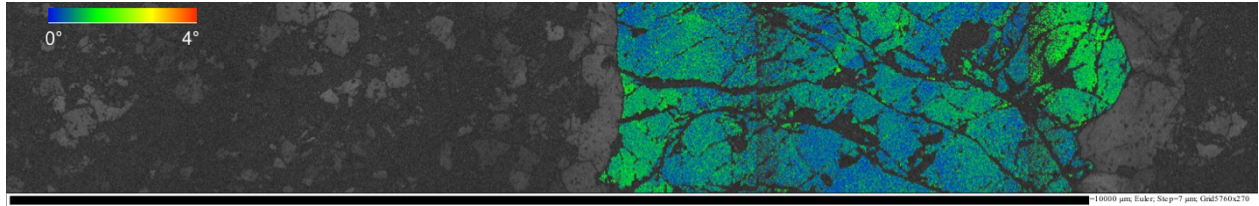
Figure 4-25. EBSD map of almandine garnet in W2-2, cumulative misorientation < 4°.
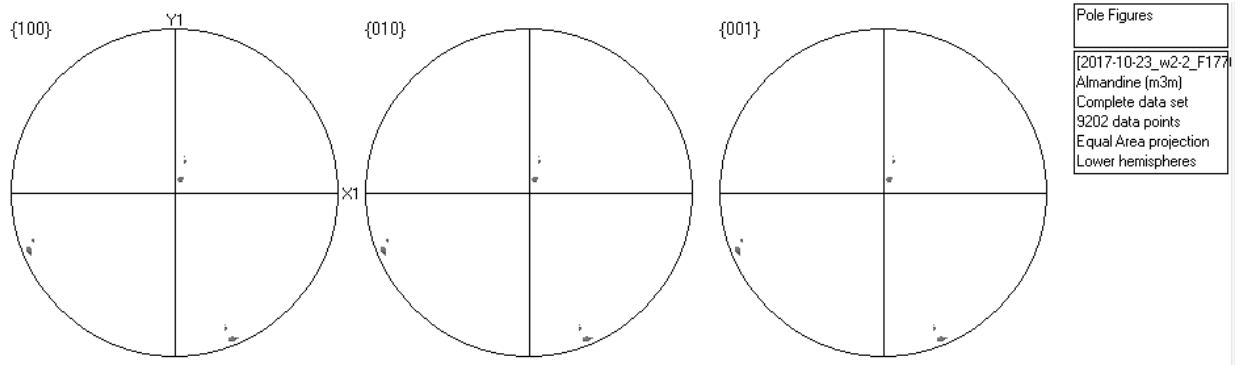
Figure 4-26. Pole figure plots of almandine garnet surrounding Grain 1770.
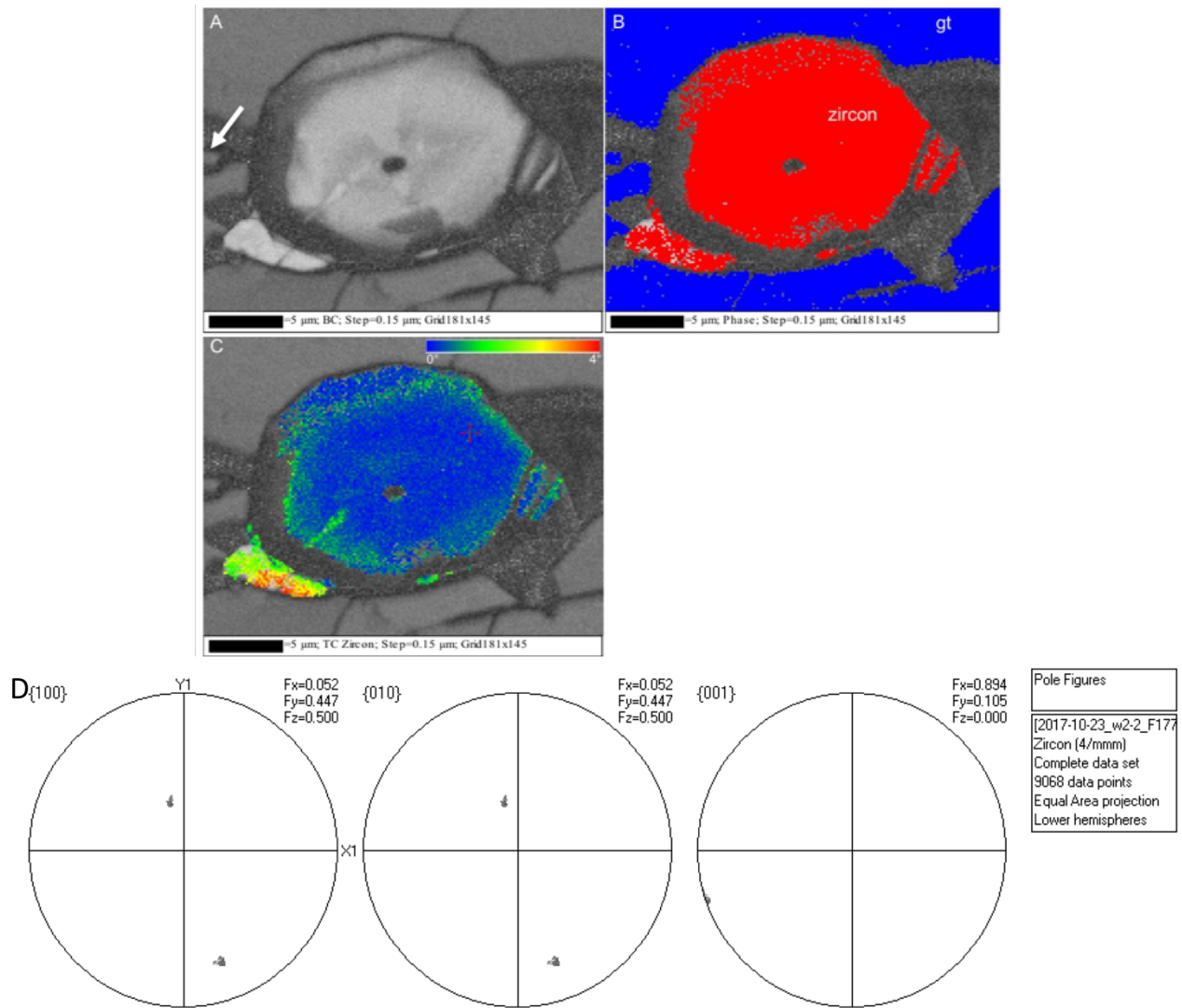
Figure 4-27. Grain 1770, metamorphic zircon contained within almandine garnet. A: Band contrast image; arrow indicates fractured garnet. B: EBSD map colour coded by phase. C: EBSD map colour coded by misorientation (misorientation within zircon < 2.5°). D: Pole figure plot of zircon.

One monazite grain (Grain 3011) was also imaged (Figure 4-28). Misorientation within the main grain is less than ~3°. Pole figures (Figure 4-28: E) show a cluster of orientation due to the fractured segments. Minor deformation is due to brittle fracture (Figure 4-29:), the appearance of 6° of misorientation is due to fractured segments of monazite indicated by an arrow in Figure 4-28: C. In Figure 4-29, micro-zircon that has grown around monazite grain

boundaries and into biotite cleavage is observed. Pole figures (Figure 4-30) show the colour

coded orientation of the micro-zircon.
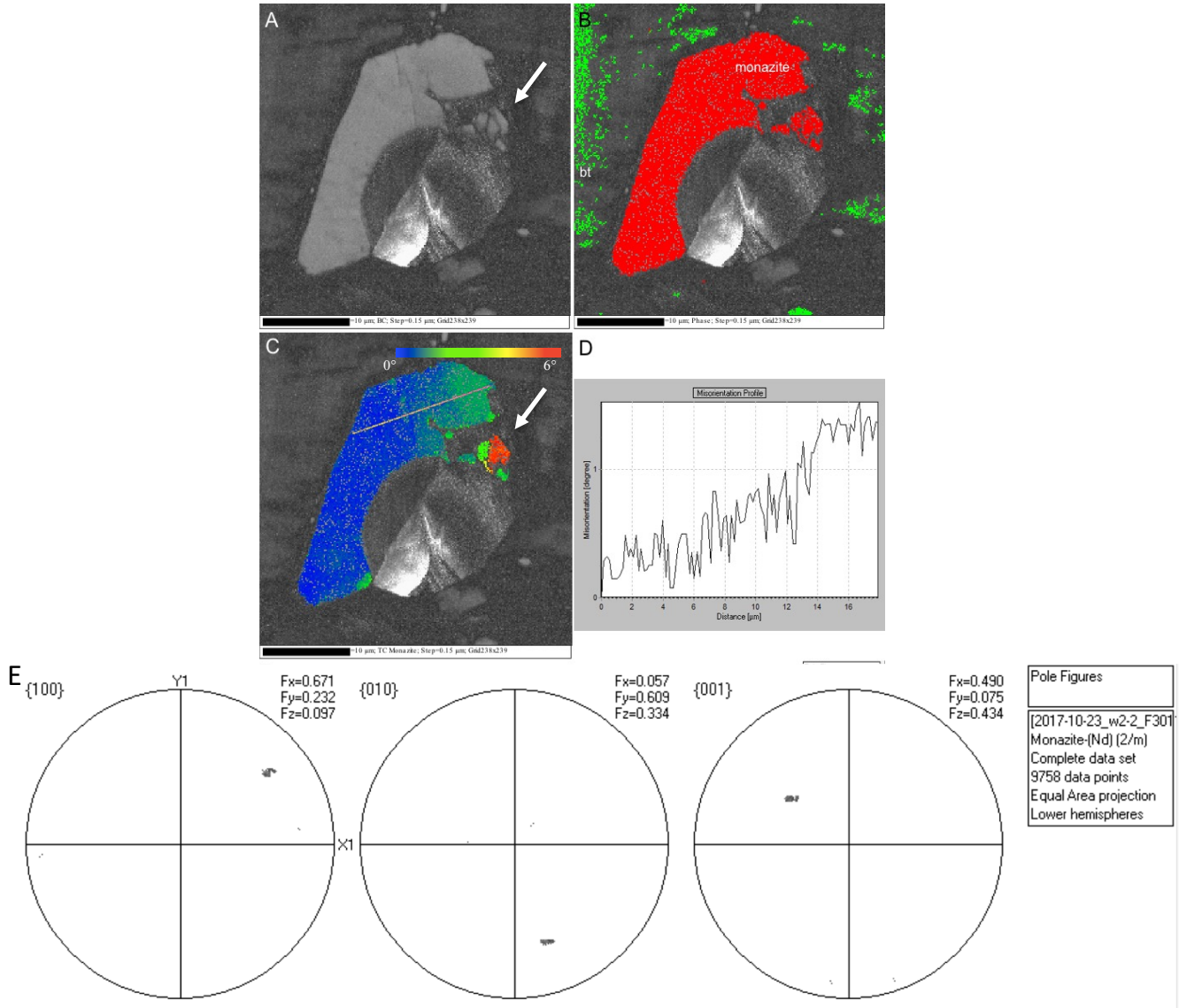
Figure 4-28. Grain 3011, monazite. A: Band contrast image. B: EBSD map colour coded by phase. C: EBSD map colour coded by misorientation (misorientation within monazite < 3°). D: Misorientation profile along line shown in C. E: Pole figure plots of monazite.
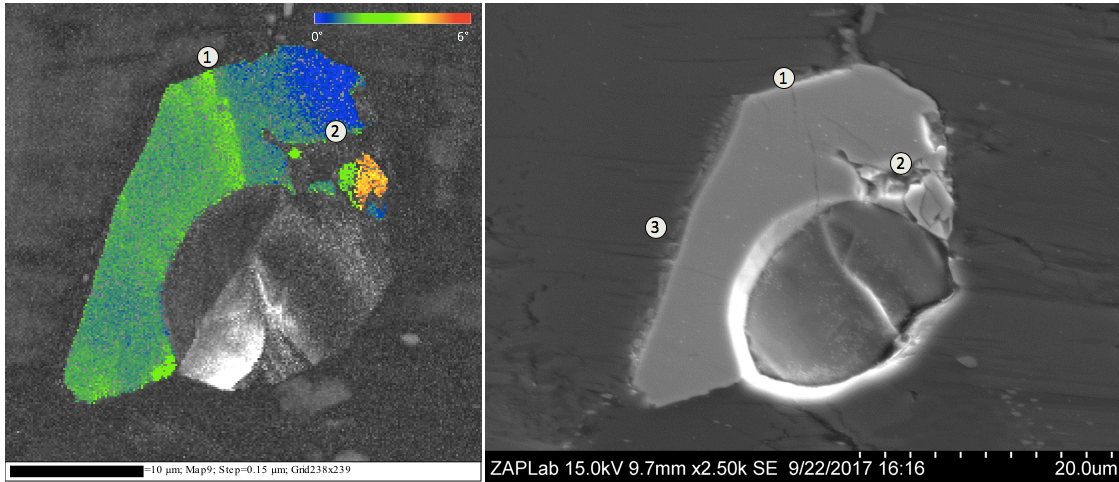
Figure 4-29. Misorientation map (left) and SE image (right) shows misorientation corresponding to brittle fractures (1,2), micro-zircons can be seen in SE image (3).
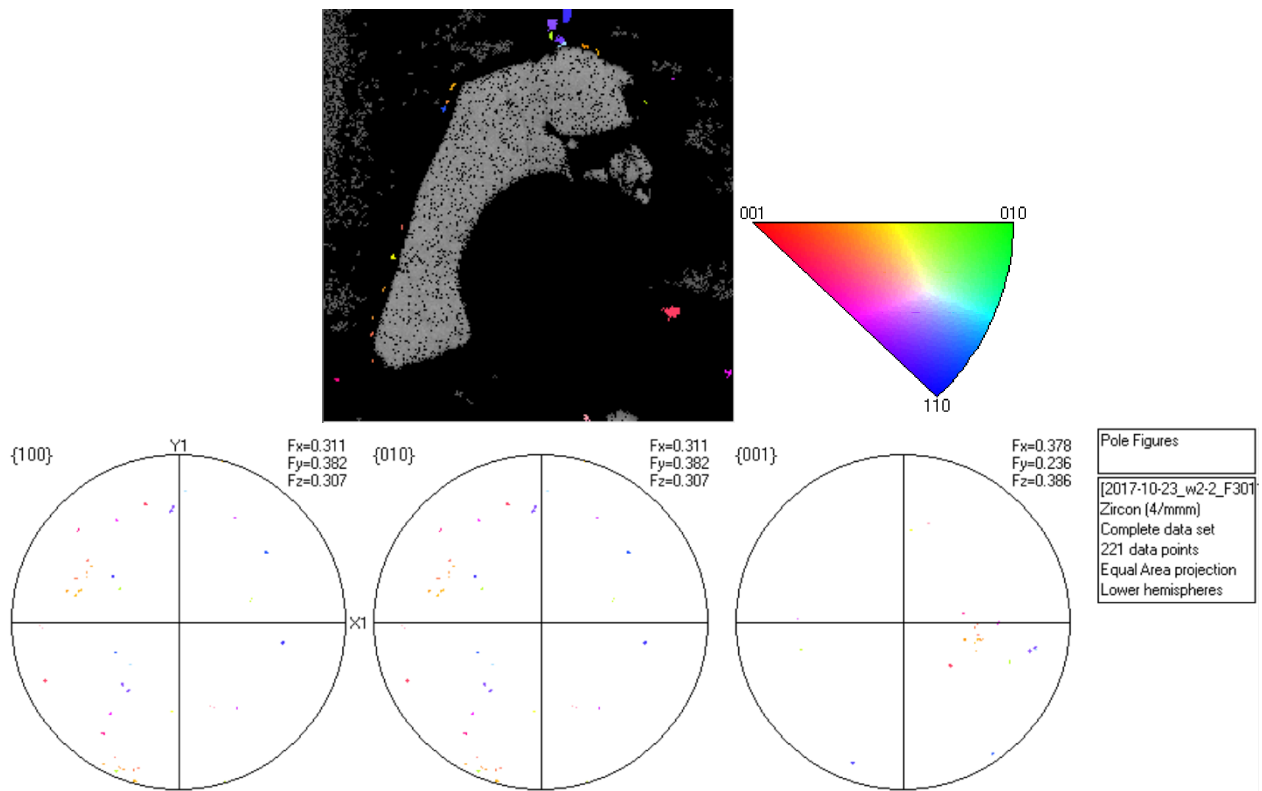
Figure 4-30. IPF colour coded pole figures of micro-zircon.

4.2 Quartz Grain size measurements

Grain size measurements of matrix quartz were made on samples Wcc 4G and W2-2 using NIS elements auto-detect tool. Grain size (in microns) was measured as the equivalent diameter of a circle with the same area. 734 and 334 grains were measured in samples Wcc 4G and W2-2, respectively. The grain size distributions exhibit a positive skew with an extended tail of low frequencies. Full grain size statistics can be found in Appendix C.

4.2.1 Wcc 4G – Deformed Granitic Dyke

The average grain size of recrystallized quartz in Wcc 4G is 136.13 ± 2.2 µm. The grain size distribution (Figure 4-31) is positively skewed. There is an extended tail of low frequency large grain sizes. It is important to note that there may have been a contribution to this tail by the inadvertent inclusion of ribbon quartz. Quartz subgrains exhibiting undulose extinction and low-angle grain boundaries demonstrate the operation of subgrain rotation during deformation-induced recrystallization (Figure 4-32: 1, 2, 3). The broader grain size distribution at higher values is indicative of the transition from SGR to GBM. Values may also be influenced by post-recrystallization grain growth (annealing) as is evident by relatively strain-free grains separated by straight, high-angle boundaries often meeting at angles of 120° (Figure 4-32: 4). Annealing was short-lived as grain growth is minimal. The influence of annealing on subsequent flow stress estimates will be addressed in later sections.
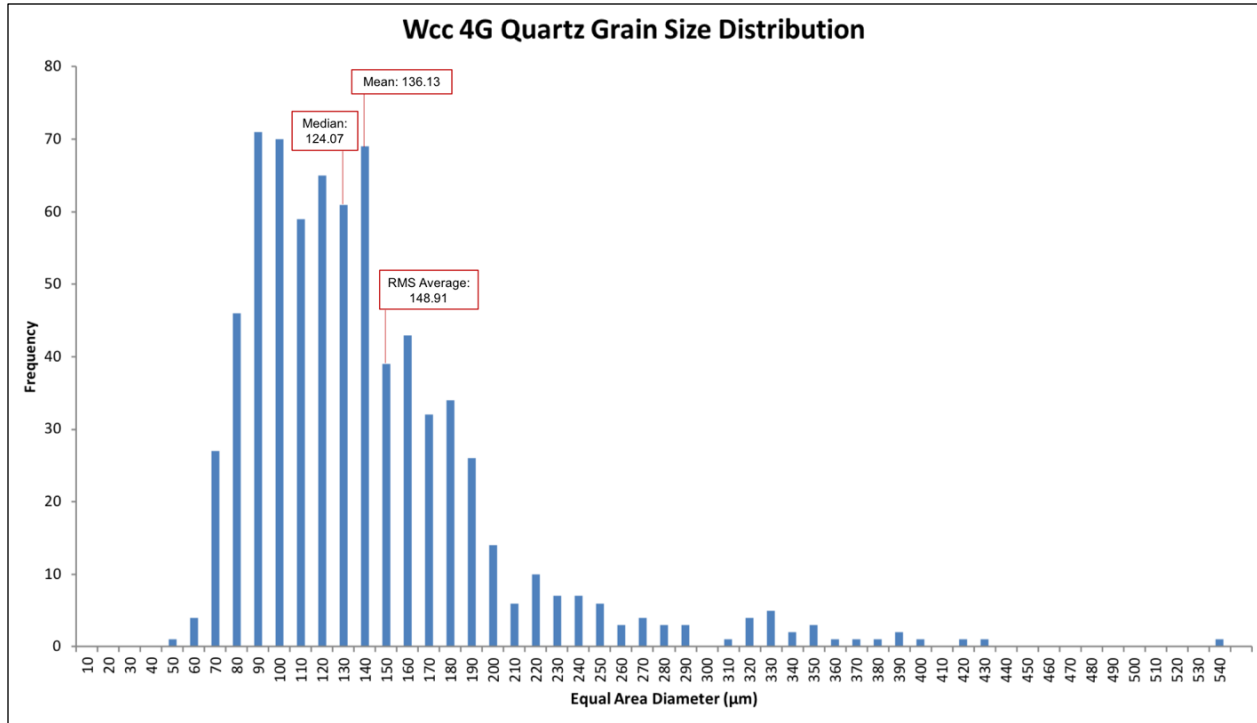
Figure 4-31. Grain size distribution of sample Wcc 4G measured with NIS Elements.
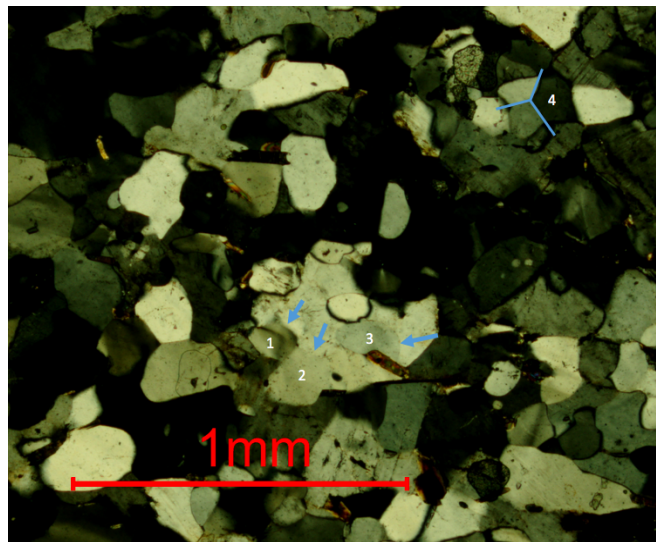
Figure 4-32. Recrystallization features of Wcc 4G. 1: Qtz subgrain exhibiting undulose extinction, 2,3: Qtz subgrains. 4: Recrystallized qtz grains exhibiting 120° triple junction.

4.2.2 W2-2 – Garnet-Biotite Quartzofeldspathic Gneiss

The average grain size of quartz in W2-2 is 196.91 ± 4.1 μm. The grain size distribution has a slight positive skew and a peak at the 150-175 μm bin. Quartz recrystallization has not been activated in sample W2-2. This sample did not recrystallize due to grain boundary pinning by the polymineralic matrix.
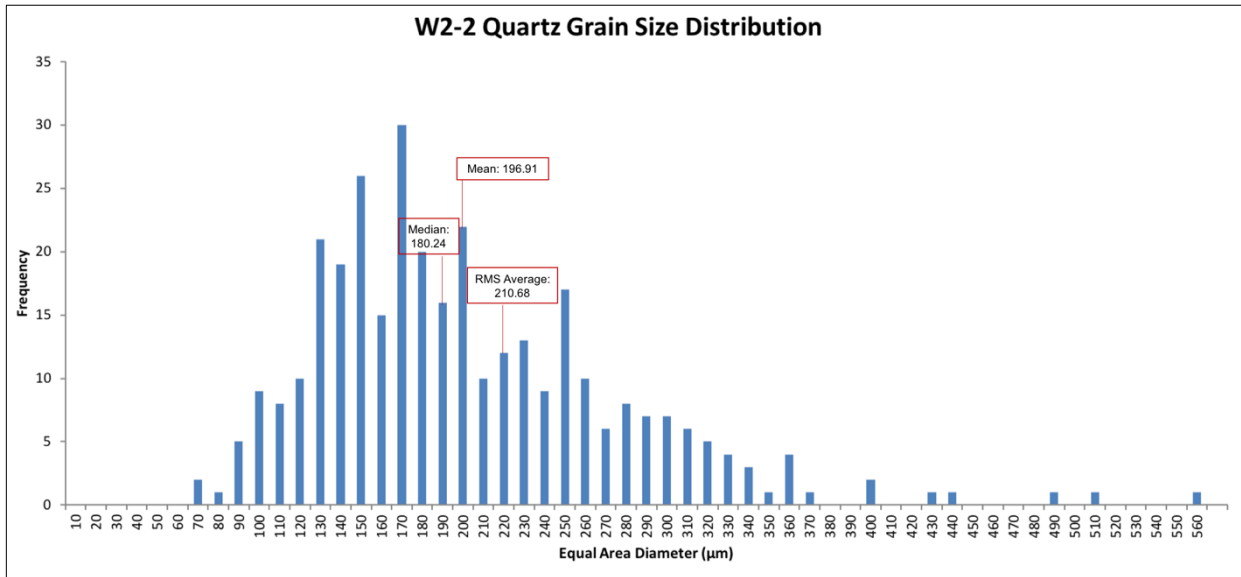
Figure 4-33. Grain size distribution of sample W2-2 measured with NIS Elements.

Chapter 5

5 Interpretations

5.1 Interpretation of Microstructural Analysis

In situ investigation of zircons in these samples revealed that they are not plastically deformed and no eligible targets for zircon strain chronometry were identified. Zircon grains displayed minimal internal lattice misorientation, below the extent that has been observed to correlate with enhanced Pb diffusion (i.e. ~0.3°/um (Piazolo et al., 2012); ~3-40° cumulative misorientation (Kovaleva et al., 2014)). Complete metamictization of zircons in Wcc 4G (granitic dyke) rendered them unsuitable for EBSD examination. Zircons in both samples of the Wanapitei metagabbro (Wcc 4M and Wcc) were either igneous with significant resorption and metamorphic overgrowth or wholly metamorphic, few euhedral igneous zircons remained. Igneous zircons and relict igneous cores showed internal misorientation under 3°. Metamorphic zircon in the Wanapitei metagabbro had internal misorientation under 3.5° with some misorientation owing to post-metamorphic fracturing. In the quartzofeldspathic gneiss country rock (W2-2), metamict cores were surrounded by complexly zoned metamorphic rims. The metamorphic rims had misorientation of under 3° that can be accounted for by post-metamorphic fracturing due to zircon volume increase during metamictization.

Additionally, there was no correlation between zircon morphology and location within specific structures or hosts. Despite the difference in composition between rock samples, zircons showed similar features in each sample and were devoid of any significant internal misorientation. In sample Wcc 2, zircons from the feldspar-rich, larger-grain bands and the feldspar/mica, smaller-grain bands displayed no difference in morphology. In sample W2-2,

zircons in the rheologically weaker matrix showed the same internal features as the zircons investigated within garnet.

Furthermore, the size and condition of zircon grains were not conducive to complete zircon strain chronometry. First, homogenous, featureless morphology of zircons in W2-2, as well as the presence of triple junction grain boundaries, suggests recovery by annealing in the country rock sample. The presence of annealing warrants the inference that any strained lattice domains would have recovered and experienced subsequent Pb loss, affecting any isotopic age calculations violating Moser et al. (2009)'s condition (1) for zircon strain chronometry. Second, the small grain size of zircon, minimal distortion and presence of brittle fracturing inhibits the ability to obtain sufficient analytical and spatial resolution of discordance as in Moser et al. (2009)'s condition (3) for zircon strain chronometry. Zircon grains in these samples displayed < 3° of cumulative misorientation with ~0.5° of noise with < 1% of ~6000 zircon grains being larger than 50 μm in size. The size and deformation of these zircons is not substantial enough to date with sufficient resolution or to correlate internal microstructures to deformational fabrics. This would also present problems when considering the Kovaleva et al. (2017) suggestion that to avoid contamination, U-Pb isotopic analyses should be done at a distance ~5 μm from the deformation front and 5-10 μm from boundaries.

Two additional accessory phases, baddeleyite and monazite, were also investigated. Like zircon, baddeleyite and monazite can be useful geochronological tools due to their ability to withstand metamorphism. There are no known occurrences of metamorphic baddeleyite in tectonic settings (Heaman and LeCheminant, 1993). Therefore, baddeleyite was inspected in these samples to observe the microstructural response of a mineral of known igneous origin (i.e. pre-deformation). The two baddeleyite grains in metagabbroic sample Wcc 4M were very fine-

grained (<10 μm) and showed no internal distortion. The lack of distortion in baddeleyite demonstrates that regional deformation of the Wanapitei Complex was not significant enough to result in permanent deformation. Monazites were indexed in all four samples (two in Wcc 4M, two in Wcc 2, 10 in Wcc 4G, 26 in W2-2). One monazite grain was imaged in the country gneiss, W2-2, because it was initially mis-indexed as zircon; investigation with the HKL "Tango" re-identified the grain as monazite. Misorientation within the monazite (Grain 3011) was attributed to brittle fracture rather than plastic deformation (Figures 4-28 to 4-30).

Due to lack of internal distortion in geochronological accessory phases, correlation of isotopic ages to the D_3 deformational event cannot be completed. U-Pb dating would not provide dates with any more specificity or confidence than work by Li (2012); therefore, isotopic dating was not pursued. Subsequently, the objective of this thesis evolved to explain why zircons are not deformed by investigating stress conditions in the Grenville Front.

5.2 Stress Estimates from Quartz Piezometers

5.2.1 Determination of parameters

Piezometers are relations between microstructural characteristics such as grain size and the differential stress that produced the microstructure. Various piezometers have been proposed and calibrated. The method of calibration, equations used, and parameter values of the quartz piezometers used are outlined below and summarized in Table 2.

<u>Stipp and Tullis (2003)</u>

In Stipp and Tullis (2003) grain size was measured in equal diameter with average grain size calculated as the root mean square (RMS) diameter. Grain size for this thesis was measured using NIS Elements and manual exclusion of quartz porphyroclasts. Like Stipp and Tullis

(2010), no stereological correction was applied. The *Regime 2/3* relation (Eq. (3): $D = 10^{3.56 \pm 0.27} \cdot \sigma^{-1.26 \pm 0.13}$) is deemed most appropriate due to the operating recrystallization mechanisms of SGR and GBM in sample Wcc 4G and large grain size of sample W2-2. Stipp and Tullis (2010) recommended that the piezometer of Stipp and Tullis (2003) was most applicable to grain sizes < 46 μm, applied reasonably well to the range of grain sizes between 46 and 120 μm and underestimated flow stress for recrystallized grain sizes >120. Due to the large grain size in these samples (~200 μm average), an underestimation of flow stress may occur. With this consideration in mind, the Stipp and Tullis (2003) piezometer for *Regimes 2/3* is regarded as an appropriate relation to estimate flow stress in these samples.

Austin and Evans (2007)

Next, the paleowattmeter of Austin and Evans (2007), Eq. (4): $d_s^{1+p} = \frac{K_g \exp{(\frac{-Q_g}{RT})} p^{-1} c \gamma}{\lambda \sigma \dot{\varepsilon}_{disl}}$, will also be used to estimate flow stress. The flow law of Lu and Jiang (2019) (Eq. (5): $\dot{\varepsilon} = 6.0 x 10^{-15} f_w^{2.7} \exp{(-\frac{132000 + 35.3P}{RT})} \sigma^4$) is used to calculate the dislocation creep strain rate in the above piezometric equation. Temperature and pressure estimates for this region are limited. They also present a challenge in that metamorphic conditions cannot be linked directly to P-T conditions of D$_3$ deformation recrystallized grain size. For this study, temperature and pressure estimates are from conditions calculated from samples of similar composition in the Grenville Province by Murphy (2001). Equilibrium conditions of the independent reactions of six anhydrous phases (kyanite, garnet, biotite, muscovite, plagioclase, quartz) in metapelites of the Grenville near Coniston Creek Area yielded P-T conditions: P=8.1 ± 1 kbar, T=684 ± 50°C. Garnet-Biotite thermometry yielded conditions: P=8.1 kbar, T=715°C. The anhydrous phase estimates along with error will be used to calculate the possible range of stress conditions.

Fugacity is calculated after Sterner and Pitzer (1994) using a Matlab code of the Western University structural geology lab. Grain growth parameters used are p = 3.2, Q_g = 215 kJ/mol, K_g = 1.3e8 (Wightman et al., 2006), γ = 0.5 J/mol^2 (Brace and Walsh, 1962), λ = 0.1 (Austin and Evans, 2009), c = π, and R = 8.314 J·K^{-1}·mol^{-1} as cited in Austin and Evans (2007, 2009). Grain size is measured as the average equal diameter.

Shimizu (2012)

The Shimizu piezometer is calibrated based on SGR and GBM as operating recrystallization mechanisms and is, therefore, an appropriate relation to apply to sample Wcc 4G. Stress estimates will also be made for sample W2-2. Temperature estimates in this region (Murphy, 2001) are greater than the transition temperature of α to β quartz (573°C), subsequently, the paleopiezometer of Shimizu (2012) for β quartz is utilized, Eq. (10): $d = 1.82 \cdot 10^3 \cdot \sigma^{-1.25} \exp\left(\frac{7.25\frac{kJ}{mol}}{RT}\right)$. Median recrystallized grain size is used as steady state grain size (d).

Parameters used for these estimates are recorded below (Table 2).

Table 2. Parameters used for quartz piezometry.

Sample	Median d (μm)	Avg d (μm)	RMS Avg d (μm)	T [C] (Murphy 2001)	P [MPa] (Murphy 2001)
Wcc 4G	124	136	148	684 ± 50	810 ± 100
W2-2	180	196	210	684 ± 50	810 ± 100

5.2.2 Stress Estimates: Wcc 4G

Quartz recrystallized grain size reflects differential stress estimates of 12.5 MPa (based on Stipp and Tullis, 2003) with RMS average grain size 148.91 μm, ~4-4.8 MPa (based on Austin and Evans, 2007) with average grain size 136.13 μm and ~17-18.5 MPa (based on Shimizu, 2012) with median grain size 124.07 μm (Figure 5-1).
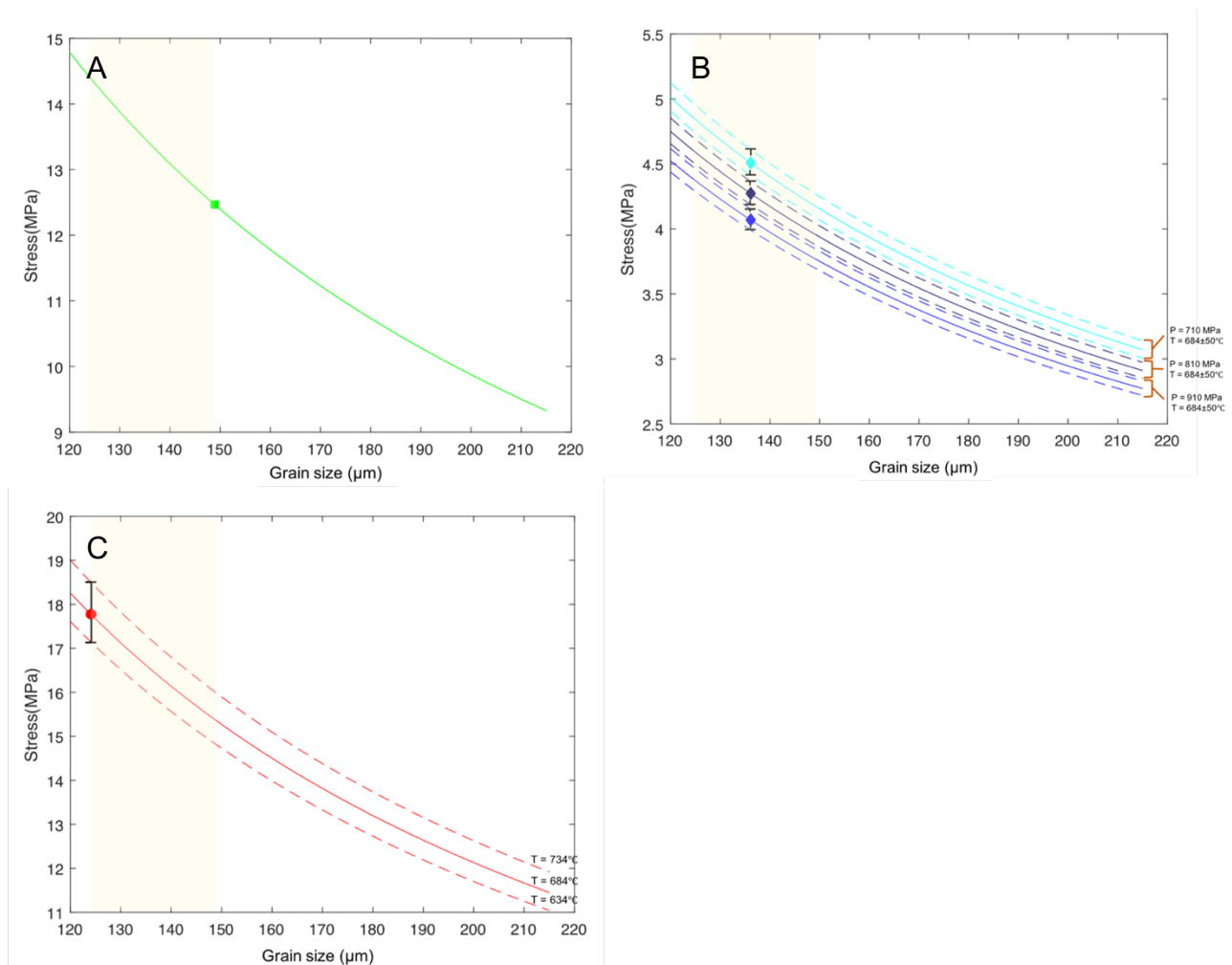
Figure 5-1. Stress estimates based on quartz piezometry of sample Wcc 4G. A: Estimated stress based on Stipp and Tullis (2003), B: Estimated stress based on Austin and Evans (2007) with P = 810 ± 100 MPa and T = 684 ± 50ºC, D: Estimated stress based on Shimizu (2012) with T = 684 ± 50ºC. Shaded region indicates range of results due to different methods of recrystallized grain size measurement.

5.2.3 Stress estimates: W2-2

Quartz grain size in the country rock reflects flow stress estimates of 9.5 MPa (Stipp and Tullis, 2003) with RMS average grain size of 210.68 μm, ~3-3.6 MPa (Austin and Evans, 2007) with average grain size of 196.91 μm, and ~13-13.7 MPa (Shimizu, 2012) with median grain size of 180.24 μm (Figure 5-2).
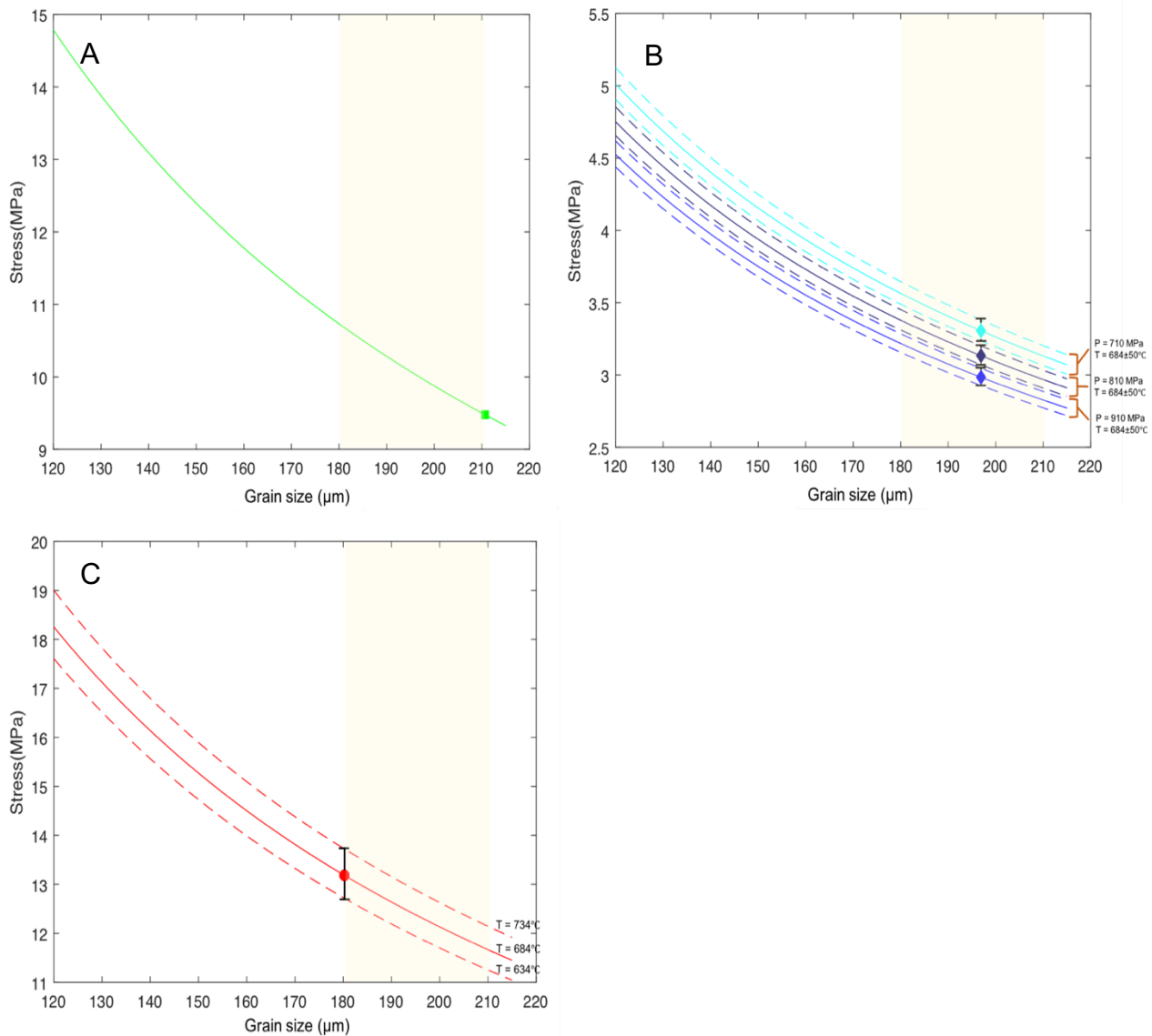
Figure 5-2. Stress estimates based on quartz piezometry of sample W2-2. A: Estimated stress based on Stipp and Tullis (2003), B: Estimated stress based on Austin and Evans (2007) with P = 810 ± 100 MPa and T = 684 ± 50ºC, D: Estimated stress based on Shimizu (2012) with T = 684 ± 50ºC. Shaded region indicates range of results due to different methods of recrystallized grain size measurement.

5.2.4 Piezometry Summary

The quartz grain size piezometers of Stipp and Tullis (2003), Austin and Evans (2007) and Shimizu (2012) produce stress estimates of 4-18.5 MPa (Wcc 4G) and 3-13.7 MPa (W2-2). The estimates obtained from sample Wcc 4G (granitic dyke) likely represent a minimum value of stress in the region. Partial foam texture from annealing can result in underestimates of flow stress due to grain growth (Kidder et al., 2012, 2016). However, Francsis (2012) suggested that underestimates of flow stress due to large grain size from annealing under low-stress conditions are insignificant and would be less than a few 10's of MPa. As discussed in later sections, an underestimate of this magnitude would not have a significant impact on the results. Accordingly, estimates from sample Wcc 4G are considered conservative. Differential stress estimates from W2-2 cannot be verified as minimal dynamic recrystallization of quartz in W2-2 places this sample beyond the applicability of piezometers. Piezometers are calibrated based on the activation of the dislocation creep mechanism, the lack of recrystallization in the country rock signifies that the dislocation creep mechanism was not activated and therefore quartz grain sizes are not reflective of the differential stress in the area. As seen in Figures 5-1 and 5-2, the method of calculation of steady state grain size did not have a significant impact on stress estimate in these samples.

To assess the accuracy of these results, the differential stress estimates from each piezometer are compared to previous results as well as quartzite flow laws in Figure 5-3 to 5-5. Previous results are plotted by dominant recrystallization mechanism when known (BLG: bulging recrystallization, SGR: subgrain rotation recrystallization, GBM: grain boundary migration). The shaded region shows results that correspond to geologically reasonable strain rates (10^{-13} to 10^{-11} s^{-1}) using the flow law of Lu and Jiang (2019). Flow laws of Gleason and

Tullis (1995), Luan and Paterson (1992) and Rutter and Brodie (2004) are also plotted. The

Matlab codes used to plot the results were provided by Lu and Jiang (2019). These plots show

that the stress estimates agree with previously reported results at high temperature and low

differential stress across all three piezometers. However, the results of the individual piezometers

vary significantly. The wattmeter scaling relation (Austin and Evans, 2007) consistently displays

the lowest stress estimates while the Shimizu model (Shimizu, 2012) returns the highest. In fact,

when compared to the flow laws, the results using the paleowattmeter displays considerable

discrepancies and appears to significantly underestimate stress as pointed out in Lu and Jiang

(2019), while the piezometers of Stipp and Tullis (Figure 5-3: A) and Shimizu (Figure 5-3: C)

show more congruent estimates with flow laws. Kidder et al. (2012) found that when

extrapolated to natural conditions the paleowattmeter could significantly underestimate different

stress, by up to an order of magnitude. In Figure 5-3: B it can be seen that the divergence of

stress estimates from geological flow laws increases with increasing differential stress and

decreasing temperatures. While this may not be of great consequence in low stress/high-

temperature conditions such as in the Grenville Front, flow stress may be significantly

underestimated in low-temperature/high-stress samples. Therefore, the accuracy of the

paleowattmeter is ambiguous. The similar magnitudes of estimated stress by Stipp and Tullis

(2003) and Shimizu (2012) and their agreement with quartz flow laws suggest that Austin and

Evans (2007) produces an underestimate of strain by one order of magnitude in these samples.

The piezometer of Stipp and Tullis (2003) has been found to be accurate in natural

samples at low temperatures (Kidder et al., 2012) and with grain sizes smaller than 120 μm

(Stipp and Tullis, 2010). The applicability of this grain size piezometer at grain sizes greater than

120 μm has not been sufficiently explored. Nevertheless, due to the agreement with previous

studies and quartz flow laws Stipp and Tullis (2003) and Shimizu (2012) produce the most

accurate stress estimates in these samples and report a maximum differential stress of 18.5 MPa.
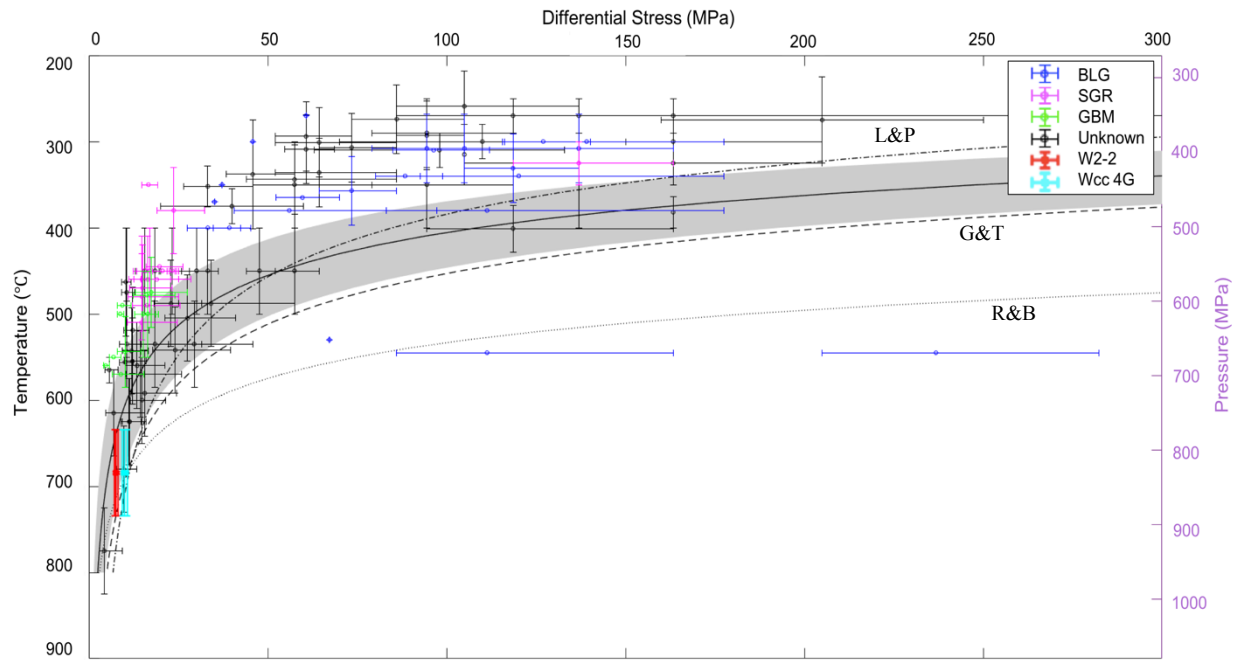
Figure 5-3. Differential stress of Wcc 4G and W2-2 predicted by Stipp and Tullis (2003) compared to quartzite flow laws of Gleason and Tullis (1995), Luan and Paterson (1992) and Rutter and Brodie (2004) at a geothermal gradient of 20°C/km and strain rate of $10^{-12}s^{-1}$ and estimated results of natural mylonites. Shaded region is the flow law of Lu and Jiang (2019) with strain rate between $10^{-13}s^{-1}$ and $10^{-11}s^{-1}$. Modified from Lu and Jiang (2019).
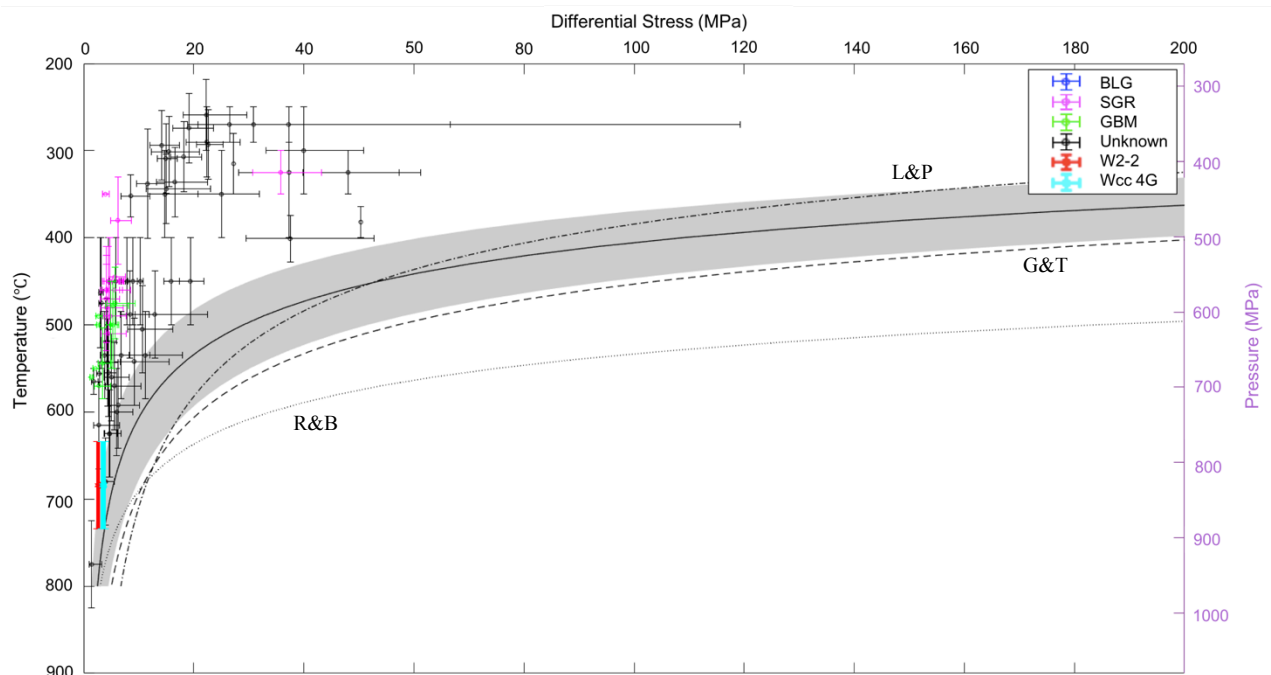
Figure 5-4. Differential stress of Wcc 4G and W2-2 predicted by Austin and Evans (2007) compared to quartzite flow laws of Gleason and Tullis (1995), Luan and Paterson (1992) and Rutter and Brodie (2004) at a geothermal gradient of 20°C/km and strain rate of $10^{-12}s^{-1}$ and estimated results of natural mylonites. Shaded region is the flow law of Lu and Jiang (2019) with strain rate between $10^{-13}s^{-1}$ and $10^{-11}s^{-1}$. Modified from Lu and Jiang (2019).
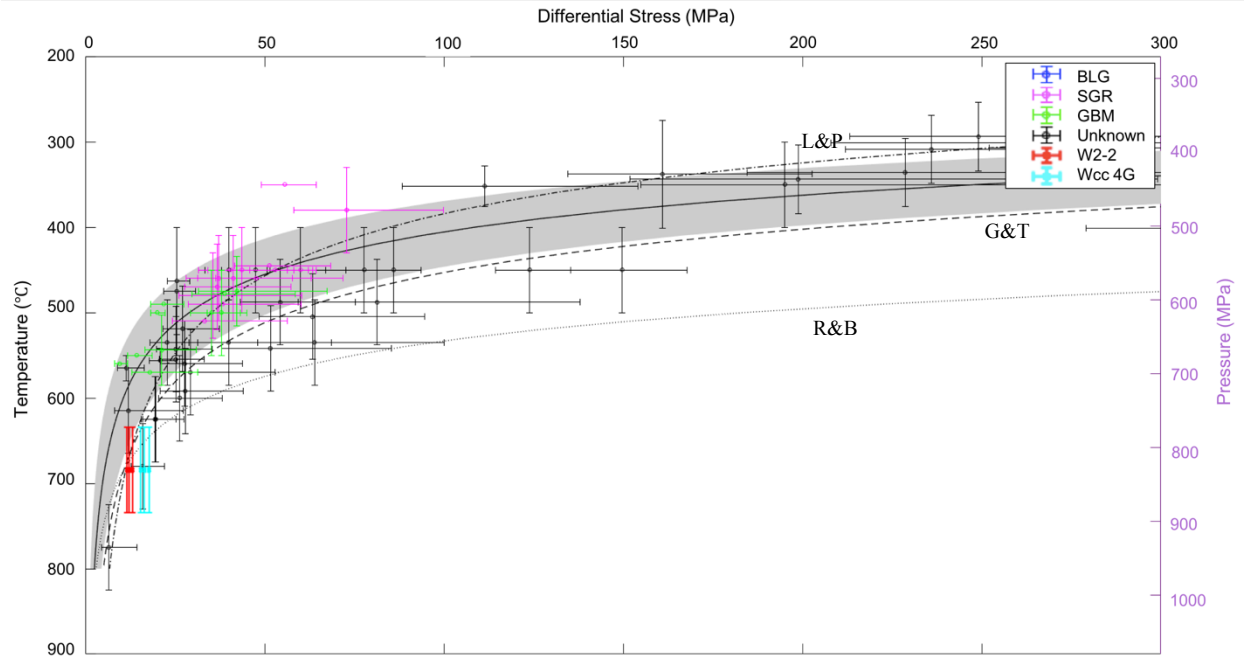
Figure 5-5. Differential stress of Wcc 4G and W2-2 predicted by Shimizu (2012) compared to quartzite flow laws of Gleason and Tullis (1995), Luan and Paterson (1992) and Rutter and Brodie (2004) at a geothermal gradient of 20°C/km and strain rate of 10^{-12}s^{-1} and estimated results of natural mylonites. Shaded region is the flow law of Lu and Jiang (2019) with strain rate between 10^{-13}s^{-1} and 10^{-11}s^{-1}. Modified from Lu and Jiang (2019).

Chapter 6

6 Discussion

The direct dating of deformation fabrics with accessory minerals has the potential to be very useful in tectonic studies of areas such as the Grenville Front. Using quartz piezometry it is now possible to assess whether or not conditions were appropriate to deform zircon in the Wanapitei area. The current chapter will address the response of zircon to regional deformation in these samples and the implications of these results.

6.1 Microstructural Response of Zircon and Implications for Isotopic Dating of the Grenville Front

There is no evidence of zircon lattice distortion in these samples that would be suitable for zircon strain chronometry of D_3 deformation. The lack of lattice distortion in zircon grains has two explanations: (1) deformation conditions were not sufficient to produce permanent plastic deformation and/or (2) zircon grains formed after D_3 deformation.

Stress estimates in the Grenville Front reveal that deformation conditions were not sufficient to plastically deform zircon. As discussed in Chapter 5, the deformation conditions in the Wanapitei region are estimated to be under pressure between 810 ± 100 MPa, and temperature 684 ± 50ºC. At these P-T conditions and with the use of quartz grain size piezometry, the estimated differential stress in the area of the Wanapitei Complex is between 4 and 18.5 MPa. Figure 6-1 shows the range of temperature-stress conditions of D_3 in the Wanapitei Complex compared to previous studies of zircon yield and tensile strength; in this comparison, it is clear that the estimated stress in the current study is at least one order of

magnitude lower than necessary to result in permanent zircon strain. On that premise, an underestimate due to grain growth by annealing would not have a significant impact on the results, as the stress estimate would remain at least an order of magnitude lower than zircon yield. Without plastic deformation, the U-Pb system in zircon, which has a high closure temperature for trace element diffusion (> 900ºC (Lee et al., 1997)), would not have reset to record the age of deformation. The results of this thesis plot within the gap in knowledge of zircon material behaviour and thus call for further inquiry into the application of zircon strain chronometry to tectonic deformation. Further experiments to fill this gap are necessary. Work by Jones (*In Progress*) will explore the yield stress of zircon by hot indentation at temperatures below 500ºC.
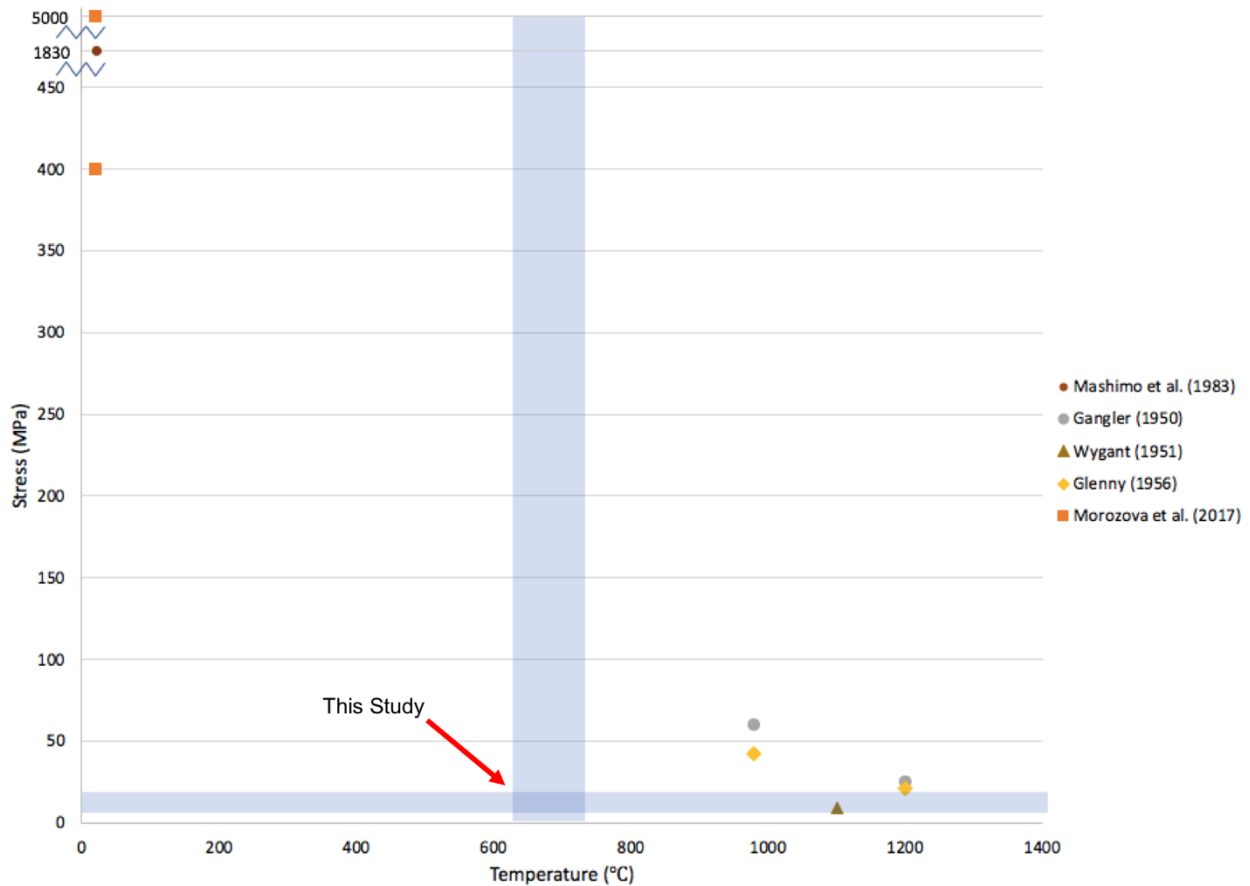
Figure 6-1. Yield strength of zircon, shaded regions show temperature-stress conditions of the Grenville Front from this study.

While these results agree with current knowledge of zircon strength, there have been a few cases where zircon strain has been observed in samples of similar composition and P-T conditions (e.g. Kaczmarek et al., 2011; Piazolo et al., 2012; Macdonald et al., 2013; Kovaleva et al., 2014; Kovaleva et al., 2016). This emphasizes the complexity of zircon lattice distortion as it is likely influenced by the interaction of many factors that have not been examined in their entirety. This study is one of the first to combine in situ zircon analysis with grain size piezometry to correlate microstructures with differential stress estimates in natural samples. Observations from this study integrate temperature, pressure and differential stress conditions with microstructural analysis of zircon and demonstrate that tectonic stresses of up to ~20 MPa do not deform micron-scale zircon. Previous studies (i.e. Kaczmarek et al., 2011; Piazolo et al., 2012; Macdonald et al., 2013; Kovaleva et al., 2014; Kovaleva et al., 2016) lack information on differential stress conditions that would be integral to comparing results to empirically determined zircon strength.

Explicit investigation of the additional factors on lattice distortion in shear zones (i.e. internal mechanical weakness, grain shape and grain orientation within the kinematic framework) compared with in situ microstructural analysis of deformed and undeformed zircon would allow for more definitive parameters on the development of permanent zircon deformation to be identified. The sample size in the present thesis was too small to identify definitive relationships with regards to these factors. The examination of these factors in future datasets will help establish how applicable zircon strain chronometry is to dating tectonic deformation and its practicality.

A secondary explanation for the lack of lattice distortion is that zircons may not have been present during D_3 deformation. The majority of zircons in these samples are either wholly

metamorphic or igneous with metamorphic rims. Metamorphic zircon can grow at a variety of times on the P-t path and importantly, through retrograde metamorphism (Kohn et al., 2015), isotopic ages of which would post-date deformation.

6.2 Conclusions and Future Recommendations

(1) This study marks the first integration of quartz grain size piezometry with microstructural analysis of zircon, and the first piezometric stress estimates in the Grenville Front Tectonic Zone.

(2) Microstructural analysis indicates that zircons within the Wanapitei Complex and surrounding country gneiss are primarily of metamorphic origin and do not display any significant lattice distortion as a result of regional deformation during the Grenville Orogeny.

(3) Optical microscopy of a cross-cutting granitic dyke (Wcc 4G) reveals the operation of subgrain rotation and grain boundary migration recrystallization mechanisms due to strain accommodation. The average recrystallized grain size in Wcc 4G is 136 μm. The metapelitic country gneiss (W2-2) lacks operation of dynamic recrystallization and has an average grain size of 180 μm.

(4) Using the recrystallized grain size of quartz and piezometers of Stipp and Tullis (2003), Austin and Evans (2007) and Shimizu (2012), differential stress is estimated to be in the range of 4-18.5 MPa in this region.

(5) The piezometers of Stipp and Tullis (2003) and Shimizu (2012) show concurrent results that agree with current quartz flow laws, while Austin and Evans (2007) underestimates the differential stress by an order of magnitude.

(6) The representative recrystallized grain size (i.e. median, RMS average, average) does not

have a large impact on differential stress estimates in these samples (< 5 MPa).

(7) If zircon grains were present at the time of D_3 deformation, based on previous studies of

yield strength of zircon, the differential stress estimates from this study are an order of

magnitude too low to result in meaningful permanent lattice distortion of zircon.

Alternatively, zircon grains may have resulted from new growth post-peak

metamorphism. In both cases, these results indicate that U-Pb isotopic ages would not

reflect the age of D_3 deformation any more precisely than previous efforts.

The results of this study raise questions as to the hope of effectively resolving the age of

deformation in geological conditions such as in the Grenville Front. Future studies in the GFTZ

require higher stress conditions (i.e. D_3 mylonites), larger sample sizes and larger zircon grain

size. I suggest three main objectives for subsequent studies.

Firstly, it is clear that there is a multitude of factors that need to be considered when

attempting to date deformation with zircon. Zircon remains one of the primary geochronological

tools; however, its potential has not yet been actualized. The application of zircon strain

chronometry to natural samples would benefit greatly from a better understanding of the factors

that influence lattice distortion. Defining the parameters surrounding these factors would allow

better sample selection and application of these methods. Studies of zircon strength within the

500-900ºC range and at low differential stress (< 250 MPa) are critical to better understand the

material behavior of zircon within natural shear zones. By determining these parameters, samples

could be better chosen with the intention of finding and dating plastic deformation.

Secondly, through careful in situ investigation and chemical analyses, metamorphic

zircon can be used to date deformation (Piazolo et al., 2012; Beckman et al., 2017). The

challenge of using metamorphic zircon becomes confirming that the crystallization age coincides with peak metamorphism. Following Kohn et al. (2015) zircon has been shown to dissolve during prograde reactions and grow preferentially during cooling and exhumation. Kohn et al. (2015) confirms the necessity of in situ investigation to identify growth domains and subsequent point dating of those distinct domains. Chemical analyses to establish the P-T conditions of the zircon growth domain can be used to correlate the age of zircon growth to the P-t path.

Lastly, the continued investigation into additional geochronological minerals such as baddeleyite and monazite has the potential to aid in the dating of deformational fabrics. As addressed in Chapter 5, there are no known metamorphic origins of baddeleyite. Therefore, investigating baddeleyite in metamorphic samples could provide an interesting insight into the igneous mineral and its response to deformation. Erickson et al. (2015) identified the first known cases of deformed natural monazite in the Sandmata granulite complex (India). Crystal-plastic deformation and recrystallization resulted in discordant ages that were believed to date Neoproterozoic deformation. Monazite should be investigated in future samples as it could provide an additional avenue to date deformation.

In conclusion, although these samples cannot be used to date D_3 deformation, these results give important insight into the enigmatic issue of dating tectonic deformation. It is clear that zircon is a useful but complex geochronological tool that requires intensive exploration. Given the uncertainties surrounding zircon and U-Pb dating of deformation, there is a breadth of research still to be done before zircon strain chronometry can be identified as a reliable source for dating deformation.

References

Ames, D.E., Davidson, A., Buckle, J.L., & Card, K.D. (2005). *Geology, Sudbury bedrock compilation, Ontario; Geological Survey of Canada, Open File 4570*, scale 1:50 000.

Austin, N. J., & Evans, B. (2007). Paleowattmeters: A scaling relation for dynamically recrystallized grain size. *Geology*, *35*(4), 343–346. https://doi.org/10.1130/G23244A.1

Austin, N., & Evans, B. (2009). The kinetics of microstructural evolution during deformation of calcite. *Journal of Geophysical Research*, *114*(B09402). https://doi.org/10.1029/2008JB006138

Beckman, V., Möller, C., Söderlund, U., & Andersson, J. (2017). Zircon Growth during Progressive Recrystallization of Gabbro to Garnet Amphibolite, Eastern Segment, Sveconorwegian Orogen. *Journal of Petrology*, *58*(1), 167–187. https://doi.org/10.1093/petrology/egx009

Bishop, R. R. (1996). *Grain boundary migration in experimentally deformed quartz aggregates: The relationship between dynamically recrystallized grainsize and steady state flow stress* (Master's Thesis). Brown University, Rhode Island, United States of America.

Brace, W. F., & Walsh, J. B. (1962). Some direct measurements of the surface energy of quartz and orthoclase. *American Mineralogist*, *47*(9–10), 1111–1122. Retrieved from https://pubs.geoscienceworld.org/msa/ammin/article-abstract/47/9-10/1111/541974/some-direct-measurements-of-the-surface-energy-of?redirectedFrom=fulltext

Brocoum, S.J., and Dalziel, I.W.D. 1974. The Sudbury Basin, the Southern Province, the Grenville Front, and the Penokean Orogeny. *Geological Society of America Bulletin*, *85*: 1571–1580. https://doi.org/10.1130/0016-7606(1974)85<1571:TSBTSP>2.0.CO;2.

Carr, S. D., Easton, R. M., Jamieson, R. a, & Culshaw, N. G. (2000). Geologic transect across the Grenville orogen of Ontario and New York. *Canadian Journal of Earth Sciences*, *37*(2–3), 193–216. https://doi.org/10.1139/e99-074

Chakoumakos, B. C., Murakami, T., Lumpkin, G. R., & Ewing, R. C. (1987). Alpha-decay-induced fracturing in zircon; the transition from the crystalline to the metamict state. *Science*, *236*(4808), 1556–1559. Retrieved from https://search.proquest.com/georefmodule/docview/51047844/8FA009AAB1A4DA1PQ/1?accountid=15115

Corfu, F., & Easton, R. M. (2000). U – Pb evidence for polymetamorphic history of Huronian rocks within the Grenville front tectonic zone east of Sudbury, Ontario, Canada. *Chemical Geology*, *172*(1–2), 149–171. https://doi.org/10.1016/S0009-2541(00)00241-2

Corfu, F., Hanchar, J. M., Hoskin, P. W. O., & Kinny, P. D. (2003). Atlas of Zircon Textures. *Reviews in Mineralogy and Geochemistry*, *53*(1), 469–500. https://doi.org/10.2113/0530469

Corrigan, D., Culshaw, N. G., & Mortensen, J. K. (1994). Pre-Grenvillian evolution and Grenvillian overprinting of the Parautochthonous Belt in Key Harbour, Ontario: U–Pb and field constraints. *Canadian Journal of Earth Sciences*, *31*(3), 583–596. https://doi.org/10.1139/e94-051

Cross, A. J., Ellis, S., & Prior, D. J. (2015). A phenomenological numerical approach for investigating grain size evolution in ductiley deforming rocks. *Journal of Structural Geology*, *76*, 22–34. https://doi.org/10.1016/j.jsg.2015.04.001

Culshaw, N. G., Ketchum, J. W. F., Wodicka, N., & Wallace, P. (1994). Deep crustal ductile extension following thrusting in the southwestern Grenville Province, Ontario. *Canadian Journal of Earth Sciences*, *31*(1), 160–175. https://doi.org/10.1139/e94-013

Davidson, A. (1984). Tectonic boundaries within the Grenville Province of the Canadian shield. *Journal of Geodynamics*, *1*(3–5), 433–444. https://doi.org/10.1016/0264-3707(84)90018-8

Davidson, A. (1995). Tectonic history of the Grenville Province, Ontario. *Open File Report – Geological Survey of Canada*, 150. https://doi.org/10.4095/205286

De Bresser, J., Ter Heege, J., & Spiers, C. (2001). Grain size reduction by dynamic recrystallization: can it result in major rheological weakening? *International Journal of Earth Sciences*, *90*(1), 28–45. https://doi.org/10.1007/s005310000149

Erickson, T. M., Pearce, M. A., Taylor, R. J. M., Timms, N. E., Clark, C., Reddy, S. M., & Buick, I. S. (2015). Deformed monazite yields high-temperature tectonic ages. *Geology*, *43*(5), 383–386. https://doi.org/10.1130/G36533.1

Farver, J. R., & Yund, R. A. (1991a). Measurement of oxygen grain boundary diffusion in natural, fine-grained, quartz aggregates. *Geochimica et Cosmochimica Acta*, *55*(6), 1597–1607. https://doi.org/10.1016/0016-7037(91)90131-N

Farver, J.R., & Yund, R.A. (1991b). Oxygen diffusion in quartz: dependence on temperature and water fugacity. *Chemical Geology, 90*(1-2), 55–70. https://doi.org/10.1016/0009-2541(91)90033-N

Francsis, M. K., Law, R. D., Spotila, J. A., & Caddick, M. J. (2012). *Piezometry and Strain Rate Estimates Along Mid-Crustal Shear Zones* (Master's Thesis). Virginia Polytechnic Institute and State University. Retrieved from http://hdl.handle.net/10919/32170

Gagnevin, D., Daly, J. S., & Kronz, A. (2010). Zircon texture and chemical composition as a guide to magmatic processes and mixing in a granitic environment and coeval volcanic system. *Contributions to Mineralogy and Petrology*, *159*(4), 579–596. https://doi.org/10.1007/s00410-009-0443-0

Gangler, J. J. (1950). Some Physical Properties of Eight Refractory Oxides and Carbides. *Journal of the American Ceramic Society*, *33*(12), 367–374. https://doi.org/10.1111/j.1151-2916.1950.tb14155.x

Giletti, B. J., & Yund, R. A. (1984). Oxygen Diffusion in Quartz. *Journal of Geophysical Research: Solid Earth*, *89*(B6), 4039–4046. https://doi.org/10.1029/JB089iB06p04039

Gleason, G. C., & Tullis, J. (1995). A flow law for dislocation creep of quartz aggregates determined with the molten salt cell. *Tectonophysics*, *247*(1–4), 1–23. https://doi.org/10.1016/0040-1951(95)00011-B

Glenny, E. (1956). A review of high strength materials for the rotor blading of high temperature aircraft gas turbines. *National Gas Turbine Establishment Farnborough (United Kingdom) -*

Memorandum, 84. Retrieved from https://apps.dtic.mil/dtic/tr/fulltext/u2/092862.pdf

Guillope, M., & Poirier, J. P. (1979). Dynamic recrystallization during creep of single-crystalline halite: An experimental study. *Journal of Geophysical Research*, *84*(B10), 5557. https://doi.org/10.1029/JB084iB10p05557

Hanchar, J. M., & Miller, C. F. (1993). Zircon zonation patterns as revealed by cathodoluminescence and backscattered electron images: Implications for interpretation of complex crustal histories. *Chemical Geology*, *110*(1–3), 1–13. https://doi.org/10.1016/0009-2541(93)90244-D

Harris, L. B., Koyi, H. A., & Fossen, H. (2002). Mechanisms for folding of high-grade rocks in extensional tectonic settings. *Earth-Science Reviews*, *59*(1–4), 163–210. https://doi.org/10.1016/S0012-8252(02)00074-0

Heaman, L., & LeCheminant, A. (1993). Paragenesis and U-Pb systematics of baddeleyite (ZrO2). *Chemical Geology*, 110(1-3), 95-126. https://doi.org/10.1016/0009-2541(93)90249-I

Heilbronner, R., and Tullis, J. 2002. The effect of static annealing on microstructures and crystallographic preferred orientations of quartzites experimentally deformed in axial compression and shear. Geological Society Special Publications, **200**: 191–218.

Hippertt, J., Rocha, A., Lana, C., Egydio-Silva, M., and Takeshita, T. 2001. Quartz plastic segregation and ribbon development in high-grade striped gneisses. Journal of Structural Geology, 23: 67–80. https://dx.doi.org/10.1016/S0191-8141(00)00129-2.

Hirth, G., Teyssier, C., & Dunlap, W. J. (2001). An evaluation of quartzite flow laws based on comparisons between experimentally and naturally deformed rocks. *International Journal of Earth Sciences*, *90*, 77–87. https://doi.org/10.1007/s005310000152

Hirth, G., & Tullis, J. (1992). Dislocation creep regimes in quartz aggregates. *Journal of Structural Geology*, *14*(2), 145–159. https://doi.org/10.1016/0191-8141(92)90053-Y

Holland, H. D., & Gottfried, D. (1955). The effect of nuclear radiation on the structure of zircon. *Acta Crystalographica*, *8*(6), 291–300. https://doi.org/10.1107/S0365110X55000947

Hoskin, P. W. O., & Schaltegger, U. (2003). The Composition of Zircon and Igneous and Metamorphic Petrogenesis Metamorphic Petrogenesis. *Reviews in Mineralogy and Geochemistry*, *53*(1), 27–62. https://doi.org/10.2113/0530027

Jones, G. (2019). *Indentation Hardness of Zircon* (Research in progress). University of Western Ontario, Canada.

Kaczmarek, M., Reddy, S. M., & Timms, N. E. (2011). Lithos Evolution of zircon deformation mechanisms in a shear zone (Lanzo massif, Western-Alps). *Lithos*, *127*(3), 414–426. https://doi.org/10.1016/j.lithos.2011.09.016

Ketchum, J. W. F., Heaman, L. M., Krogh, T. E., Culshaw, N. G., & Jamieson, R. A. (1998). Timing and thermal influence of late orogenic extension in the lower crust: a U-Pb geochronological study from the southwest Grenville orogen, Canada. *Precambrian Research*, *89*(1–2), 25–45. https://doi.org/10.1016/S0301-9268(97)00079-X

Kidder, S., Avouac, J.-P., & Chan, Y.-C. (2012). Constraints from rocks in the Taiwan orogen on crustal stress levels and rheology. *Journal of Geophysical Research: Solid Earth*, *117*(B9), 1–13. https://doi.org/10.1029/2012JB009303

Kidder, S., Hirth, G., Avouac, J., & Behr, W. (2016). The influence of stress history on the grain size and microstructure of experimentally deformed quartzite. *Journal of Structural Geology*, *83*, 194–206. https://doi.org/10.1016/j.jsg.2015.12.004

Kohn, M. J., Corrie, S. L., & Markley, C. (2015). The fall and rise of metamorphic zircon. *American Mineralogist*, *100*(4), 897–908. https://doi.org/10.2138/am-2015-5064

Kovaleva, E., & Klötzli, U. (2017). NanoSIMS study of seismically deformed zircon: Evidence of Y, Yb, Ce, and P redistribution and resetting of radiogenic Pb. *American Mineralogist*, *102*(6), 1311–1327. https://doi.org/10.2138/am-2017-5975

Kovaleva, E., Klötzli, U., Habler, G., Huet, B., Guan, Y., & Rhede, D. (2017). The effect of crystal-plastic deformation on isotope and trace element distribution in zircon: Combined BSE, CL, EBSD, FEG-EMPA and NanoSIMS study. *Chemical Geology, 450*, 183–198. https://doi.org/10.1016/j.chemgeo.2016.12.030

Kovaleva, E., Klötzli, U., Habler, G., & Libowitzky, E. (2014). Finite lattice distortion patterns in plastically deformed zircon grains. *Solid Earth*, *5*(2), 1099–1122. https://doi.org/10.5194/se-5-1099-2014

Kovaleva, E., Klötzli, U., & Habler, G. (2016). On the geometric relationship between deformation microstructures in zircon and the kinematic framework of the shear zone. *Lithos*, *262*, 192–212. https://doi.org/10.1016/j.lithos.2016.07.001

Kovaleva, E., Klötzli, U., Wheeler, J., & Habler, G. (2018). Mechanisms of strain accommodation in plastically-deformed zircon under simple shear deformation conditions during amphibolite-facies metamorphism. *Journal of Structural Geology*, *107*(December 2017), 12–24. https://doi.org/10.1016/j.jsg.2017.11.015

La Tour, T. E. (1981). Significance of folds and mylonites at the Grenville front in Ontario: Summary. *Geological Society of America Bulletin*, *92*(7), 411–413. https://doi.org/10.1130/0016-7606(1981)92<411:SOFAMA>2.0.CO;2

Lee, J. K., Williams, I. S., & Ellis, D. J. (1997). Pb, U and Th diffusion in natural zircon. *Nature*, *390*(6656), 159–162. https://doi.org/10.1038/36554

Li, C. (2012). *An Investigation of Deformation Structures and Their Tectonic Significance Across the Grenville Front Tectonic Zone in the Vicinity of Sudbury, Ontario, Canada* (PhD Thesis). University of Western Ontario, Canada. Retrieved from https://ir.lib.uwo.ca/cgi/viewcontent.cgi?referer=&httpsredir=1&article=1636&context=etd

Liati, A., Theye, T., Fanning, C. M., Gebauer, D., & Rayner, N. (2016). Multiple subduction cycles in the Alpine orogeny, as recorded in single zircon crystals (Rhodope zone, Greece). *Gondwana Research*, *29*(1), 199–207. https://doi.org/10.1016/j.gr.2014.11.007

Liu, F., Wang, F., Liu, P., & Liu, C. (2013). Multiple metamorphic events revealed by zircons from the Diancang Shan−Ailao Shan metamorphic complex, southeastern Tibetan Plateau. *Gondwana Research*, *24*(1), 429–450. https://doi.org/10.1016/j.gr.2012.10.016

Lloyd, G.E., and Freeman, B. 1994. Dynamic recrystallization of quartz under greenschist conditions. Journal of Structural Geology, *16,* 867–881. https://dx.doi.org/10.1016/0191-8141(94)90151-1.

Lu, L. X., & Jiang, D. (2019). Quartz flow law revisited: The significance of pressure dependence of the activation enthalpy. Journal of Geophysical Research: Solid Earth, 124. https://doi.org/10.1029/2018JB016226

Luan, F. C., & Paterson, M. S. (1992). Preparation and deformation of synthetic aggregates of quartz. *Journal of Geophysical Research*, *97*(B1), 301–320. https://doi.org/10.1029/91JB01748

Lumbers, S.B., 1971. Tomiko area, District of Nipissing; Summary of field work. ODM, Misc. Paper 30, p.84-88.

MacDonald, J. M., Wheeler, J., Harley, S. L., Mariani, E., Goodenough, K. M., Crowley, Q., & Tatham, D. (2013). Lattice distortion in a zircon population and its effects on trace element mobility and U-Th-Pb isotope systematics: examples from the Lewisian Gneiss Complex, northwest Scotland. *Contributions to Mineralogy and Petrology, 166*(1), 21–41. https://doi.org/10.1007/s00410-013-0863-8

Mackinnon, P., Fueten, F., & Robin, P-Y.F. 1997. A fracture model for quartz ribbons in straight gneisses. *Journal of Structural Geology*, *19*(1), 1–14. https://doi.org/10.1016/S0191-8141(96)00073-9.

Mashimo, T., Nagayama, K., & Sawaoka, A. (1983). Shock Compression of Zirconia ZrO_2 and Zircon $ZrSiO_4$ in the Pressure Range up to 150 GPa. *Physics and Chemistry of Minerals*, *9*(6), 237–247. https://doi.org/10.1007/BF00309573

McLelland, J. M., Selleck, B. W., & Bickford, M. E. (2010). Review of the Proterozoic evolution of the Grenville Province, its Adirondack outlier, and the Mesoproterozoic inliers of the Appalachians. In R. P. Tollo, M. J. Bartholomew, J. P. Hibbard, & P. M. Karabinos (Eds.), *From Rodinia to Pangea: The Lithotectonic Record of the Appalachian Region* (Vol. 206, p. 21-49). Geological Society of America. https://doi.org/10.1130/2010.1206(02)

Möller, C., Andersson, J., Lundqvist, I., & Hellström, F. (2007). Linking deformation, migmatite formation and zircon U-Pb geochronology in polymetamorphic orthogneisses, Sveconorwegian Province, Sweden. *Journal of Metamorphic Geology*, *25*, 727–750. https://doi.org/10.1111/j.1525-1314.2007.00726.x

Möller, A., O'Brien, P. J., Kennedy, A., & Kröner, A. (2003). Linking growth episodes of zircon and metamorphic textures to zircon chemistry: an example from the ultrahigh-temperature granulites of Rogaland (SW Norway). *Geological Society London Special Publications*, *220*(1), 65–81. https://doi.org/10.1144/GSL.SP.2003.220.01.04

Morozova, I., Shieh, S. R., Moser, D. E., Barker, I. R., & Hanchar, J. M. (2017). Strength and Deformation of Zircon at Crustal and Mantle Pressures. In D. E. Moser, F. Corfu, J. R. Darling, S. M. Reddy, & K. Tait (Eds.), *Microstructural Geochronology* (pp. 169–182). https://doi.org/10.1002/9781119227250.ch7

Moser, D. E., Cupelli, C. L., Barker, I. R., Flowers, R. M., Bowman, J. R., Wooden, J., & Hart, J. R. (2011). New zircon shock phenomena and their use for dating and reconstruction of large impact structures revealed by electron nanobeam (EBSD, CL, EDS) and isotopic U-Pb and (U-Th)/He analysis of the Vredefort dome. *Canadian Journal of Earth Sciences*, *48*(2), 117–139. https://doi.org/10.1139/E11-011

Moser, D. E., Davis, W. J., Reddy, S. M., Flemming, R. L., & Hart, R. J. (2009). Zircon U–Pb strain chronometry reveals deep impact-triggered flow. *Earth and Planetary Science Letters*, *277*(1–2), 73–79. https://doi.org/10.1016/j.epsl.2008.09.036

Murphy, E. I. (2001). Geology, metamorphism and geochemistry of rocks of the Southern and

Grenville Provinces in the vicinity of the Grenville Front, Timmins Creek Area, near Sudbury, Ontario. *Open File Report - Ontario Geological Survey*, 132.

Nikon. *NIS-Elements Advanced Research: User's Guide (Ver. 4.00).* Retrieved from http://www.torontomicrofluidics.ca/cms/manuals/niselements.pdf

Otani, M., and Wallis, S. 2006. Quartz lattice preferred orientation patterns and static recrystallization: Natural examples from the Ryoke belt, Japan. Geology, *34*, 561–564. https://doi:10.1130/G22430.1.

Passchier, C. W., & Trouw, R. A. J. (1996). *Microtectonics*. Springer Berlin Heidelberg.

Piazolo, S., Austrheim, H., & Whitehouse, M. (2012). Brittle-ductile microfabrics in naturally deformed zircon: Deformation mechanisms and consequences for U-Pb dating. *American Mineralogist*, *97*(10), 1544–1563. https://doi.org/10.2138/am.2012.3966

Piazolo, S., Fontaine, A. La, Trimby, P., Harley, S., Yang, L., Armstrong, R., & Cairney, J. M. (2016). Deformation-induced trace element redistribution in zircon revealed using atom probe tomography. *Nature Communications*, *7*, 1–7. https://doi.org/10.1038/ncomms10490

Post, A., & Tullis, J. (1999). A recrystallized grain size piezometer for experimentally deformed feldspar aggregates. *Tectonophysics*, *303*(1–4), 159–173. https://doi.org/10.1016/S0040-1951(98)00260-1

Prevec, S. A. (1995). Sm–Nd isotopic evidence for crustal contamination in the ca. 1750Ma Wanapitei Complex, western Grenville Province, Ontario. *Canadian Journal of Earth Sciences*, *32*(4), 486–495. https://doi.org/10.1139/e95-041

Reddy, S. M., Timms, N. E., Pantleon, W., & Trimby, P. (2007). Quantitative characterization of plastic deformation of zircon and geological implications. *Contributions to Mineralogy and Petrology*, *153*(6), 625–645. https://doi.org/10.1007/s00410-006-0174-4

Reddy, S. M., Timms, N. E., Trimby, P., Kinny, P. D., Buchan, C., & Blake, K. (2006). Crystal-plastic deformation of zircon: A defect in the assumption of chemical robustness. *Geology*, *34*(4), 257–260. https://doi.org/10.1130/G22110.1

Rivers, T. (1997). Lithotectonic elements of the Grenville Province: review and tectonic implications. *Precambrian Research*, *86*(3–4), 117–154. https://doi.org/10.1016/S0301-9268(97)00038-7

Rivers, T. (2008). Assembly and preservation of lower, mid, and upper orogenic crust in the Grenville Province—Implications for the evolution of large hot long-duration orogens. *Precambrian Research*, *167*(3–4), 237–259.https://doi.org/10.1016/j.precamres.2008.08.005

Rivers, T., Martignole, J., Gower, C. F., & Davidson, A. (1989). New tectonic divisions of the Grenville Province, Southeast Canadian Shield. *Tectonics*, *8*(1), 63–84. https://doi.org/10.1029/TC008i001p00063

Ross, J.V., Ave Lallemant, H.G., & Carter, N. L. (1980). Stress dependence of recrystallized-grain and subgrain size in olivine. *Tectonophysics*, *70*(1–2), 39–61. https://doi.org/10.1016/0040-1951(80)90020-7

Rousell, D. H., & Trevisiol, D. D. (1988). Geology of the mineralized zone of the Wanapitei Complex, Grenville Front, Ontario. *Mineral Deposita*, *23*(2), 138–149. https://doi.org/10.1007/BF00206663

Rutter, E. H., & Brodie, K. H. (2004). Experimental intracrystalline plastic flow in hot-pressed synthetic quartzite prepared from Brazilian quartz crystals. *Journal of Structural Geology*, *26*(2), 259–270. https://doi.org/10.1016/S0191-8141(03)00096-8

Schmid, S. M., Paterson, M. S., & Boland, J. N. (1980). High temperature flow and dynamic recrystallization in carrara marble. *Tectonophysics*, *65*(3–4), 245–280. https://doi.org/10.1016/0040-1951(80)90077-3

Schwerdtner, W. M., Rivers, T., Tsolas, J., Waddington, D. H., Page, S., & Yang, J. (2016). Transtensional origin of multi-order cross-folds in a high-grade gneiss complex, southwestern Grenville Province: formation during post-peak gravitational collapse. *Canadian Journal of Earth Sciences*, *53*(12), 1511–1538. https://doi.org/10.1139/cjes-2015-0212

Shimizu, I. (1998). Stress and temperature dependence of recrystallized grain size: A subgrain misorientation model. *Geophysical Research Letters*, *25*(22), 4237–4240. https://doi.org/10.1029/1998GL900136

Shimizu, I. (2008). Theories and applicability of grain size piezometers: The role of dynamic recrystallization mechanisms. *Journal of Structural Geology*, *30*(7), 899–917. https://doi.org/10.1016/j.jsg.2008.03.004

Shimizu, I. (2012). Steady-State Grain Size in Dynamic Recrystallization of Minerals. In K. Sztwiertnia (Ed.), *Recrystallization*. Rijeka: IntechOpen. https://doi.org/10.5772/33701

Sterner, M., & Pitzer, K. S. (1994). An equation of state for carbon dioxide valid from zero to extreme pressures. *Contributions to Mineralogy and Petrology*, *117*(4), 362–374. https://doi.org/10.1007/BF00307271

Stipp, M., & Tullis, J. (2003). The recrystallized grain size piezometer for quartz, *30*(21), 2088. https://doi.org/10.1029/2003GL018444

Stipp, M., Tullis, J., & Behrens, H. (2006). Effect of water on the dislocation creep microstructure and flow stress of quartz and implications for the recrystallized grain size piezometer. *J. Geophys. Res*, *111*, 4201. https://doi.org/10.1029/2005JB003852

Stipp, M., Tullis, J., Scherwath, M., & Behrmann, J. H. (2010). A new perspective on paleopiezometry: Dynamically recrystallized grain size distributions indicate mechanism changes. *Geology*, *38*(8), 759–762. https://doi.org/10.1130/G31162.1

Tă maş, C. G. (2002). *Structuri de "Breccia pipeî associate unor ză că minte hidrotermale din România* (PhD Thesis). Babeş-Bolyai University, Cluj-Napoca, Romania.

Tă maş, C. G., & Milési, J. P. (2002). Hydrovolcanic breccia pipe structures; general features and genetic criteria; I, Phreatomagmatic breccias. *Studie Universitatis Babes-Bolyai. Geologia*, *47*(1), 127–147. Retrieved from https://search.proquest.com/georefmodule/doc view/50440763/9459475134C74C6BPQ/1?accountid=15115

Tollo, R. P., Corriveau, L., McLelland, J., & Bartholomew, M. J. (2004). Proterozoic tectonic evolution of the Grenville Orogen in North America: An introduction. *Geological Society of America*, *197*(6), 1–18. https://doi.org/10.1130/0-8137-1197-5.1

Twiss, R. J. (1977). Theory and Applicability of a Recrystallized Grain Size Paleopiezometer. *Pure and Applied Geophysics*, *115*(1–2), 227–244. https://doi.org/10.1007/BF01637105

Urai, J.L., Means, W.D., and Lister, G.S. 1986. Dynamic recrystallization of minerals. Geophysical Monograph, *36,* 161–199. doi:http://dx.doi.org.proxy1.lib.u wo.ca/10.1029/GM036p0161.

Vernon, R.H. 1981. Optical microstructure of partly recrystallized calcite in some naturally deformed marbles. Tectonophysics, *78*, 601–612.

White, S. 1977. Geological significance of recovery and recrystallization processes in quartz. Tectonophysics, *3,* 143–170.

Wightman, R. H., Prior, D. J., & Little, T. A. (2006). Quartz veins deformed by diffusion creep-accommodated grain boundary sliding during a transient, high strain-rate event in the Southern Alps, New Zealand. *Journal of Structural Geology*, *28*(5), 902–918. https://doi.org/10.1016/j.jsg.2006.02.008

Williams, P. F., & Jiang, D. (2005). An investigation of lower crustal deformation : Evidence for channel flow and its implications for tectonics and structural studies, 27, 1486–1504. https://doi.org/10.1016/j.jsg.2005.04.002

Winter, J. 2010. Principles of Igneous and Metamorphic Petrology. In 2nd edition. Pearson.

Wygant, J. F. (1951). Elastic and Flow Properties of Dense, Pure Oxide Refractories. *Journal of the American Ceramic Society*, *34*(12), 374–380. https://doi.org/10.1111/j.1151-2916.1951.tb13017.x

Wynne-Edwards, H.R. 1972. The Grenville Province. *Special Paper - Geological Association of Canada, 11*: 263–334. Retrieved from https://www.lib.uwo.ca/cgibin/ezpauthn.cgi?url=http://search.proquest.com/docview/52511072?accountid=15115

Curriculum Vitae

Name:	Kaitlyn Petkau
Post-secondary Education and Degrees:	Queen's University Kingston, Ontario, Canada 2012-2016, B.Sc. University of Western Ontario London, Ontario, Canada 2016-2019, M.Sc.
Graduate Coursework:	Geology 1577 Exploration Drilling Practices Geology 9580 Graduate Seminar Geology 9555 Rock Flow in Crust & Mantle Geology 9702 Special Topics in Geology
Honours and Awards:	Dean's Honour List 2014, 2015, 2016, Queen's University Manley B. Baker Scholarship in Geology 2014, Queen's University William E. White Scholarship in Geology 2015, Queen's University The J. Allan Donaldson Prize in Geology 2015, Queen's University The Susan Near Prize in Geology 2016, Queen's University
Related Work Experience:	Teaching Assistant University of Western Ontario 2016-2018